Rydberg molecules and circular Rydberg states in cold atom clouds

by

David Alexander Anderson

A dissertation submitted in partial fulfillment
of the requirements for the degree of
Doctor of Philosophy
(Applied Physics)
in The University of Michigan
2015

Doctoral Committee:

Professor Georg A. Raithel, Chair
Professor Luming Duan
Professor Alex Kuzmich
Thomas Pohl, Max Plank Institute for Physics
Associate Professor Vanessa Sih

For my family

ACKNOWLEDGEMENTS

First I have to thank my advisor Georg Raithel for his continued support, patience, and encouragement during the completion of this dissertation and throughout my time working in the Raithel group. Without his insights, direction, and deep understanding of the subject matter, none of it would have been possible. His enthusiasm for research and insatiable curiosity have been an inspiration in the years I have been fortunate to have spent under his wing. Thank you Georg for giving me the opportunity to learn from you.

Over the years I have had the pleasure of working with many former and current members of the Raithel group from whom I have learned a great deal. Many thanks to Sarah Anderson, Yun-Jhih Chen, Luís Felipe Gonçalves, Cornelius Hempel, Jamie MacLennan, Stephanie Miller, Kaitlin Moore, Eric Paradis, Erik Power, Andira Ramos, Rachel Sapiro, Andrew Schwarzkopf, Nithiwadee Thaicharoen (Pound), Mallory Traxler, and Kelly Younge, for making my time in the Raithel group such an enjoyable experience.

Thank you to my committee members, Georg Raithel, Thomas Pohl, Vanessa Sih, Alex Kuzmich, and Luming Duan, for your support and willingness to serve on my committee.

Thank you Charles Sutton, Lauren Segall, Cynthia McNabb, and Cagliyan Kurdak in the Applied Physics Program and the staff in the Department of Physics here at the University of Michigan for all the wonderful work you do.

This dissertation would not have been possible without the help and support of many other people. Thanks go to my fellow graduate students, Alex Toulouse, Liz Shtrahman, Chris Trowbridge, Channing Huntington, Prashant Padmanaban, Jeffrey Herbstman, Andrea Bianchini, Danny Maruyama, Mike McDonald, for your friendships and the adventures

we have shared over the years. To my Brickhouse family: Alex, Liz (the summer sublet counts), Rob Wyman, Laurel Couture, Gina DiBraccio, Lucas Bartosiewicz, Haydee Izaguirre, Cassandra Izaguirre, Megan Williams, Claire Roussel and Guilliaume Maisetti, Jenny Geiger, Sophie Kruz, Sarah Bliss, Carson Schultz, Megan Blair, and the many more friends and visitors that helped fill the house with great conversation and good company. Thank you for making Ann Arbor a place called home. Thank you Johnny Adamski and Nick Nacca for the fishing and camping trips, to Peter and Kathy Adamski for your love and support. And to my family, thank you for always pointing me in the right direction.

TABLE OF CONTENTS

LIST OF FIGURES

Figure

LIST OF TABLES

Table

LIST OF APPENDICES

Appendix

ABSTRACT

Rydberg molecules and circular Rydberg states in cold atom clouds

by

David A. Anderson

Chair: Georg Raithel

In this dissertation I investigate cold Rydberg atoms and molecules in which the angular-momentum character of the quantum states involved strongly influences their properties and dynamics. In the first part I focus on long-range diatomic Rydberg molecules formed by a rubidium D-state Rydberg atom and a second rubidium atom in its ground state. Spectroscopic measurements of molecular binding energies are presented showing the effect of the Rydberg atom size and fine-structure coupling on the molecular potentials. A theoretical model is introduced that takes into account all relevant angular-momentum couplings between the molecular constituents, successfully reproducing experimental observations. Calculations of adiabatic potentials and binding energies, molecular-state lifetimes, electric and magnetic dipole moments are also presented. In the second part, I describe the production and magnetic trapping of cold circular Rydberg atoms. The circular Rydberg atoms are generated out of a cold gas of rubidium using the crossed-fields method and magnetically trapped. The trapping force is employed to induce center-of-mass oscillations of the trapped atom sample. Trap parameters and observed oscillation frequencies are used to measure the magnetic moments of the circular Rydberg atoms. Trap losses and the atomic internal-state evolution in the 300 Kelvin thermal background are also investigated.

CHAPTER I

Introduction

1.1 A historical perspective

The development of quantum mechanics during the first decades of the twentieth century changed our fundamental understanding of nature and provided the language to describe the structure of atoms and molecules and their dynamics in remarkable detail. Among the many experimental discoveries and theoretical breakthroughs during this period, two are of notable influence. The first is the experiments described by Ernest Rutherford in his 1911 paper on the scattering of alpha and beta particles from various metals, which led him to propose that atoms consist of a massive central positive charge whose field is compensated by the negative charge of surrounding electrons [6]. The second was Niels Bohr's 1913 paper on the hydrogen atom, which, drawing direct inspiration from Rutherford's work, introduced the two entirely new ideas that an electron in an atom could only occupy discrete levels with quantized energies and that the transitions between two levels were linked to the emission of monochromatic radiation [7]. In this, Bohr proposed a model in which the electron could only occupy quantized circular orbits around the positively charged proton. Initially, Bohr's theory found success in its ability to account for the Balmer spectral series in hydrogen, but its applicability waned as it could not account for phenomena observed in experiments conducted soon thereafter, including the discovery of the spin of particles by Otto Stern and Walther Gerlach [8]. Nevertheless, the ideas Bohr presented provided the conceptual

framework essential for the subsequent development of the full modern theory of quantum wave mechanics.

An important aspect of Bohr's model is that it linked the Rydberg constant, a constant determined empirically to describe the wave numbers (energies) of transitions in atoms, to fundamental constants including the mass and charge of the electron. This connection gave, for the first time, a picture of atomic structure and physical meaning to experimentally observed spectroscopic signatures of atoms. In addition, Bohr's model of hydrogen provided insight into physical properties of atoms beyond their level structures, one being that the binding energy of the electron in a state of principal quantum number n scales as $1/n^2$, establishing that electrons in states of high n are only loosely bound to the atomic nucleus and are more easily ionized than those in low n states; another being that the radial distance of the electron in orbit about the nucleus scales as n^2, which for states with high n results in very large orbits and atom sizes. With this, Bohr's model provided the first description of what today we call a Rydberg atom, an atom with an electron in a state of high n, and a first glimpse of the many interesting properties they exhibit.

One of the earliest experiments to directly investigate the properties of Rydberg atoms beyond their level structures was performed by Edoardo Amaldi and Emilio Segrè in 1934 [9] in which they studied the effects different foreign gases (H_2, N_2, He, and Ar) had on the high-n absorption lines of Na and K atoms. Their experiment realized conditions in which the alkali Rydberg atoms were large enough to encompass as many as several thousand atoms or molecules of the foreign gas within the orbit of the Rydberg electron. They observed that the absorption lines were shifted substantially in proportion to the pressure of the foreign gas and were only slightly broadened. Importantly, they found that the foreign gas shifted the spectral lines to both lower and higher energies depending on the nature of the gas, and that the shifts were independent of the alkali species. An explanation of these observations was provided by Enrico Fermi [10] who reasoned that two different mechanisms contributed to the observed phenomena; the first being a polarization-induced shift in which the electric

field of the unshielded, positively-charged atomic core polarizes the foreign gas in its vicinity within the orbit of the Rydberg electron. The energy required to polarize the gas is matched by a reduction in the energy of the Rydberg atom, resulting in a red shift of the spectral line. To explain the shifts to higher energies, which were unexpected and could not be accounted for by the first mechanism, Fermi suggested a second mechanism in which the low-energy Rydberg electron interacts via repeated scattering events with atoms of the foreign gas. In a quantum treatment, he described the foreign gas atoms as point-like perturbers to the much larger Rydberg electron wave function and quantified the interaction energy between the perturber and the electron using a single parameter, the S-wave scattering length A_s. The scattering length, a concept introduced by Fermi for the first time in this 1934 paper, provides a very general and powerful means to describe low-energy interactions by precluding the need for an exact form of the interaction potential, which in this case would require knowledge of the detailed structure of the perturbing atom or molecule. For given values of A_s, together with the smaller contribution of the polarization-induced shift, the Fermi model successfully described the experimental observations.

1.1.1 Long-range Rydberg molecules

The topic of collisions between Rydberg atoms and neutral perturbers was studied periodically in the subsequent decades [11]. In 1977 the theoretical groundwork laid by Fermi was revisited by Alain Omont [12] who described how the scattering interaction between a Rydberg electron and ground-state atom essentially amounts to the formation of a molecular state - a diatomic molecule formed between a Rydberg atom and ground-state atom bound by an attractive scattering interaction. Despite the novelty of this prediction, very little attention was paid to it due to the inability of experiments at the time to reach the high spectral resolution and low thermal energies necessary to probe these molecular states. It was not until the development of narrow line width tunable lasers [13], that higher resolution spectroscopy of atomic structure become possible and more detailed studies of atomic and

molecular properties began in earnest. In addition, the subsequent development of laser cooling and atom trapping techniques, epitomized by the Bose-Einstein condensation (BEC) of atomic vapors in 1995 [14, 15], opened new prospects for experiments at low energy.

Following these developments, Chris Greene, Alan Dickinson, and Hossein Sadeghpour pointed out in 2000 that the high densities and low temperatures of atomic BECs provided suitable conditions for the observation of these molecules [4]. Greene and his colleagues also showed that the distinctive binding mechanism of these molecules, which is unlike conventional covalent, ionic, and van der Waals bonds between ground-state atoms, would result in large molecules whose properties are strongly influenced by the angular momentum state ℓ of the Rydberg electron. They classified Rydberg molecules into two categories: (1) low-ℓ Rydberg molecules formed by a Rydberg atom in a non-degenerate angular momentum state with binding energies corresponding to tens of $h\times$MHz and (2) high-ℓ Rydberg molecules formed by a Rydberg atom in a degenerate mix of high-angular-momentum states, whose binding energies are typically on the order of $h\times$GHz - a class of molecules they called "trilobite" molecules with kilo-Debye electric dipole moments. Valuable insights were also provided by A. A. Khuskivadze, M. I. Chibisov and I. I. Fabrikant, who calculated detailed molecular adiabatic potentials, wave functions and electric dipole moments for both Rb_2 and Cs_2 Rydberg molecules [1], highlighting how the potentials for alkali systems are strongly affected by both low-energy ^{3}S-wave and ^3P_j-wave electron-atom scattering resonances [16, 17, 18]. In Rb_2, the ^{3}S interaction leads to the trilobite Rydberg molecules [4] and the ^{3}P interaction produces potentials [19] that are about an order of magnitude deeper and about a factor of five shorter-range than the trilobite potentials. These theoretical efforts contributed to a more detailed model of the Rydberg and ground-state atom interaction and the properties of long-range Rydberg molecules.

Long-range Rydberg molecules were observed for the first time in 2009 in the group of Tilman Pfau [20]. In their experiment, Rydberg molecules consisting of a rubidium nS (ℓ=0) Rydberg atom and rubidium ground-state atom were photoassociated [21] out of an ultra-

cold rubidium gas. The spectra revealed several weakly-bound (tens of MHz) vibrational states over a range of n =34 to 40. The spectra were modeled using a Fermi/Omont-type interaction potential to extract a value for the e^-+Rb zero-energy scattering length of $A_s = 18.5\ a_0$, agreeing qualitatively with predicted values [16, 17, 18]. Since then, Rydberg molecules have continued to be the subject of significant experimental interest. Developments include studies of diatomic Rydberg molecules in cesium [22, 23], rubidium P-states at low n [24] and D-states [25, 26], the realization of coherent bonding and dissociation of S-type molecules [27], and the first observation of a permanent electric dipole moment in a homonuclear molecule [28]. Polyatomic Rydberg molecules have also been generated [29] and employed in a demonstration of the continuous transition between a few-body to many-body regime in an ultracold quantum gas [30].

The nature of this new molecular bond and the properties of Rydberg molecules are largely dependent on both the Rydberg-atom wave function and angular-momentum couplings in the molecular constituents. Since their discovery, however, the effects of angular momentum on the properties of long-range Rydberg molecules have remained largely unexplored. In this dissertation (Chapters IV and V) I study the effects of angular momentum on the properties of rubidium Rydberg molecules. In experiments, the $^{87}\mathrm{Rb}(nD + 5S_{1/2})$ molecules are photoassociated out of a cold rubidium gas. The vibrational ground-state energies are measured for $34 \leq n \leq 40$ and found to be larger than those of their $^{87}\mathrm{Rb}(nS+5S_{1/2})$ counterparts, showing the dependence of the molecular binding on ℓ. The molecular binding energies are described using a simple Fermi-type model that includes S-wave triplet scattering and the fine structure of the nD Rydberg atom, from which a value for the triplet S-wave scattering length is obtained. The transition of $^{87}\mathrm{Rb}(nD + 5S_{1/2})$ molecules from a molecular-binding-dominant regime at low n to a fine-structure-dominant regime at high n [akin to molecular angular-momentum Hund's coupling cases (a) and (c), respectively] is also revealed. An expanded Fermi model for Rydberg molecules is introduced with all the relevant angular-momentum couplings including S-wave and P-wave singlet and triplet scat-

tering of the Rydberg electron with the $5S_{1/2}$ atom, along with the fine structure coupling of the Rydberg atom as well as the hyperfine structure coupling of the $5S_{1/2}$ atom. For high-ℓ Rydberg molecules, the molecular binding interaction is stronger than the fine-structure coupling, and is comparable to the hyperfine coupling of the ground-state perturber. Inclusion of the $5S_{1/2}$ hyperfine coupling in the model generates additional adiabatic potentials of mixed triplet and singlet character in both high- and low-ℓ molecules. Very recently, low-ℓ molecular bound states in these spin-mixed potentials have been observed in Cs_2 [23].

Alongside their appeal as fundamentally new molecular systems, long-range Rydberg molecules are also unique in part because they amount to very low-energy ($\lesssim$ 1meV) electron-atom scattering experiments at the single-atom level. Because of the strong dependence of the molecular potentials and bound-state energies on the electron-atom scattering phase shifts, absolute measurements of these phase shifts at meV electron energies become possible via high-resolution spectroscopy on these molecular states. Understanding the relevant angular-momentum couplings and their effects on the properties of long-range Rydberg molecules is a prerequisite to such measurements.

1.1.2 Circular Rydberg atoms

Bohr described the hydrogen atom as having a single valence electron in a circular orbit around the atomic core. Today these atoms are known as circular atoms, whose quantum wave function is a torus peaked along the circle of the classical Bohr orbit of the electron. Circular Rydberg atoms combine a large principal quantum number n with maximal orbital and magnetic quantum numbers $\ell = |m| = n - 1$, and exhibit a unique set of properties. These include extremely long radiative lifetimes ($\sim$ milliseconds to seconds, compared to typical atomic state lifetimes of $\sim$ nanoseconds to microseconds), giant magnetic moments (readily an order of magnitude larger than those of their low-ℓ counterparts), and posses no linear Stark shifts and small quadratic Stark shifts.

While the quantum description of circular atoms was established early on with the de-

velopment of quantum mechanics, the preparation and observation of these atomic states in the laboratory came much later. Due to the technical difficulty of imparting many units of angular momentum into an atom, circular Rydberg atoms are not readily produced by conventional optical excitation since a single photon carries only one unit of angular momentum. It was not until 1983 that Randall Hulet and Daniel Kleppner demonstrated for the first time the efficient transfer of lithium atoms from low m states to $|m| = n - 1$ circular states using an adiabatic rapid passage technique [31]. In this technique, the lowest-lying m state of a Stark manifold is first optically excited in the presence of an electric field. This is followed by the application of a fixed-frequency microwave field which couples $\Delta|m| = +1$ transitions as the electric field is ramped down linearly, tuning the states into resonance. Due to the different quadratic Stark shift of the m levels, the transitions occur consecutively in time until the maximally allowed value of $|m|$ (i.e. the circular state) is reached. Since then modifications to this method and other methods for the production of circular Rydberg atoms have been developed and demonstrated [32, 33, 34, 35]. Another production technique of particular relevance to this dissertation is the crossed-fields method, which was proposed by Delande and Gay in 1988 [5, 36] and demonstrated soon thereafter by Hare et al. [37]. In this method, an atom is optically excited to an extreme hydrogenic Stark state and transferred to the circular state using only external electric and magnetic fields, precluding the need for a large number of microwave photons.

With the tools to generate circular Rydberg atoms in the laboratory, many experiments were able to exploit the properties of these high-angular-momentum states, and in particular their long lifetimes and reduced energy-level perturbations. Transitions between circular states provide a near-perfect two-level system due to their single radiative decay channel ($|m| \rightarrow |m|-1$), making them suitable for atom-cavity interaction experiments [38]. Circular atoms have found great success as model systems for quantum measurements and landmark tests of quantum mechanics [39, 40, 41], a body of work that was recognized by the 2012 Nobel prize in physics shared by Serge Haroche and David Wineland [42, 43]. A notable

recent experiment used circular Rydberg atoms for the first non-demolition measurement of single photons [44]. There, microwave photons stored in a cavity were probed repeatedly by circular atoms, whose large dipole matrix elements make them sensitive to light-shifts at the single-photon level. The reduced nuclear and QED perturbations, and low sensitivity to external fields of circular states have also made these atoms good candidates for precision Rydberg spectroscopy and high precision measurements of the Rydberg constant [45, 46, 47].

Experiments with circular atoms have to date been performed at high temperature, primarily using atomic beams. A number of proposed experiments require circular atoms at low temperature. These include a recent proposal for a high-precision measurement of the Rydberg constant [48] using an amplitude-modulated optical lattice [49] to drive transitions between circular and near-circular Rydberg levels. In this effort, circular Rydberg atoms at $T \lesssim 1\mu$K are required in order to utilize shallow lattices, which are necessary for reduced lattice-induced shifts of the Rydberg levels. Recently, the use of cold circular Rydberg atoms to realize a two-qubit quantum gate has also been proposed [50]. Due to the toroidal shape of their wave functions, circular Rydberg atoms are also expected to have highly anisotropic collision cross sections [51, 52]. A means to generate circular atoms at low temperature would enable experimental studies of low-energy collisional processes involving high-ℓ and circular state atoms.

In Chapter VI of this dissertation I describe and demonstrate a technique for the production and trapping of circular Rydberg atoms at low temperature [53]. This is accomplished by generating circular Rydberg atoms locally in a cold, magnetically-trapped sample of ^{87}Rb atoms in their ground state using the crossed-fields method. The high spatial resolution afforded by the optical excitation in this method, along with the presence of the local magnetic trapping field, make this method particularly well-suited for localized circular Rydberg atom generation in magnetically-trapped ground-state atom samples.

1.2 Dissertation framework

This dissertation is organized as follows. In Chapter II I present some theoretical background to the work discussed in subsequent chapters. The content is drawn from several standard texts on quantum mechanics and atomic physics [54, 55, 56, 57, 58]. In Chapter III I describe the experimental apparatus and methods used for preparing and probing cold, dense rubidium ground-state and Rydberg atoms. Rubidium is used in all the experiments in this work. In Chapter IV I describe an experimental study of long-range rubidium nD Rydberg molecules and the influence of the Rydberg-atom angular momentum and fine structure on the molecular binding. In Chapter V I present a detailed theoretical study on the influence of angular-momentum couplings in $^{87}Rb_2$ long-range Rydberg molecules formed between a D-state Rydberg atom and $5S_{1/2}$ ground-state atom. A Fermi model is introduced that includes S-wave and P-wave singlet and triplet scattering of the Rydberg electron with the $5S_{1/2}$ atom, along with the fine structure coupling of the Rydberg atom and hyperfine structure coupling of the $5S_{1/2}$ atom. In Chapter VI I describe the production and magnetic trapping of cold circular Rydberg atoms. Trap losses and the internal state-evolution and dynamics of the trapped circular state atoms in the T=300 K black body radiation field are characterized.

CHAPTER II

Theoretical background

In this chapter I review some general theoretical background relevant to the work in the following chapters. I begin in section 2.1 with the non-relativistic time-independent Schrödinger equation for atomic hydrogen, which serves as a model for Rydberg atoms with more complex internal structure followed by the hydrogen fine structure in section 2.2. In section 2.3 I cover general properties of Rydberg atoms and some distinguishing features of low-ℓ and high-ℓ states, including radiative lifetimes and effects of blackbody radiation. The Stark effect for Rydberg atoms and the Rydberg excitation blockade are also described. Finally, in section 2.4 I introduce the theoretical framework used to describe long-range diatomic Rydberg molecules formed by a Rydberg atom and ground-state pertuber. Elastic scattering theory and its application to low-energy electron-Rb scattering is described. The adiabatic molecular potentials for long-range Rydberg molecules resulting from the scattering-induced interaction are introduced and the vibrational and rotational energies of the molecular states discussed. In the final section of this chapter I describe Hund's cases for the classification of angular-momentum couplings in diatomic molecules.

2.1 Hydrogen

Due to the similarity of hydrogen to other single-electron atoms, the hydrogenic wave functions and state energies provide a useful framework for understanding the properties

of Rydberg atoms. Hydrogen serves as a particularly good model for high-ℓ and circular Rydberg states of heavier atomic species as a result of the weak interaction between the Rydberg electron with the atomic core for these states.

One of the most well-established applications of quantum mechanics is its use in describing atoms with a single electron orbiting in the Coulomb field of a nucleus. The non-relativistic time-independent Schrödinger equation for an electron of mass m_e and charge $-e$ in the field of a nucleus with mass M and charge Ze is

$$[-\frac{\hbar^2}{2\mu}\nabla^2 + V(r)]\psi = E\psi, \tag{2.1}$$

where the potential $V(r) = -\frac{Ze^2}{4\pi\epsilon_0 r}$ is the Coulomb potential energy of the electron in the field of the positively charged nucleus and $\mu = \frac{m_e M}{(m_e+M)}$ is the reduced mass of the system. For hydrogen $Z = 1$ and M is the proton mass.

Considering only the relative motion of the two particles and assuming there are no external forces, Eq. 2.1 can be separated in spherical coordinates where the center of mass (which is near the nucleus) is chosen to be at the origin with an arbitrary direction for the polar axis z, and (r, θ, ϕ) is the spatial coordinate of the electron. Writing the Laplacian operator ∇^2 in spherical coordinates, and expressing the eigenfunction solutions as a product of radial and angular functions

$$\psi(r, \theta, \phi) = R_{n,\ell}(r)Y_{\ell,m}(\theta, \phi) \tag{2.2}$$

Eq. 2.1 separates into two differential equations, one for the radial part of the wave function and one for the angular part of the wave function. The differential equation satisfied by the angular functions $Y_{\ell,m}(\theta, \phi)$ is

$$\hbar^2\hat{L}^2 Y_{\ell,m}(\theta, \phi) = \hbar^2\ell(\ell+1)Y_{\ell,m}(\theta, \phi), \tag{2.3}$$

$$\hat{L}^2 = -\frac{1}{\sin\theta}\frac{\partial}{\partial\theta}(\sin\theta\frac{\partial}{\partial\theta}) - \frac{1}{\sin^2\theta}\frac{\partial^2}{\partial\phi^2}, \tag{2.4}$$

where $\hat{L}^2$ is the operator for the orbital angular momentum squared and ℓ is the orbital angular momentum quantum number, which can take on any integer value from 0 to $n-1$. For a given ℓ this results in $2\ell+1$ unique solutions to Eq. 2.3 given by the spherical harmonics

$$Y_{\ell,m}(\theta,\phi) = \sqrt{\frac{(2\ell+1)}{4\pi}\frac{(\ell-m)!}{(\ell+m)!}} P_\ell^m(\cos\theta)e^{im\phi}, \tag{2.5}$$

where P_ℓ^m are the associated Legendre functions and m is the magnetic quantum number, which can take on any integer value from $-\ell$ to ℓ.

The differential equation satisfied by the radial functions $R_{n,\ell}(r)$ is given by

$$[\frac{-\hbar^2}{2\mu}\frac{1}{r^2}\frac{d}{dr}(r^2\frac{d}{dr}) + V_{eff}(r)]R_{n,\ell} = E_n R_{n,\ell}, \tag{2.6}$$

where the effective potential

$$V_{eff}(r) = \frac{\hbar^2\ell(\ell+1)}{2\mu r^2} - \frac{Ze^2}{4\pi\epsilon_0 r} \tag{2.7}$$

includes both the radial Coulomb interaction energy and the repulsive centrifugal term. The binding energy of the electron is

$$E_n = -\frac{\mu e^4}{(4\pi\epsilon_0)^2 2\hbar^2}\frac{Z^2}{n^2}, \tag{2.8}$$

which depends only on the principal quantum number n as a result of a degeneracy of states with different ℓ in the Coulomb potential. The radial wave function $R_{n,\ell}(r)$ is given by

$$R_{n,\ell}(r) = -\frac{(n-\ell-1)!^{\frac{1}{2}}}{(n+1)!^{\frac{3}{2}}(2n)^{\frac{1}{2}}}\kappa^{\frac{3}{2}}e^{-\kappa r}(\kappa r)^\ell L_{n+1}^{2\ell+1}(\kappa r) \tag{2.9}$$

where $L_{n+1}^{2\ell+1}(\kappa r)$ are the Laguerre functions and $\kappa = 2Z/n$. Combining Eqns. 2.5 and 2.9 one then obtains a complete expression for the hydrogen wave functions.

2.2 Fine structure

In addition to orbital angular momentum $\hat{L}$, which in a classical picture is a measure of the particle's rotation about a given axis and depends explicitly on its spatial degrees of freedom, a particle can also have a spin $\hat{S}$, which is an intrinsic property with no classical counterpart. Generally, in atoms and molecules the coupling between angular momenta of the constituent particles can strongly influence their level structures and properties. The quantum treatment of angular momentum and addition of angular momenta is reviewed in Appendix A.

LS-coupling and relativistic effects lead to additional fine structure splittings of atomic energy levels. In hydrogen, the fine structure splittings are not accounted for in the non-relativistic Schrödinger equation in Eq. 2.1 but are fully accounted for in the relativistic quantum mechanics of Dirac, which gives an exact expression for the electron binding energy in the absence of external fields [54]

$$\frac{E_{Dirac}}{m_e c^2} = [1 + (\frac{\alpha Z}{n - k + \sqrt{k^2 - \alpha^2 Z^2}})^2]^{-1/2} - 1. \tag{2.10}$$

Here, $k = j + 1/2$ where j is the quantum number for the total angular momentum $\hat{\mathbf{J}}$=$\hat{\mathbf{L}}$+$\hat{\mathbf{S}}$ of the electron, where $\hat{\mathbf{L}}$ is its orbital angular momentum and $\hat{\mathbf{S}}$ its spin. The constants $\alpha = e^2/4\pi\epsilon_0\hbar c = 7.297 \times 10^{-3} \approx 1/137$ and c=2.998×10^8 m/s [59] are the fine-structure constant and speed of light, respectively. Expanding Eq. 2.10 in powers of $(\alpha Z)^2$ and taking the first two terms gives

$$E_{n,j} = -\frac{\text{Ry Z}^2}{n^2}[1 + \frac{(\alpha Z)^2}{n}(\frac{1}{j + 1/2} - \frac{3}{4n})], \tag{2.11}$$

where the Rydberg energy Ry=$m_e c^2 \alpha^2/2$ is ≈13.6 eV [59]. The zeroth order term in Eq. 2.11 reproduces the non-relativistic binding energy of the electron given by Eq. 2.8. The first-order term adds a fine-structure correction on the order of $\alpha^2 \sim 10^{-4} - 10^{-5}$ times the

non-relativistic binding energy, and depends on both n and j. The splitting between the $j = \ell + 1/2$ and $j = \ell - 1/2$ fine-structure states is given by

$$\Delta E^{(1)}_{n,j} = \frac{\text{Ry } Z^4\alpha^2}{n^3}(\frac{1}{\ell(\ell+1)}). \tag{2.12}$$

It follows that the fine-structure coupling for low angular-momentum ($n > \ell$) and high angular-momentum ($n \approx \ell$) states scales as $\approx 1/n^3$ and $\approx 1/n^5$, respectively, and the fine-structure energy for low-ℓ states is larger than for high-ℓ states. In hydrogen-like alkali Rydberg atoms, whose outer electron is affected by the presence of a larger inner core, the relativistic corrections and core penetration to the energies are accounted for using quantum defects (see section 2.3). However, the general n (n^* in quantum defect theory) and ℓ scaling behaviors of the fine-structure in (2.12) hold.

2.3 Rydberg atoms

Alkali Rydberg atoms are similar to hydrogen in that they have a single unpaired electron orbiting a positive central charge. The difference lies in that the positive central charge of alkali atoms is a larger and more complex ion, consisting of electrons in closed inner shells surrounding a heavy nucleus. For high-ℓ states, whose wave functions have a small overlap with the ionic core, the Rydberg electron experiences nearly the same Coulomb potential as in hydrogen and their energies are similar. For low-ℓ states, whose wave functions have a larger overlap with the core, there is less screening of the nuclear charge resulting in significantly lower energies compared to those in hydrogen. The binding energy of a Rydberg electron is

$$E_n = -\frac{\text{Ry}_{\text{alkali}}}{(n-\delta_{\ell j})^2} = -\frac{\text{Ry}_{\text{alkali}}}{n^{*2}}, \tag{2.13}$$

where n is the principal quantum number and $\delta_{\ell j}$ are the quantum defects, which account for core perturbations and fine-structure in alkalis, n^* is the effective principal quantum

number, and $\mathrm{Ry}_{\mathrm{alkali}}$ is the Rydberg energy for a Rydberg alkali atom with effective mass μ. The quantum defects $\delta_{\ell j}$ also have a small energy dependence given by

$$\delta_{n\ell j} = \delta_0 + \frac{\delta_2}{(n-\delta_0)^2} + \frac{\delta_4}{(n-\delta_0)^4} + \frac{\delta_6}{(n-\delta_0)^6} + ... \tag{2.14}$$

where the parameters $\delta_0, \delta_2, \delta_4, \delta_6, ...$ are determined empirically. For rubidium and other alkalis, the quantum defects have been measured to high precision [56, 60, 61]. For high-ℓ states a small quantum defect correction due to core polarization is often used given by $\delta_\ell = 3\alpha_D/4\ell^5$ [56], where the measured dipolar polarizability for Rb^+ is $\alpha_D = 9.023$ atomic units [62]. Low-ℓ and high-ℓ states are typically distinguished by the size of their quantum defect. In rubidium, the S, P, and D states ($\ell = 0, 1$ and 2, respectively) are typically categorized as low-ℓ because they have quantum defects on the order of 1, while the F, G and higher-ℓ states ($\ell \geq 3$) have much smaller defects and comprise the high-ℓ group.[1]

Rydberg atoms exhibit properties that scale strongly with n^*. Table 2.1 summarizes some of the properties of Rydberg atoms and their n^*-dependence. From Table 2.1, it is apparent that all Rydberg atoms share similar characteristics and that low-ℓ Rydberg states exhibit different physics than high-ℓ Rydberg states. In the following sections I describe in more detail several Rydberg atom properties relevant to this work, highlighting important differences between low-ℓ and high-ℓ Rydberg states.

[1] The small quantum defects for the F and G states in rubidium have also been measured [63, 64].

Table 2.1: Selected properties of Rydberg atoms and their dependence on n^*.

Property	n^*-scaling	
Binding energy	n^{*-2}	
Orbital radius	n^{*2}	
Classical velocity	n^{*-1}	
Keppler frequency	n^{*-3}	
Geometric cross section	n^{*4}	
Dipole moment $\langle n^{*\prime}\ell' = \ell \pm 1 \vert er \vert n^*\ell\rangle$	n^{*2}	
Polarizability	n^{*7}	
Energy splitting between adjacent n^*	n^{*-3}	
	$n^* > \ell$	$n^* \approx \ell$
Fine-structure splitting	n^{*-3}	n^{*-5}
Radiative lifetimes	n^{*3}	n^{*5}

2.3.1 Radiative lifetimes

Perhaps the most striking difference between low- and high-ℓ Rydberg states are the significantly longer lifetimes of high-ℓ states compared to those of low-ℓ states. The lifetimes can be understood by considering spontaneous decay rates. The spontaneous decay rate from a Rydberg state $|i\rangle = |n^*\ell\rangle$ to a lower-energy state $|f\rangle = |n^{*\prime}\ell'\rangle$ is given by the Einstein A coefficient

$$A_{i\to f} = \frac{\nu_{i\to f}^3}{3\pi\epsilon_0\hbar c^3}|d_{i\to f}|^2, \tag{2.15}$$

where $\nu_{i\to f}$ is the transition frequency and $d_{i\to f} = \langle f|er|i\rangle$ is the transition dipole moment. The total spontaneous decay rate out of state $|i\rangle$ is obtained by summing over all final states

$|f\rangle$ and the initial state's radiative lifetime is given by

$$\tau_i^{rad} = (\sum_f A_{i\to f})^{-1}. \tag{2.16}$$

Due to the strong dependence of the decay rate (2.15) on ν, transitions with the highest frequency generally contribute the largest terms in the sum (2.16), and the dominant decay channel for a high-lying atomic state is a dipole-allowed transition to the state with the lowest energy. For Rydberg states with $n^* >> \ell$, the change in principal quantum number Δn^* is therefore large compared to the $\Delta\ell = \pm 1$, imposed by dipole selection rules. In the limit of high n^* the transition frequency ν approaches a constant due to the n^{*-2}-scaling of the binding energy, and for low-ℓ Rydberg states the decay rate is then mostly determined by the dipole moment between the high-n Rydberg state and a low-n atomic state. This amounts to the $n^{*-3/2}$-dependence of the Rydberg wave function at small distances from the ionic core [54, 56]. The wave function density near the nucleus is then $\sim n^{*-3}$, and for the lifetimes of low-ℓ Rydberg states one then finds

$$\tau_{\mathrm{low}-\ell}^{\mathrm{rad}} \propto n^{*3}. \tag{2.17}$$

The decay behavior is different for high-ℓ Rydberg states with $n^* \approx n \approx \ell$. Consider a circular state (CS) which has maximal angular momentum $\ell = n - 1$. By dipole selection rules, the spontaneous decay out of the CS is limited to a single decay channel with $\Delta\ell = \Delta n = -1$. In this case, the transition frequency $\nu \propto n^{-3}$ is much smaller. The transition dipole moment, on the other hand, is larger and scales like the size of the atom $d = \langle n' = n-1, \ell' = n-2|er|n\ell = n-1\rangle \sim n^2$ due to the large overlap of the wave functions. From this one then finds for the lifetimes of Rydberg atoms in high-ℓ states

$$\tau_{\mathrm{high}-\ell}^{\mathrm{rad}} \propto n^5. \tag{2.18}$$

Rydberg atoms with $n = 10 - 100$ are common in experiments, spanning a broad range of radiative lifetimes for both low- and high-ℓ states. Radiative lifetimes for selected low- and high-ℓ Rydberg states are given in the $T = 0\ K$ column of table 2.2.

Table 2.2: Lifetimes of selected Rydberg states at T=0 and 300 Kelvin.

Rydberg state	T=0 K (τ^{rad})	T=300 K (τ)
Rb(60P)	$\sim 500\ \mu$s	$\sim 200\ \mu$s
Rb(60CS)	$\sim$70 ms	$\sim 400\ \mu$s

In practice, the measured lifetimes of Rydberg states are smaller than their radiative lifetimes due to additional decay processes such as collisions with other particles and interactions with external fields [65]. For the circular state experiment discussed in chapter VI, in which cold circular Rydberg atoms are produced and magnetically trapped, the long interaction times of the circular states with their environment allow additional decay mechanisms to significantly influence their decay behavior. There, collisions between circular Rydberg atoms and ground-state atoms as well as thermally-induced transitions out of the CS due to 300 K black body radiation play dominant roles.

2.3.2 Black body radiation

Rydberg atoms are strongly affected by room-temperature black body radiation. This is due to the fact that $kT = 2.6 \times 10^{-2}$ eV at $T = 300$ Kelvin is much larger than the transition energies $h\nu \approx 10^{-5}$ eV between Rydberg states, and the transition dipole moments for Rydberg-Rydberg transitions are large, typically $d \gtrsim 10^3\ ea_0$. In a thermal radiation field, the stimulated emission rate from a Rydberg state to another state is equal to its spontaneous decay rate times the photon occupation number of a corresponding mode ν in a black body

radiation field at temperature T [56]

$$\begin{aligned} B_{i\to f} &= \bar{n}A_{i\to f} \\ &= \frac{A_{i\to f}}{e^{h\nu_{i\to f}/kT}-1}. \end{aligned} \tag{2.19}$$

The stimulated absorption rate of a thermal photon is similarly given by Eq.2.19 with the transition rate $A_{i\to f}$ evaluated for the transition to the final higher-energy state. The black body limited lifetime is then obtained as in (2.16)

$$\tau_i^{\rm bb} = (\sum_f B_{i\to f})^{-1}, \tag{2.20}$$

where now the sum is over all states at both lower and higher energy, including continuum states. From this, the total Rydberg atom lifetime then becomes

$$\tau = (\frac{1}{\tau^{\rm rad}} + \frac{1}{\tau^{\rm bb}})^{-1}. \tag{2.21}$$

For Rydberg atoms, $h\nu << kT$ and $\bar{n} \approx kT/h\nu$ so the number of thermal photons available to drive transitions generally increases $\propto n^{*3}$. For high-ℓ Rydberg states, whose radiative decay rates scale as n^{-5} (2.18), one might expect from (2.19) that $B_i \lesssim n^{-2}$. In fact, it can be shown that

$$B_i \propto \frac{kT}{n^{*2}}, \tag{2.22}$$

which is typically valid for $n^* \gtrsim 15$ and does not depend on ℓ [56]. From this, the effects of black body radiation on the lifetimes of high and low-ℓ states become apparent. Since the radiative lifetimes $\tau^{\rm rad}$ of high-ℓ states are typically much longer than $\tau^{\rm bb}$, the total decay of a high-ℓ state is dominated by black body transitions which often result in a significant redistribution of population between nearby Rydberg levels. For the low-ℓ states, whose radiative lifetimes are shorter, thermally-driven decays play a smaller role and the lifetimes

are less affected. A comparison is given in table 2.2, which shows calculated lifetimes for rubidium 60P and 60CS Rydberg state for both T=0 (radiative only) and 300 K (radiative and black body).

These lifetimes reflect the typical time the atom spends in a well-defined Rydberg state. For atoms in circular and high-ℓ Rydberg states, a 300 Kelvin radiation background preferentially drives transitions to nearby Rydberg states with comparatively long radiative lifetimes. There, the time the atom spends in a highly-excited Rydberg state prior to decaying to the ground state or being ionized by the thermal radiation background is typically longer than the lifetime given by Eq. 2.21. This is in contrast to low-ℓ states, which are less affected by thermal radiation and preferentially decay to low-lying states. As a result, in atom counting and trapping experiments, while an atom may have decayed in a strict sense, there is often still a measurable signal over much longer times and the definition of a "lifetime" becomes ambiguous.

In addition to driving resonant transitions between states, the black body radiation field also contributes to AC Stark shifts of the atomic energy levels. For Rydberg states, this amounts to a ponderomotive energy shift of the loosely bound Rydberg electron in the oscillating black body radiation field. At T=300 K, the black body induced shift is ≈ 2 kHz, which is much smaller than the smallest ($\sim$MHz) energy scales relevant in this work.

2.3.3 Stark effect

The shifting and splitting of spectral lines of atoms and molecules in a static electric field is known as the Stark effect. Due to their large electric dipole moments, Rydberg atoms are generally very sensitive to electric fields and exhibit large Stark shifts compared to atoms in low-n and ground states. The Stark interaction between an atom with a dipole moment $\hat{d}$ and an electric field $\vec{E}$ is [56]

$$V_{Stark} = -\hat{d} \cdot \vec{E}. \tag{2.23}$$

Using the spherical basis and choosing the direction of the electric field to be along r, the matrix elements are

$$\langle V_{Stark} \rangle = eE\langle n'\ell'm'|\hat{r}|n\ell m\rangle. \tag{2.24}$$

The dipole operator in Eq. 2.23 only couples states with opposite parity ($m = m'$ for $\vec{E} \,||\, \hat{z}$ and $\ell' = \ell \pm 1$). Since the matrix elements in Eq. 2.24 are all proportional to E, it follows that the Stark states are linear combinations of zero-field high-ℓ states. These states exhibit linear Stark shifts and therefore posses permanent dipole moments. The Stark shifts and dipole moments are also dependent on m. For the circular state, which has $|m| = \ell = n - 1$, there exists no other state with the same n and m. The circular state therefore exhibits no first-order Stark shift (and only a small second-order Stark shift $\sim n^6$). The lower m states, on the other hand, include degenerate ℓ states that do couple with increasingly larger radial matrix elements at lower ℓ. The lowest m states in the manifold therefore exhibit the largest Stark shifts, which are equal to approximately $\pm\frac{3}{2}n^2Eea_0$ for the most extreme states. This also follows from describing the Stark effect in parabolic coordinates. In parabolic coordinates, Schrödinger's equation remains separable in the presence of an electric field, and the states are defined by parabolic quantum numbers n_1 and n_2, in addition to n and $|m|$ [54, 56]. The parabolic quantum numbers are connected by $n = 1 + |m| + n_1 + n_2$, and the first-order Stark energies given by $\frac{3}{2}Eea_0n(n_1 - n_2)$.

For non-degenerate low-ℓ Rydberg states, the matrix elements in Eq. 2.24 vanish and one needs to go to second order in the field for a contribution to the energy. The low-ℓ states therefore do not have permanent dipole moments and exhibit quadratic Stark shifts

$$\langle V_{Stark} \rangle^{(2)} = -\frac{1}{2}\alpha_{pol}\vec{E}^2, \tag{2.25}$$

where the static polarizability

$$\alpha_{pol} = 2\sum_{n' \neq n} \frac{|\langle n\ell m|e\hat{r}|n'\ell'm'\rangle|^2}{W_{n\ell m} - W_{n'\ell'm'}}. \tag{2.26}$$

Here, W_i is the energy of the atomic state i. The polarizabilities of low-ℓ Rydberg states scale approximately as n^7, making them very sensitive to electric fields. In this work, Stark spectroscopy on rubidium D-state Rydberg atoms ($\alpha_{pol} \approx [2 \times 10^{-13}\ GHz/(V/cm)^2] \times n^7$) is performed to measure electric fields in the experiments and calibrate voltage-controlled electrodes used to control electric fields in the experimental region (see section 3.3).

2.3.4 Rydberg excitation blockade

Due to their large dipole moments and polarizabilities Rydberg atoms also exhibit strong electrostatic interactions with other Rydberg atoms. For low-ℓ Rydberg states, which do not have permanent dipole moments, the interaction results from the large transition dipole moments to nearby states. Resonant transitions give rise to first-order dipole-dipole interactions $\Delta W^{(1)} \propto n^4/r^3$ and off-resonant transitions give rise to second-order van der Waals interactions between the atoms $\Delta W^{(2)} \propto n^{11}/r^6$. For low-$\ell$ states the van der Waals usually dominates at long distances in the absence of external fields [66].

A consequence of the strong interactions between Rydberg atoms is the Rydberg excitation blockade [67, 68, 69]. The blockade can be interpreted qualitatively as a process in which the electrostatic field of one Rydberg atom Stark shifts atoms in its vicinity out of resonance with the optical excitation field thereby inhibiting, or "blocking" their excitation to Rydberg states. Since the interaction strength between Rydberg atoms depends on their separation, the effectiveness of the blockade is limited in range. In the van der Waals case, this range is given by the blockade radius

$$r_b = (\frac{C_6 n^{*11}}{h \times \delta\nu_L})^{1/6}, \tag{2.27}$$

where $\delta\nu_L$ is the line width of the excitation laser and the C_6 coefficient sets the strength of the Rydberg-Rydberg interaction, which for low-ℓ states in rubidium have been previously calculated [70] and recently measured [71]. Since the initial Rydberg excitation is not deter-

ministic, the excitation blockade is in reality not a two-step process but a many-body effect, which in recent years has been a subject of significant interest for applications in quantum information processing [72, 73, 74]. In this work, the Rydberg blockade is not a topic of interest in itself but because it can influence the number of Rydberg atoms generated by optical excitation in an atomic sample it nevertheless plays an important role in the interpretation of the Rydberg excitation spectra.

2.4 Long-range Rydberg molecules

The Rydberg molecules of interest in this work consist of an atom in a highly excited Rydberg state and a second atom in its ground state. These molecular states are unique in that the binding arises from an attractive low-energy scattering interaction between the Rydberg atom's valence electron and the ground-state atom. The theoretical framework for these molecules is generally well-established. The interaction between a low-energy Rydberg electron and ground-state atom can be described using a Fermi pseudo-potential approach [4, 10, 12]. In the Fermi model, the ground-state atom is treated as a delta-function perturber of the Rydberg-electron wave function, resulting in oscillatory potential curves with localized minima capable of sustaining bound molecular states. In this section I give some background on low-energy electron-atom scattering and how this scattering interaction gives rise to bound molecular states for a Rydberg electron scattering off of a ground-state atom.

2.4.1 Elastic scattering and partial waves

The formal quantum approach to elastic scattering between two particles is to treat it as the scattering of a single particle with reduced mass μ by a potential $V_s(\mathbf{r})$. In this center of mass coordinate system, the free particle incident with momentum $\hbar k$ along the z axis is treated as a plane wave $\psi_{in} = e^{ikz}$ and the scattered particles, far from a spherically-symmetric scattering center $V_s(\mathbf{r})$, are treated as an outgoing spherical wave $\psi_{out} = f(\theta)\frac{e^{ikr}}{r}$.

At large distances ($r \to \infty$) the full wave function then takes the asymptotic form [55]

$$\psi \approx e^{ikz} + f(\theta)\frac{e^{ikr}}{r}, \tag{2.28}$$

where $f(\theta)$ is the scattering amplitude and is a function of the scattering angle θ between the z-axis and direction of the scattered particle. With the assumption that the two components of the asymptotic wave function (2.28) do not interfere, namely that the measurement is made of ψ_{out} only, the differential cross section for a particle scattered between θ and $\theta + d\theta$ is given by

$$\frac{d\sigma}{d\theta} = 2\pi \sin(\theta)|f(\theta)|^2. \tag{2.29}$$

The exact wave function is a solution to Schrödinger's equation whose radial wave function satisfies

$$\frac{\hbar^2}{2\mu}\frac{1}{r^2}\frac{d}{dr}(r^2\frac{dR_{k,l}}{dr}) + [E_k - V_{eff}(r)]R_{k,l} = 0, \tag{2.30}$$

where the effective scattering potential is given by

$$V_{eff}(r) = \frac{\hbar^2 l(l+1)}{2\mu r^2} + V_s(r), \tag{2.31}$$

where $E_k = \frac{\hbar^2 k^2}{2\mu}$ is the kinetic energy of the two-particle system.[2] It follows from the form of 2.28 that all solutions to Eq. 2.30 are axially symmetric about z, and therefore independent of ϕ, and that each corresponds to the motion of the particles with energy E_k, orbital angular momentum l, and zero projection onto the z-axis, $m_l = 0$.The wave function then takes the form

$$\psi = \sum_{l=0} C_l P_l(\cos(\theta))R_{k,l}, \tag{2.32}$$

[2]Note the use of l here to distinguish the angular momentum associated with the scattering from the atomic orbital quantum number ℓ.

where C_l are coefficients and $P_l(\cos(\theta))$ are the Legendre functions. In order for ψ to have the asymptotic form of Eq. 2.28

$$C_l = \frac{1}{2k}(2l+1)i^l e^{i\delta_l(k)} \tag{2.33}$$

and

$$R_{k,l} \approx \frac{2}{r}\sin(kr - \frac{l\pi}{2} + \delta_l(k)), \tag{2.34}$$

where $\delta_l(k)$ are the energy- and l-dependent phase shifts of $R_{k,l}$ relative to the incident wave. Combining 2.33 and 2.34 for the asymptotic form of the full wave function 2.32, one obtains the scattering amplitude and corresponding total cross section [75]

$$f(\theta) = \sum_{l=0}(2l+1)f_l(k)P_l(\cos(\theta)) \tag{2.35}$$

$$\sigma = \frac{4\pi}{k^2}\sum_{l=0}(2l+1)\sin^2(\delta_l(k)), \tag{2.36}$$

and the l-th partial-wave amplitude $f_l(k)$ and corresponding partial cross section

$$f_l(k) = \frac{e^{2i\delta_l}-1}{2ik} = \frac{1}{k\cot(\delta_l(k)) - ik} \tag{2.37}$$

$$\sigma_l = 4\pi(2l+1)|f_l|^2. \tag{2.38}$$

In the limit where $k \to 0$ only the l=0 component contributes, and the elastic cross section is given by

$$\lim_{k\to 0}\sigma = 4\pi A_{s0}^2, \tag{2.39}$$

where A_{s0} is the zero-energy S-wave scattering length.

2.4.2 Low-energy electron-Rb scattering

The diatomic Rydberg molecules studied in this work result from a low-energy scattering interaction between a Rydberg electron and a rubidium ground-state atom. Since the Ryd-

berg electron's kinetic energy depends on its location within the Coulomb field of the atomic core and the ground-state atom can in principle reside anywhere within the spatial extend of the Rydberg-atom wave function, the energy-dependence of the scattering interaction is important for describing long-range Rydberg molecules. The energy-dependent partial-wave scattering length for low-energy electron-atom scattering can be expressed as [12, 19]

$$A_l(k) = -\frac{\tan(\delta_l(k))}{k^{2l+1}}. \tag{2.40}$$

At increasing interaction energies, $l > 0$ partial waves contribute to the interaction. The contributing partial waves can be determined by comparing the energy of the scattering particles E_k to the effective potential energy V_{eff}. If E_k is small compared to V_{eff} such that there is a negligible tunneling probability through the centrifugal barrier, the corresponding ℓ-th partial wave does not significantly contribute to the scattering interaction and can be neglected. At low temperature, the thermal motion of the ground-state atom and Rydberg atom is negligible compared to the kinetic energy of the Rydberg electron, which sets the interaction energy E_k.[3] The kinetic energy of the Rydberg electron as a function of distance R from the ionic core can be obtained from the semiclassical expression

$$\frac{\hbar^2 k^2}{2\mu} = -\frac{Ry}{2n^{*2}} + \frac{e^2}{4\pi\epsilon_0 R}. \tag{2.41}$$

For a $34D$ Rydberg electron at a distance of 2000 a_0 from the atomic core, corresponding to the outermost lobe of the 34D Rydberg wave function, $E_k \approx 1$ meV. For electron-Rb scattering, the scattering potential $V_s(\mathbf{r})$ can be described by the short-range polarization of

[3]It is also instructive to consider the different timescales for the motion of the particles involved in the scattering interaction. Consider atoms at a temperature $T = 20$ μK, with a corresponding thermal energy $\approx h \times 200$ kHz and average velocity ≈ 5 cm/s. An $n = 34$ Rydberg electron scattering off of an atom in this sample has a Keppler frequency of 167 GHz. The average distance traveled by the atom over the course of one Keppler orbit of the Rydberg electron is $\approx 2 \times 10^{-13} m$, and hundreds of scattering events can take place before the atom moves one Bohr radius.

the ground-state atom by the Coulomb field of the Rydberg electron

$$V_{pol} = -\frac{e^2}{(4\pi\epsilon_0)^2}\frac{\alpha_{Rb}}{2r^4}, \tag{2.42}$$

where the polarizability of the rubidium ground-state atom $\alpha_{Rb} = 319 \pm 6$ in atomic units ($= h \times 0.0794 \pm 0.0015$ Hz/(V/cm)^2 in SI units) [76]. Here, $\mathbf{r}$ is the relative coordinate in the center of mass frame of the ground-state atom and electron system. Figure 2.1 shows $V_{eff}(r)$ for $l = 0, 1, 2$, where we see that for $l = 0$ the interaction is purely attractive, and for $l = 1$ the centrifugal barrier peaks at $\approx$ 40 meV around 16a$_0$. At 1 meV electron energies, the tunneling probability through the $l = 1$ barrier is small. The molecular states investigated in Chapter IV are associated with these low-energy electron-Rb interactions and are dominated by S-wave scattering.[4] P-wave scattering is not entirely suppressed, however, and can have a substantial effect on the molecular adiabatic potentials at smaller internuclear separations where the Rydberg electron kinetic energy is higher. The effects of P-wave scattering on the molecular potentials is investigated in more detail in Chapter V. As a result of the l^2 scaling of the centrifugal term, D-wave and higher-order ($l > 2$) partial waves are nearly entirely suppressed for the molecular states of interest and are therefore neglected.

Low-energy electron-atom scattering interactions can also exhibit resonances. These occur at specific energies where the electron and atom remain bound together for a time exceeding the expected transit time of the electron through the extent of the atom, forming a negative ion. Two types of resonances are typically distinguished: those at energies below the asymptotic energy of the non-interacting free electron and atom system, where the interaction potential is deep enough to support bound states, and those with energies above this energy, where the centrifugal barrier confines the scattering particle near the target [77].

[4]The tunneling probability through the $l = 1$ barrier can be estimated by considering an incident $E_k =$ 1 meV electron incident on a rectangular barrier with a height $V_0 \approx 40$ meV and width $a \approx 20$ a_0. The tunneling probability T is given by

$$T = (1 + \frac{V_0^2 \sinh^2(\varrho a)}{4E_k(V_0 - E_k)})^{-1}, \tag{2.43}$$

where $\varrho = \sqrt{2\mu(V_0 - E_k)/\hbar^2}$ and μ is the reduced mass. For the above parameters T=0.07.

The latter are known as shape resonances, which require a repulsive potential barrier and therefore generally only occur for P-wave and higher l scattering. Low-energy electron-Rb($5S$) scattering exhibits a well-known ^{3}P-wave shape resonance near 20 meV [1, 16, 19], which is discussed further below.

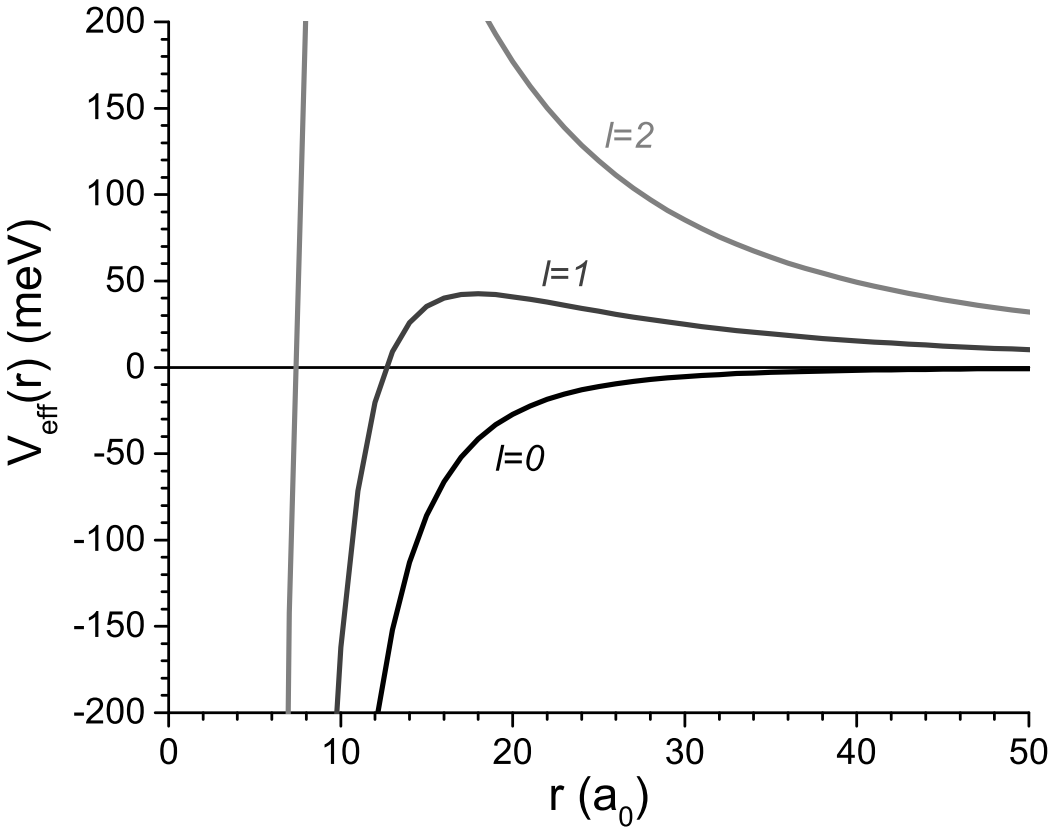

Figure 2.1: Calculated V_{eff} of the electron-Rb polarization interaction for $l = 0, 1, 2$.

For electron-Rb scattering, the energy-dependent S-wave and P-wave phase shifts $\delta_l(k)$ have been calculated by Khuskivadze et al. [1]. Their calculated scattering phase-shifts are shown in Fig. 2.2. The scattering of a Rydberg electron from a rubidium atom in its $5S_{1/2}$ ground-state has both S-wave singlet $^1S_0$ and triplet $^3S_1$ scattering channels. These correspond to a total spin S=0 scattering channel, in which the combined spin of the Rydberg electron and $5S_{1/2}$ electron equals 0, and three total spin S=1 channels, in which their total spin equals 1, respectively. The P-wave also has singlet $^1P_1$ scattering and triplet ^3P_J scattering, where $J = 0, 1, 2$ is the spin-orbit splitting of the triplet P scattering phase shifts.

In Fig. 2.2, the P-wave shape resonance occurs at an energy where the ^3P scattering phase shift approaches $\pi/2$, leading to a divergence of the scattering length (Eq. 2.40). Another interesting feature is the Ramsauer-Townsend zero crossing of the ^{3}S-wave phase shift at an energy near 42 meV. There, the scattering length goes to zero and the electron and rubidium atom become non-interacting, essentially passing right through each other. Generally, both of these scattering features do not immediately affect the low-energy molecular states studied in this work but do account for distinct features in the molecular adiabatic potentials described below and in Chapters IV and V.

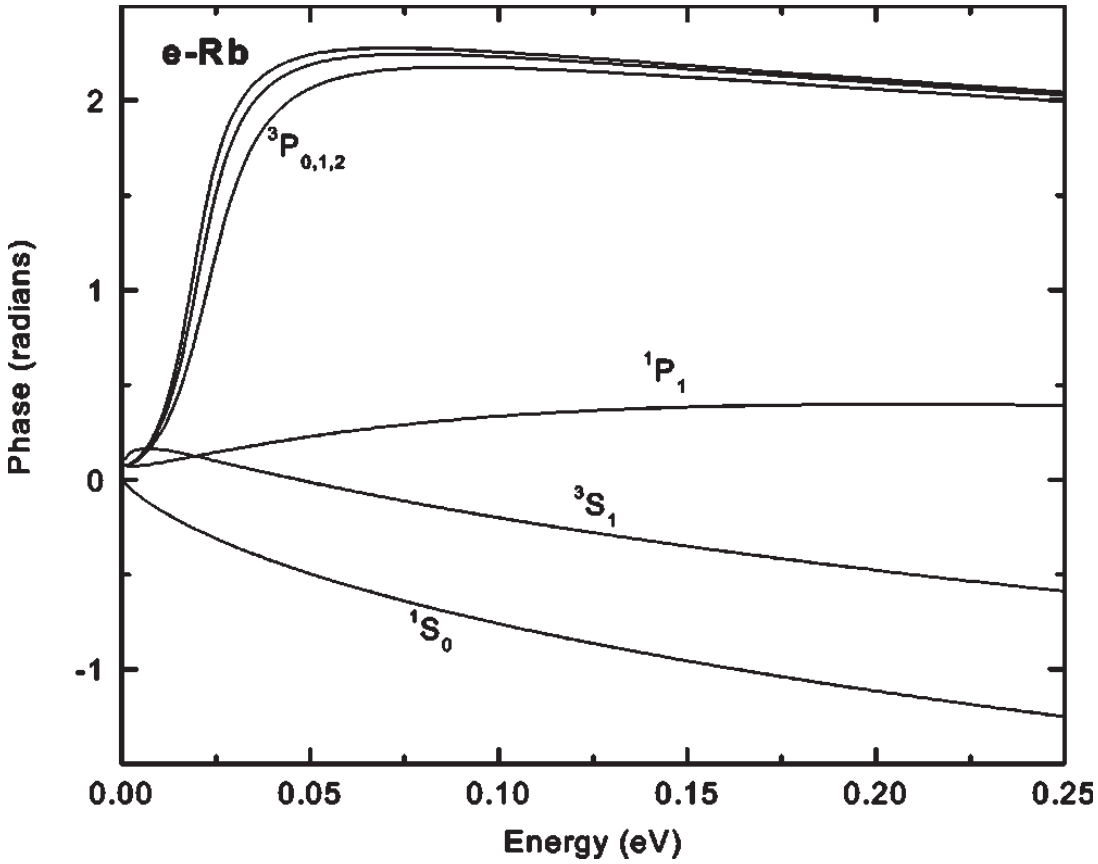

Figure 2.2: Calculated S-wave and P-wave phase shifts for low-energy electron-Rb scattering as a function of energy [1].

2.4.3 Adiabatic molecular potentials and bound states

The nature of the binding interaction between a Rydberg electron and ground-state atom was first described by Fermi [10] to help explain pressure-induced energy shifts of absorption lines of Rydberg atoms in a high-pressure environment [9]. In Fermi's treatment, the deBroglie wavelength of the Rydberg electron (position $\mathbf{r}$) is much larger than that of a heavy ground-state atom (position $\mathbf{R}$) that lies within the Rydberg atom's volume, and their interaction is approximated as a low-energy S-wave scattering process. The interaction can be described using an S-wave Fermi-type potential of the form

$$V_{\text{pseudo}}(\mathbf{r}) = 2\pi A_s(k)\,\delta^3(\mathbf{r}-\mathbf{R}), \tag{2.44}$$

where $A_s(k)$ is the energy-dependent S-wave scattering length for the electron-atom scattering interaction. As was pointed out by Omont and again by Greene et al. [4, 12], for negative values of $A_s(k)$ the interaction can lead to bound molecular states. In their models, they used that fact that for the scattering of a low-energy electron with a polarizable atom (i.e. for r^{-4} potentials), the scattering length can be expressed in a form independent of the scattering phase shifts as [78]

$$A_{l=0}(k) = A_{s0} + \frac{\pi\alpha}{3}k + O(k^2), \tag{2.45}$$

where A_{s0} is the zero-energy S-wave scattering length and α is the polarizability of the perturbing atom. The scattering length depends on the relative spins of the Rydberg electron and ground-state atom. For S-wave electron-Rb scattering, predicted and measured values of the triplet scattering length A_{s0}^T range from -13 to -19.48 a_0 [16, 17, 18, 20, 29], leading to attractive interactions. Predicted values for the singlet scattering length A_{s0}^S range from 0.627 to 2.03 a_0 [16, 17], which are small and positive, giving rise to weak repulsive interactions.

Figure 2.3 shows the adiabatic molecular potential of the ^{87}Rb$(34D_{5/2} + 5S_{1/2})$ low-

ℓ molecule calculated for the S-wave Fermi-type interaction potential in Eq. 2.44 with $A_{s0}^{T} = -14.0\mathrm{a}_0$. The internuclear axis is chosen along $\mathbf{R} = Z$. The interaction results in oscillatory potential curves that largely mimic the behavior of the Rydberg atom wave function, with localized potential minima deep enough to sustain weakly-bound vibrational states. The outermost well of the adiabatic potential curve centered at 2000 a_0 coincides with the outermost lobe of the 34D Rydberg wave function. There, the Rydberg electron energy is small ($\lesssim$ 1meV) and the potential is dominated by S-wave scattering. The $\nu = 0$ vibrational ground-state in this potential well is also shown which has a binding energy of about 46 MHz. Generally, the outermost well of the adiabatic potential curves for low-ℓ Rydberg molecules is little affected by P-wave and higher-order partial waves and the Fermi-type S-wave model used here suffices to model molecular spectra. At smaller internuclear separations the higher kinetic energy of the electron causes the inner wells to be substantially modified by P-wave scattering channels, and for high resolution spectroscopy on molecular states in these inner potentials the S-wave Fermi-model is insufficient. The effects of P-wave scattering on the molecular states of interest here are discussed in Chapter V. At and internuclear separation around 750 a_0, one also sees that the molecular potential crosses zero as a consequence of the Ramsauer-Townsend zero in the ^{3}S-wave phase shift.

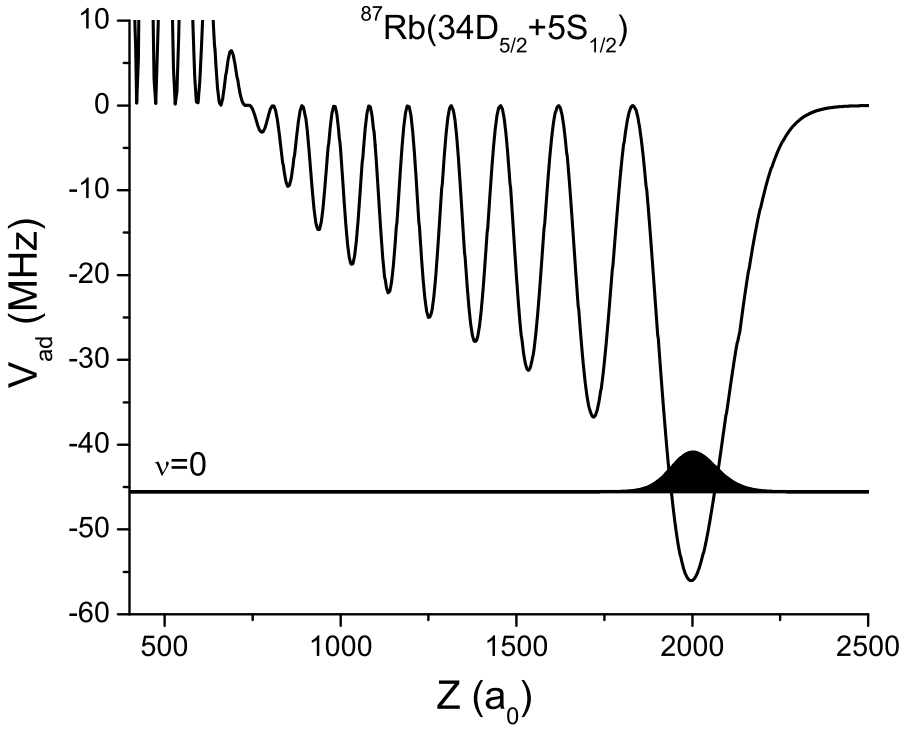

Figure 2.3: Calculated S-wave adiabatic potential for the ^{87}Rb($nD_{5/2}+5S_{1/2}$) molecule with $A_{s0} = -14.0\mathrm{a}_0$ and $\alpha_{Rb} = 319$ a.u., and the $\nu = 0$ vibrational wave function.

In addition to their electronic and vibrational structure, diatomic molecules also have rotational structure. Due to their large internuclear separations and large nuclear masses, the rotational energies of long-range diatomic Rydberg molecules are small. The rotational energies of diatomic molecules can be estimated by considering a rigid rotor model with the Hamiltonian operator [79]

$$H_{rot} = B\hat{J}^2, \tag{2.46}$$

where $\hat{J}$ is the (dimensionless) angular-momentum operator and the rotational constant $B = \hbar^2/2I = \hbar^2/2\mu R^2$. Here I is the molecule's moment of inertia, R the average separation of the two atoms and μ their reduced mass. Schrödinger's equation and the molecular rotational energies are then given by

$$\frac{\hbar^2}{2\mu R^2}\hat{J}^2\psi(\theta,\phi) = E_{rot}\psi(\theta,\phi) \tag{2.47}$$

$$E_{rot} = BJ(J+1), \tag{2.48}$$

where the energy levels are spaced in intervals of $2B$. For the $^{87}Rb_2$ long-range Rydberg molecules investigated here, $\mu = m_{Rb}/2 = 43.5$ amu and $R \approx 2000\ a_0$ giving $B/h = 10.4$ kHz. From this we see that the rotational energies are smaller than the vibrational energies by more than an order of magnitude. Since the spectroscopic resolution in the experiments presented here is limited to $\sim$ 1MHz by laser line widths, the rotational level structure cannot be resolved and is therefore not considered.

2.4.4 Hund's coupling cases

In Chapters IV and V of this work I investigate the influence of angular-momentum couplings on the properties of long-range D-type Rydberg molecules. Hund's coupling cases [80] are widely used for the classification of angular-momentum couplings in diatomic molecules [79]. These cases are idealized angular-momentum coupling cases in which specific coupling terms in the molecular Hamiltonian dominate over other terms. As a result, they play an important role in the theory underlying the analysis of molecular spectra and in determining molecular properties. The five Hund's cases (a) through (e) are traditionally defined using the following angular momenta of the molecule:

- L is the electronic orbital angular momentum
- S is the electronic spin
- $J_a = L + S$ is the total electronic angular momentum
- J is the total angular momentum of the molecule
- $R = J - L - S$ is the rotational angular momentum of the nuclei

The diatomic long-range Rydberg molecules of interest here exhibit a wide range of Hund's coupling cases. Due to the small rotational energies of the molecules in this work, rotational coupling in long-range Rydberg molecules is not considered and the Hund's cases used to describe the molecules are restricted to $R = 0$ and $J = J_a$. Hund's cases (d) and (e) describe

configurations for dominant couplings with R and therefore the relevant Hund's cases here are cases (a), (b), and (c). Figure 2.4 shows vector angular-momentum-coupling diagrams for these cases.

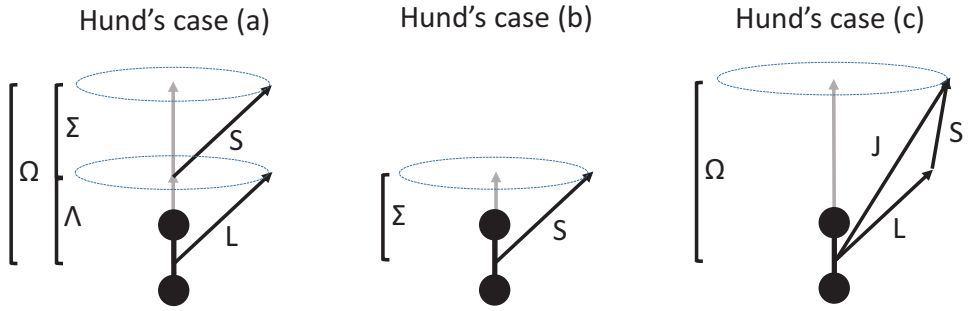

Figure 2.4: Vector angular-momentum coupling diagrams for Hund's cases (a), (b), and (c) with $R = 0$.

Hund's case (a) describes a situation where L and S are decoupled and each is strongly coupled to the internuclear axis. In the description of diatomic molecules the natural choice for a quantization axis is the internuclear axis. The projections of L and S onto the internuclear axis are Λ and Σ, respectively, and their sum $\Omega = \Lambda + \Sigma$. In this case J is not a good quantum number. Hund's case (b) describes a configuration where the LS coupling vanishes due to $\Lambda = 0$ as well as situations where $\Lambda \neq 0$ but the coupling between S and the internuclear axis is small. In Fig. 2.4 this case is shown for $L = 0$, where the projection of the total angular momentum onto the internuclear axis reduces to Σ. Hund's case (c) describes a situation in which the LS coupling is stronger than the coupling to the internuclear axis, making J a good quantum number. Here, Λ and Σ are not well defined, and Ω denotes the projection of J onto the internuclear axis.

Hund's cases are idealized cases and in most diatomic molecules the coupling configurations are intermediate cases. Long-range Rydberg molecules exhibit a broad range of Hund's cases which are distinguished by the relative strength of the angular-momentum couplings in the constituent Rydberg and ground-state atoms compared to the scattering-induced binding interaction between the Rydberg electron and ground-state atom. This is exemplified in

rubidium D-type Rydberg molecules which exhibit a transition between Hund's cases (a) and (c) as the n of the Rydberg atom is increased and its fine-structure begins to dominate the scattering-induced binding interaction. The details of this transition behavior are discussed in Chapters IV and V.

CHAPTER III

Experimental methods

The preparation of rubidium Rydberg and ground-state atoms at low temperature is central to the experiments in this dissertation. A common approach to making cold Rydberg atoms is to first prepare a sample of cold ground-state atoms and then photo-excite the ground-state atoms to Rydberg states. Because the process of optically exciting ground-state atoms to Rydberg states is accomplished with minimal energy and momentum transfer to the atoms, the temperature of the resulting Rydberg atoms is typically limited by how cold one can make the ground-state atom sample. Using established atom-cooling techniques, this readily allows the production of Rydberg atoms at μK temperatures and below. In part of this work, I am specifically interested in interactions between cold Rydberg and ground-state atoms, and the formation of long-range Rydberg molecules via these interactions. This requires a sufficiently high density of ground-state atoms such that the average interatomic separation of ground-state atoms becomes comparable to the size of the Rydberg atom. The generation of magnetically-trapped ground-state atom samples at low temperature is also a prerequisite to producing and trapping cold circular state Rydberg atoms by the technique described in Chapter VI. In this Chapter, I first review the cooling steps used to prepare low temperature ground-state atom samples at high density in a magnetic trap. The experimental apparatus, laser systems, and cooling steps used for the experiments have been described in detail by previous students [2, 81] so the discussion here is kept brief. The

photo-excitation, field-ionization and detection of Rydberg atoms and molecules are then described. In the final section I describe the calibration of electric fields in the experiments using Stark spectroscopy on high-lying Rydberg states.

3.1 Preparation of cold rubidium ground-state atoms

3.1.1 Laser cooling

A schematic of the experimental apparatus is shown in the left panel of Fig. 3.1. In all the experiments, ^{87}Rb atoms are first collected from a background rubidium vapor and cooled to $\sim 150\mu$K in a pyramidal magneto-optical trap (MOT) [82, 83, 84]. The pyramidal MOT acts as a low-velocity intense source [85] by emitting an effusive atomic beam directed along $\mathbf{y}$ to load a second MOT located 35 cm away in a separate experimental chamber at ultra-high vacuum ($< 2 \times 10^{-11}$ Torr). Both MOTs are operated on the $|5S_{1/2}, F = 2\rangle \rightarrow |5P_{3/2}, F = 3\rangle$ cooling transition [3] with the addition of a repumping laser on the $|5S_{1/2}, F = 1\rangle \rightarrow |5P_{3/2}, F = 2\rangle$ transition. A diagram of the relevant energy-level structure in ^{87}Rb is shown in the right panel of Fig. 3.1 with the optical transitions indicated. Over the course of 10 seconds, $\approx 2 \times 10^8$ atoms are collected in the second MOT at temperature T$\approx$ 150 μK and density of $\approx 10^9$ cm^{-3}. To increase the atom density, the secondary MOT is then compressed by simultaneously switching off the relatively weak MOT magnetic field and turning on a high-gradient ($\approx$ 50 G/cm) quadrupole magnetic field over the course of 50 ms using a U-wire configuration [86]. The compressed MOT is on for 20 ms with the laser frequencies detuned by an additional line width after which the cloud of atoms is about 2 mm in diameter and at a density of $\approx 10^{10}$ cm^{-3}.

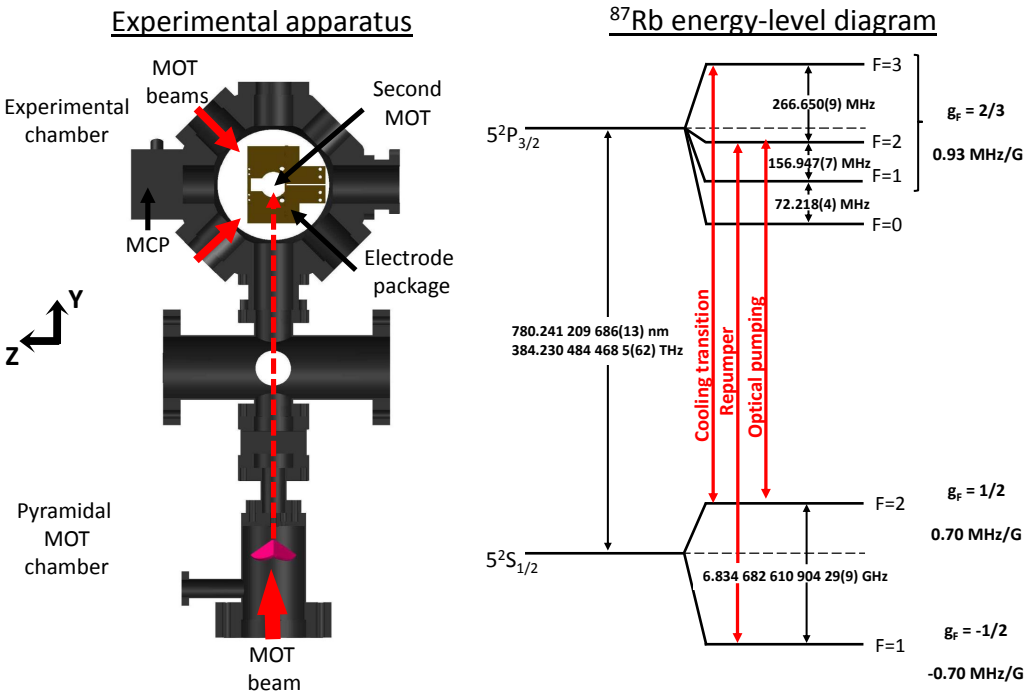

Figure 3.1: Left: Schematic of the experimental apparatus [2]. Right: ^{87}Rb hyperfine structure energy-level diagram. Frequency splittings, Landé g-factors for each level and their corresponding Zeeman splitting between neighboring magnetic sub-levels are indicated on the plot. Values are taken from [3].

Prior to switching on the magnetic trap, the atoms are further cooled by doing a 4 ms corkscrew optical molasses and then optically pumped to the $|F = 2, m_F = +2\rangle$ ground state on the $|5S_{1/2}, F = 2\rangle \rightarrow |5P_{3/2}, F = 2\rangle$ transition (see Fig. 3.1). For optimal transfer of the laser-cooled atoms into the magnetic trap, the atom cloud and magnetic trapping potential need to be mode matched. The mode-matched condition requires that the atoms have a temperature and Gaussian width σ_i along the ith dimension such that the kinetic energy of the atoms equals its average potential energy in the harmonic trap

$$\frac{k_B T}{2} = \frac{m\omega_i^2 \sigma_i^2}{2} \rightarrow \omega_i = \frac{1}{\sigma_i}\sqrt{\frac{k_B T}{m}}, \tag{3.1}$$

where ω_i is the trap frequency along i. For typical parameters of σ_i=1 mm, T=50 μK, and m=87 amu, the mode matched trapping frequency ω_i=69 Hz. Good transfer efficiency also requires that the atom cloud and magnetic trap are spatially overlapped so to avoid

oscillations of the atom cloud after the transfer that both heat the sample and delocalize the atom cloud during experiments. In practice, the aforementioned laser-cooling and magnetic trap parameters are adjusted iteratively to optimize the final atom number, density, and temperature in the magnetic trap.

3.1.2 Magnetic trap and evaporative cooling

The magnetic atom trap is generated using a Z-wire configuration [86], whose location is shown in the schematic of the experimental chamber in Fig. 3.3 below. A typical magnetic trapping field is shown in Fig. 3.2. Near the trap minimum, the magnetic trapping field is nearly harmonic and the trapping frequency along the $i = x, y, z$ direction is given by

$$\omega_i = \sqrt{\frac{\mu}{m}\frac{d^2|B|}{dr_i^2}} \tag{3.2}$$

where μ and m are the magnetic moment and mass of the atom. For ^{87}Rb atoms prepared in their $|F = 2, m_F = +2\rangle$ ground-state $\mu = \mu_B$ and the trapping frequency is determined by the magnetic trap curvature, which is set by appropriate choices of Z-wire current and magnetic bias fields. At the loading step, these parameters are chosen to fulfill the mode-matching condition above. It is also assumed that the atomic spins adiabatically follow the local magnetic field as the magnetic trapping field is switched on after optical pumping (i.e. the atoms do not undergo any "Majorana" spin flips into un-trapped or anti-trapped states)[1]. In experiments, the magnetic trap is loaded with $\sim 10^7$ atoms at a temperature of $\lesssim 100\mu$K and density of 10^{10} cm^{-3}. For a quantitative characterization of the magnetic trap, a direct measurement of the magnetic trapping frequencies is made by inducing center of mass oscillations of the trapped atom sample. This measurement is explained in detail in Chapter VI Section 6.2, in context with the circular Rydberg atom trapping experiment

[1]The adiabaticity condition can be expressed as $d\omega_L/dt << \omega_L^2$ [87], where ω_L is the Larmor frequency, and is readily satisfied for typical experimental parameters. Consider an $|F = 2, m_F = +2\rangle$ atom in a 10 Gauss field with $\omega_L/2\pi = 14$ MHz/Gauss. For a typical magnetic field switching time $\gtrsim 100\mu$s, this gives $d\omega_L/dt/\omega_L^2 \lesssim 10^{-3}$, which is well within the adiabatic limit.

where the magnetic trapping frequency plays an important role.

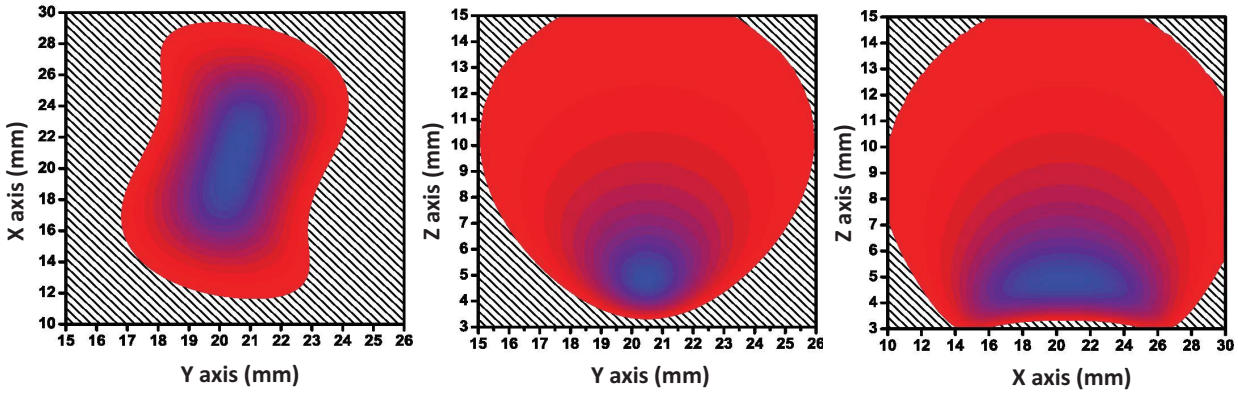

Figure 3.2: Counter plots of $|B|$ for three orthogonal planes through the center of the magnetic trap located 4 mm from the surface of the Z wire . Scale is 1 (blue) to 15 Gaus (red) in steps of 1 G; >15 G (hatched).

For the Rydberg molecule experiment, higher ground-state atom densities are needed. This is accomplished by doing forced radio-frequency (RF) evaporative cooling on the atom sample. The magnetic trap is adiabatically compressed followed by the application of an RF frequency ramp over the course of approximately 15 seconds. In the trap, atoms with higher kinetic energies sample the highest magnetic field strengths. As a result of the position-dependent Zeeman shifts in the magnetic trap, the RF field selectively transfers the hottest atoms from the $m_F = +2$ state to high-field seeking states via $\Delta m = -1$ transitions. These atoms get ejected from the trap and the remaining atoms re-thermalize at a lower temperature. The process continues as the RF frequency is ramped down until the desired temperature and density is reached. A typical frequency ramp starts at 20 MHz and ends at $\sim$1 MHz; the exact stop value of the RF frequency depends on the magnetic field strength at the bottom of the trap which is varied depending on the experiment.

3.1.3 Absorption imaging

Absorption imaging is used to measure the ground-state atom number, cloud size and temperature. In absorption imaging, the atom cloud is illuminated by a low intensity laser pulse resonant with the cooling transition and imaged on a CCD camera. A comparison of

the intensity of transmitted light with (I) and without (I_0) the atoms in the trap provides an image of the atom cloud from which its optical density is determined. The area density of the atoms along the direction of the imaging beam is given by [84]

$$N_a = \frac{1}{\sigma} \ln(I_0/I) \tag{3.3}$$

with the scattering cross section given by [84]

$$\sigma = \frac{\sigma_0}{1 + (2\Delta/\Gamma)^2 + (I/I_{sat})} \tag{3.4}$$

$$\sigma_0 = \frac{\Gamma \hbar \omega}{2 I_{sat}}, \tag{3.5}$$

where σ_0 is the on-resonance scattering cross section, Δ is the laser detuning from resonance, Γ and ω are the transition line width and frequency, respectively, and I_{sat} is the saturation intensity of the transition. In our imaging setup, the absorption laser drives the $m_F = \pm 2 \rightarrow m_F = \pm 3$ cycling transition on resonance, for which $I_{sat} = 1.67$ mW/cm^2 [3]. The beam intensity is set to $\approx I_{sat}/10$ to avoid saturating the transition and the scattering cross section $\sigma = 2.6 \times 10^{-9}$ cm^2. Under these conditions, each atom scatters photons at a rate $\gamma_p = 1.7 \times 10^6 s^{-1}$. For a typical laser pulse duration of 30μs this results in an average of ≈ 50 scattered photons, ensuring negligible Doppler broadening ($\lesssim 1$ MHz) on the probe transition during the imaging pulse.

3.2 Rydberg excitation and detection

In all the experiments, Rydberg atoms and molecules are optically excited out of the magnetically-trapped ground-state atom sample using a two-photon transition from the $5S_{1/2}$ ground state using nearly counter-propagating 780 nm and 480 nm laser beams. This is shown schematically in Fig. 3.3b. Since the entire ground-state atom preparation sequence (from the initial MOT loading stage to the end of the evaporative cooling) can take up to 30

seconds, a single magnetically-trapped atom sample is used for multiple Rydberg excitation and detection sequences (typically 100 to 1000). To minimize loss of phase-space density of the ground-state atom sample over the course of repeated optical excitations, the 780 nm laser frequency is fixed 1 GHz off-resonance from the $5S_{1/2}$ to $5P_{3/2}$. The 780 nm laser power is set to $\sim$500 μW and collimated to a full-width half-maximum (FWHM) of 3.5 mm, corresponding to an intensity of $\approx$ 0.5mW/cm^2. Under these conditions the off-resonant photon scattering rate on the $5S_{1/2} \rightarrow 5P_{3/2}$ transition is $\gamma_p \approx 50s^{-1}$. For a 1 μs excitation pulse this amounts to $< 10^{-3}$ photon scattering events and negligible heating of the atom sample over the course of one excitation series. With the 780 nm at a fixed frequency, the 480 nm laser frequency is scanned to excite Rydberg levels. The 480 nm beam has a power of $\sim$35 mW and is focused to a FWHM of 89 ± 5 μm into the atom sample. The combined excitation bandwidth of the 780 nm and 480 nm lasers is $\approx$2 MHz.

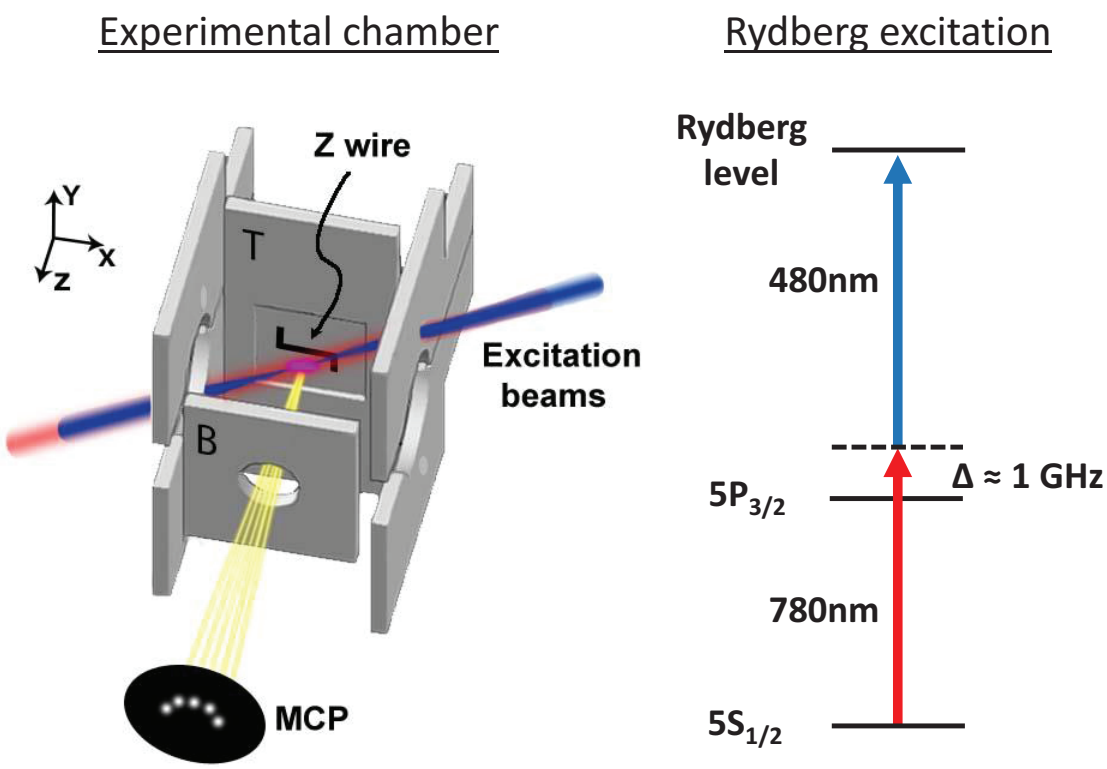

Figure 3.3: Left: Experimental chamber with the Z wire, counter-propagating 480nm and 780nm Rydberg excitation beams, and MCP are labeled. Six gold-coated copper electrodes (gray) enclose the trapped atom sample to control the electric fields in the experimental volume. The electrodes labeled "T" and "B" are used for field-ionization of Rydberg atoms and the electric-field ramp in circular state production (see Chapter VI), respectively. Right: ^{87}Rb energy-level diagram for off-resonant two-photon excitation through intermediate $5P_{3/2}$ state.

Since the optical absorption cross sections for atomic transitions to Rydberg states are small, spectroscopy on Rydberg states is typically done by detecting the Rydberg atoms in a single-atom counting scheme. A common approach takes advantage of the reduced binding energies ($\sim n^{*-2}$) of the Rydberg electron, which can be ionized by modest electric fields of tens to hundreds of V/cm. Application of an electric-field pulse after the optical Rydberg excitation ionizes the Rydberg atom, leaving a free electron and positively-charged ion either of which can then be detected.

The ionization behavior of Rydberg atoms is generally a complex process that depends on the rise time and shape of the electric field pulse and the initial Rydberg state [56].

As the electric field is increased, the initial Rydberg state traverses the Stark map until it reaches the ionization threshold for the state it is in. In alkali atoms, the Stark states exhibit avoided crossings due to non-zero quantum defects and the atom can pass through the avoided crossings adiabatically or diabatically, depending on its size and how fast the electric field is changing (i.e. its slew rate). As a result, the field-ionization behavior of low-ℓ and high-ℓ Rydberg states is generally different. Low-ℓ states exhibit relatively large avoided crossings due to their large quantum defects and tend to field ionize adiabatically at the classical field ionization threshold

$$E_{classical} = \frac{1}{16n^{*4}}. \tag{3.6}$$

High-ℓ states, on the other hand, exhibit much narrower avoided crossings and the field ionization behavior tends to be more diabatic. In the diabatic limit, the ionization electric fields of blue-shifted and red-shifted high-ℓ states are

$$E_{Blue} = \frac{1}{4n^{*4}} \tag{3.7}$$

$$E_{Red} = \frac{1}{9n^{*4}}. \tag{3.8}$$

A schematic of the anderson.da@gmail.com experimental chamber is shown in the left panel of Fig. 3.3. For all the experiments in this dissertation, Rydberg atoms are field-ionized by application of a positive voltage pulse to the "T" electrode located within a few millimeters from the atom sample. Once ionized, the field extracts the resulting ions into a multichannel plate (MCP) detector located 10 cm from the excitation region. The MCP detector provides information on the ion number, arrival time, and spatial distribution of the ion signal.

3.3 Electric field control

Controlling external electric fields is important in all the experiments described in this dissertation. In the spectroscopy of long-range Rydberg molecules, the fields need to be reduced to levels that ensure Stark shifts and broadenings of the atomic Rydberg lines do not obscure the molecular signals. In the circular state experiment, the electric field plays an essential role in the crossed-fields method used to generate the circular Rydberg atoms.

In this work, electric fields are controlled using six individually-addressable electrodes surrounding the experimental region, shown in the left panel of Fig. 3.3. Voltage-to-field calibration factors for the electrodes and field zeros are obtained by measuring the Stark shifts of high-lying Rydberg states as a function of voltage applied to the electrodes. Figure 3.4 shows calculated and experimental Stark maps for $90D$ Rydberg states excited in a trapped atom sample located $\approx$ 3 mm from the "T" electrode. The Stark maps are plots of the Rydberg signal as a function of 480 nm laser frequency offset (vertical axis) and electrode voltage (bottom horizontal axis). A comparison of the experimental and calculated Stark maps gives the corresponding electric field values (top horizontal axis). The Stark maps are symmetric about zero electric field, and from the data in Fig. 3.4 and in similar measurements the field zero is determined to within $\leq$30 mV/cm in all three coordinates.

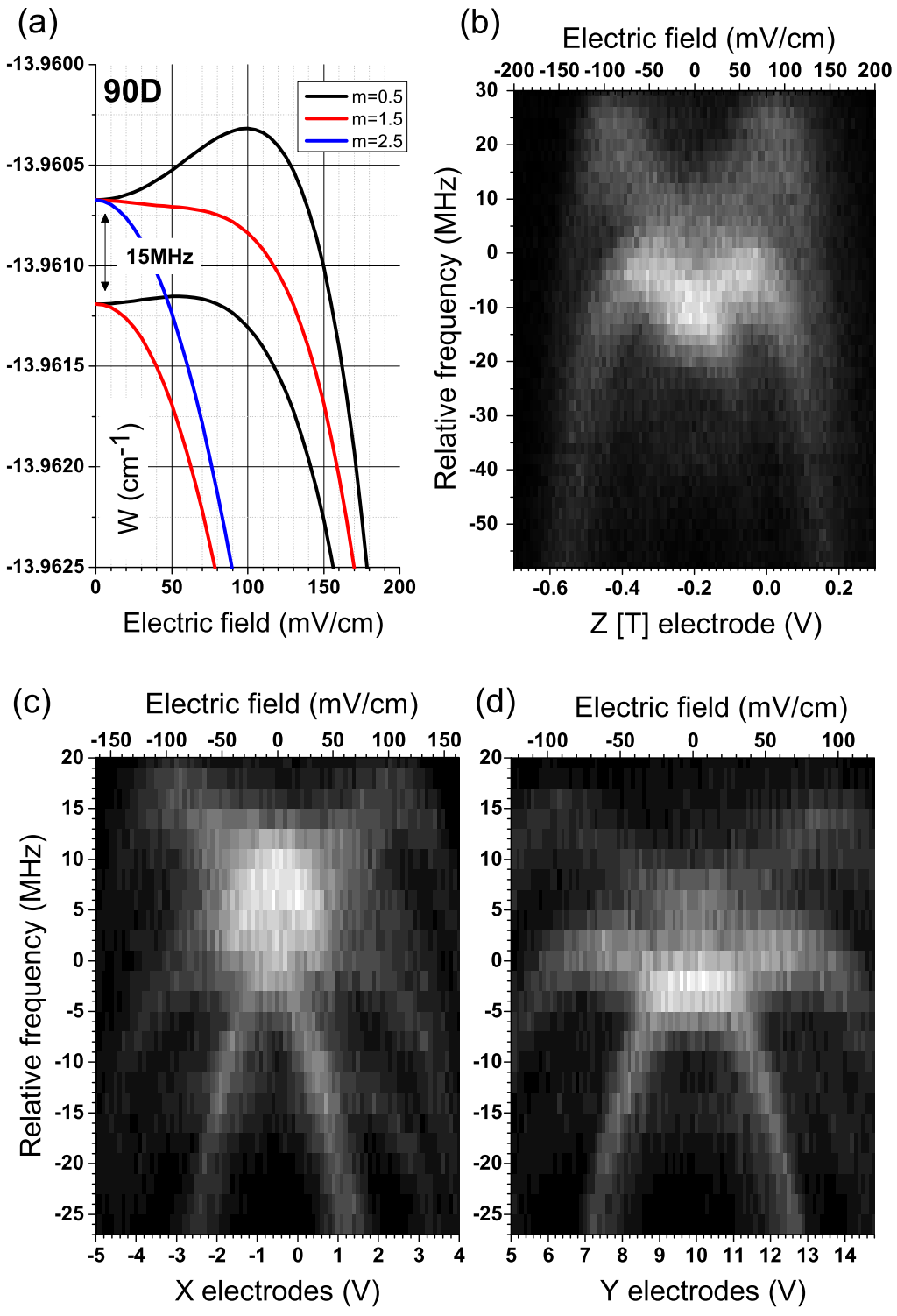

Figure 3.4: Stark spectroscopy on 90D Rydberg states in rubidium: a) Calculated Stark map, b-d) Experimental Stark maps for electric fields generated along the X, Y, and Z coordinates.

CHAPTER IV

Long-range D-type Rydberg molecules

In this chapter I describe an experimental study of long-range rubidium Rydberg molecules formed between an D-state Rydberg and a $5S_{1/2}$ ground-state atom . The molecules are photoassociated out of a cold gas of ^{87}Rb atoms. The vibrational ground-state binding energies of the $^{87}\mathrm{Rb}(nD+5S_{1/2})$ molecules are measured for principal quantum numbers $34\leq n\leq 40$. The binding energies are found to be larger than those of their $^{87}\mathrm{Rb}(nS+5S_{1/2})$ counterparts, showing the dependence of the molecular bond on the angular momentum of the Rydberg atom. A Fermi model including the triplet S-wave scattering of the Rydberg electron with the $5\mathrm{S}_{1/2}$ atom, fine-structure coupling of the Rydberg atom, and hyperfine structure of the $5\mathrm{S}_{1/2}$ atom is used to describe the experimentally determined binding energies. Molecular spectra and calculated binding energies are in good agreement and reveal the transition of $^{87}\mathrm{Rb}(nD+5S_{1/2})$ molecules from a molecular-binding-dominant regime at low n [Hund's coupling case (a)] to a fine-structure-dominant regime at high n [Hund's coupling case (c)]. Finally, broadening mechanisms relevant to the experimental spectra are discussed.

4.1 Experiment

This experiment is performed following the methods described in Chapter III. To excite nD Rydberg molecules we first prepare a sample of $\sim 10^5$ magnetically trapped ^{87}Rb atoms in

their $|F{=}2, m_F{=}2\rangle$ ground state at a temperature $\leq$17 μK and peak density $\gtrsim 5\times10^{11}$ cm^{-3}. Optical excitation to atomic and molecular nD Rydberg states is accomplished via a two-photon transition from the $5S_{1/2}$ ground state using 780 nm and 480 nm laser beams, shown schematically in Fig. 4.1a. The 780 nm laser frequency is fixed $\sim$1 GHz off-resonance from the $5S_{1/2}$ to $5P_{3/2}$ transition, and the 480 nm laser frequency is scanned to excite either Rydberg atoms or molecules. The combined excitation bandwidth of the 780 nm and 480 nm lasers is $\approx$2 MHz. The 780 nm laser has a power of $\sim$500 μW and is collimated to a full-width half-maximum (FWHM) of 3.5 mm. The 480 nm beam has a power of $\sim$35 mW and is focused to a FWHM of 89 ± 5 μm into the atom sample, which has a FWHM diameter of 28 μm and an aspect ratio of $\approx$ 1 : 5. The electric field is zeroed in the excitation region to within $\lesssim$200 mV/cm by Stark spectroscopy on $59D$ Rydberg states, as described in Chapter III, which ensures that quadratic Stark shifts of the nD Rydberg levels in the n range of interest are $\lesssim$2 MHz. A diagram of the experimental timing sequence is shown in Fig. 4.1b. In a single experiment, the atom sample is illuminated by 2-3 μs long laser pulses followed by electric-field ionization of Rydberg atoms and molecules [56]. The signal ions are extracted by the ionization field and detected by a micro-channel plate located 10 cm away. A single ground-state atom sample is used for a series of 55 individual experiments at a single 480 nm frequency step, ensuring that the density loss during one optical excitation series is negligible.

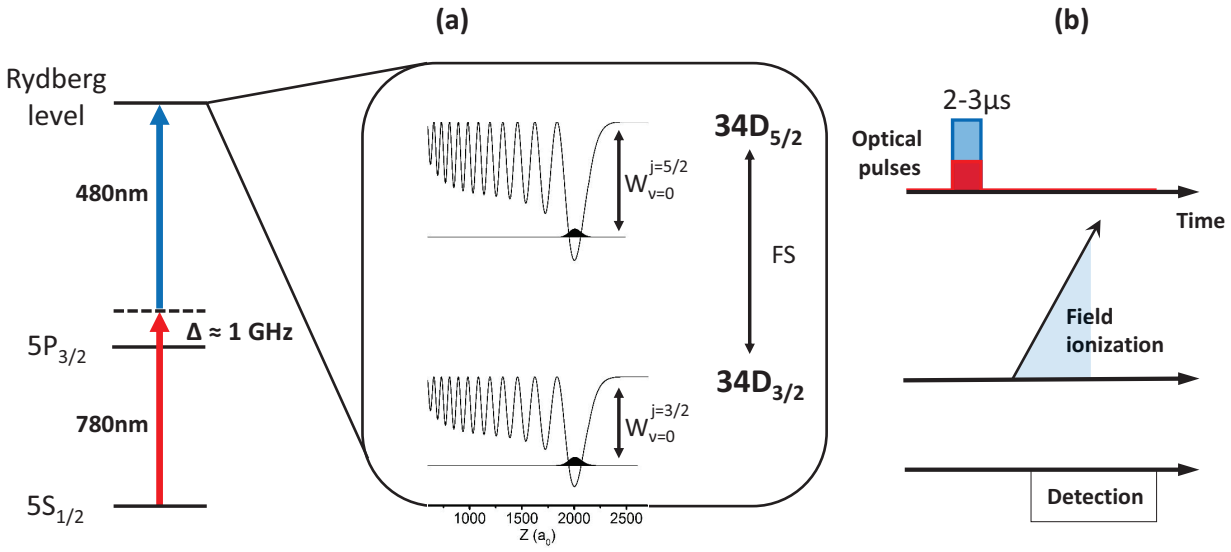

Figure 4.1: a) Schematic of the two-photon excitation to Rydberg and molecular states. The zoomed in region shows the 34D Rydberg fine structure (FS) states and their associated adiabatic S-wave molecular potentials. The binding energy $W_{\nu=0}$ of the $\nu = 0$ vibrational molecular bound-state for each FS component is defined relative to the dissociation threshold equal to the respective Rydberg state energy, as labelled; (b) Schematic of the experimental timing sequence for Rydberg excitation, field-ionization and detection.

4.2 Molecular binding energies

The photoassociation of a Rydberg atom and ground-state atom pair into a bound molecular state occurs when the excitation laser is detuned from the atomic Rydberg line by an amount equal to the molecular binding energy. This is shown schematically in Fig. 4.1a. An experimental spectrum in the vicinity of the atomic $35D_{5/2}$ Rydberg line is shown in Fig. 4.2. The observed spectral lines are fitted by a Gaussian function to obtain the line centers and σ widths; the errors of the line centers are taken to be equal to the average long-term frequency drift over one full frequency scan of the 480 nm laser which is measured separately. In Fig. 4.2, a prominent satellite line emerges at -38 ± 3 MHz, which is assigned to the $(35D_{5/2} + 5S_{1/2})(\nu = 0)$ molecule, where $\nu = 0$ denotes the vibrational ground state. This binding energy is ≈ 1.6 times larger than that of the $(35S_{1/2} + 5S_{1/2})(\nu = 0)$ molecular state measured in previous experiments [20, 29]. This increase in the binding energy is a

direct consequence of the increased ℓ. Within the low-ℓ class of Rb_2 Rydberg molecules, the nD ones have the highest binding energies due to the $\sqrt{2\ell+1}$-scaling of the angular wave functions $Y_l^{m=0}(\theta = 0)$. On a qualitative level, this can be explained by the more concentrated electron probability density of Rydberg D-states at the location of the perturbing atom compared to that of the Rydberg S-states.

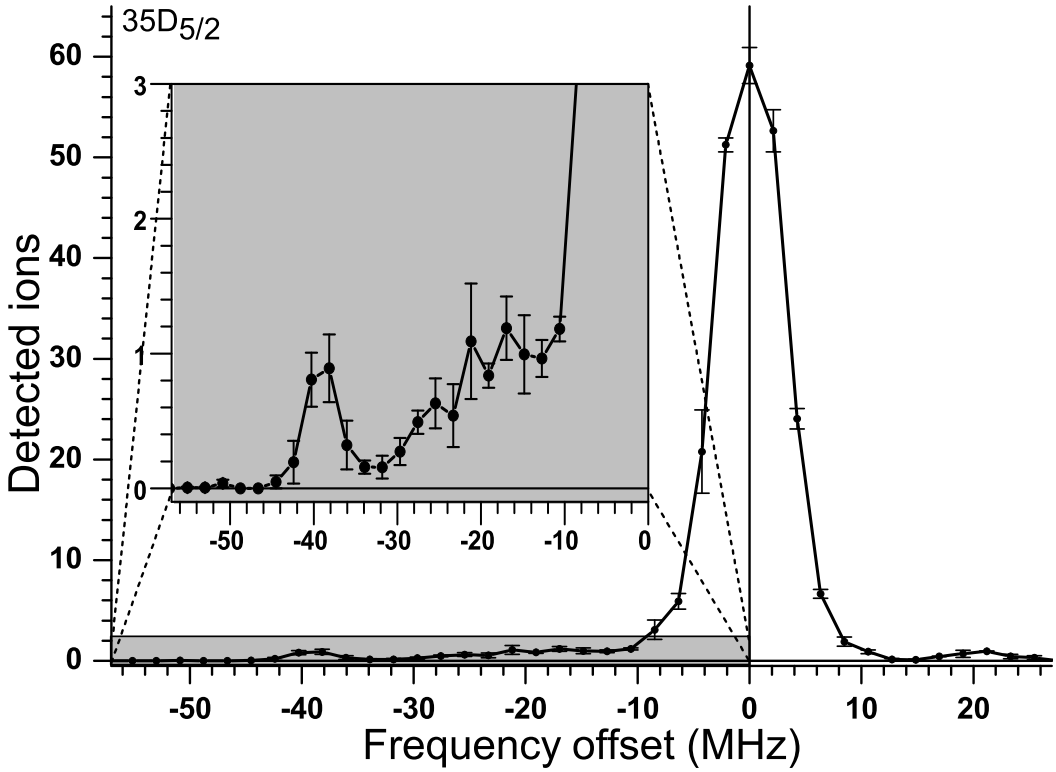

Figure 4.2: Spectrum centered on the $35D_{5/2}$ atomic Rydberg line showing the ^{87}Rb($35D_{5/2}$+ $5S_{1/2}$)($\nu = 0$) molecular line at -38 ± 3 MHz. The vertical error bars are the standard error of 3 sets of 55 individual experiments at each frequency step. The error in the binding energy is equal to the average long-term frequency drift observed over one full scan.

A series of $nD_{5/2}$ Rydberg spectra for $34 \leq n \leq 42$ is shown in Fig. 4.3 (right). The lowermost, red-shifted lines for n=40 and below are assigned to the molecular states. Molecular lines are not discernable in the n=42 and 41 spectra because the line broadening due to residual fields and the laser line width exceeds the molecular binding energies for these states. Additional satellite lines corresponding to other vibrational molecular states are expected (see section 5.3 in Chapter V), but are likely obscured in the spectra shown in

Figs. 4.2 and 4.3 by the broadening of the atomic Rydberg lines as well as artificial signals at ±20 MHz due to weak, symmetric side peaks in the 480nm laser spectrum from a Pound-Drever-Hall stabilization loop. Due to this, the features near −20 MHz are only assigned to molecular lines if they are significantly stronger than the artificial signal at +20 MHz.

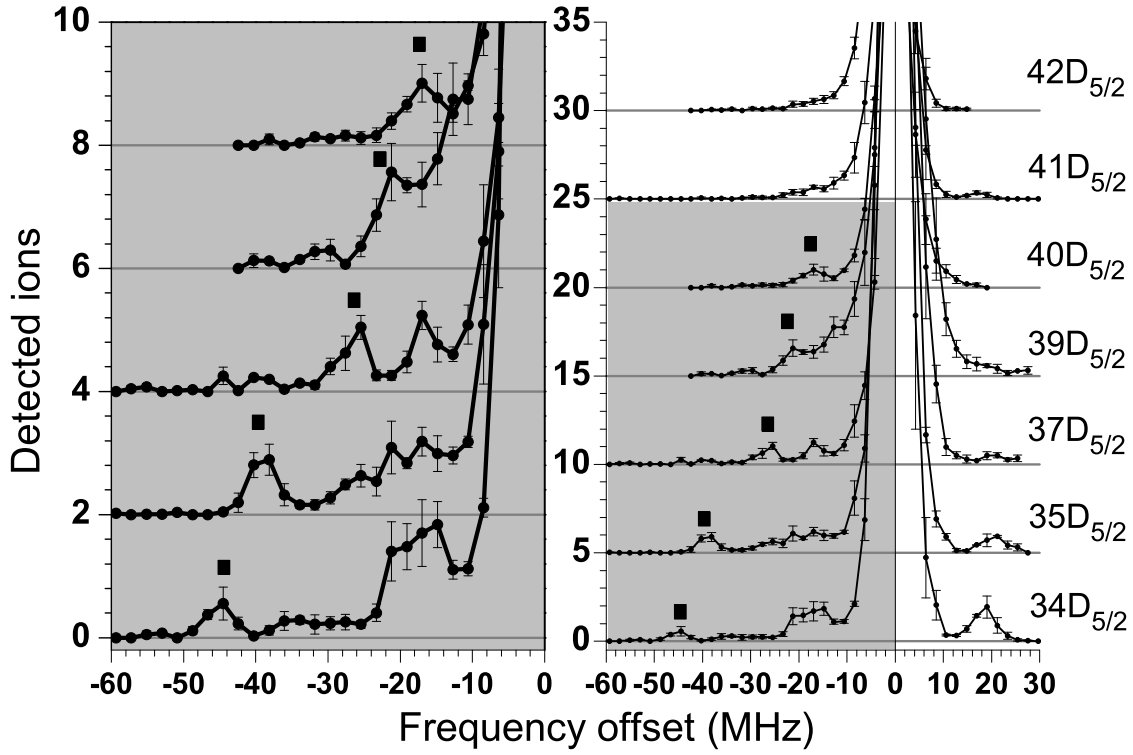

Figure 4.3: Right: Spectra centered on $nD_{5/2}$ atomic Rydberg lines for the indicated values of n and identified molecular lines (squares). Left: Selected spectra from plot on right for states with identified molecular lines. Error bars are obtained as in Fig. 4.2.

Fig. 4.4a shows the molecular binding energies measured in Fig. 4.3 versus n. One may expect these binding energies to be proportional to the probability density of the Rydberg electron wave function, which scales as the inverse of its volume $\sim n^{-6}$. An allometric fit to the data in Fig. 4.4a (black curve) qualitatively supports this expectation over the displayed range of n.

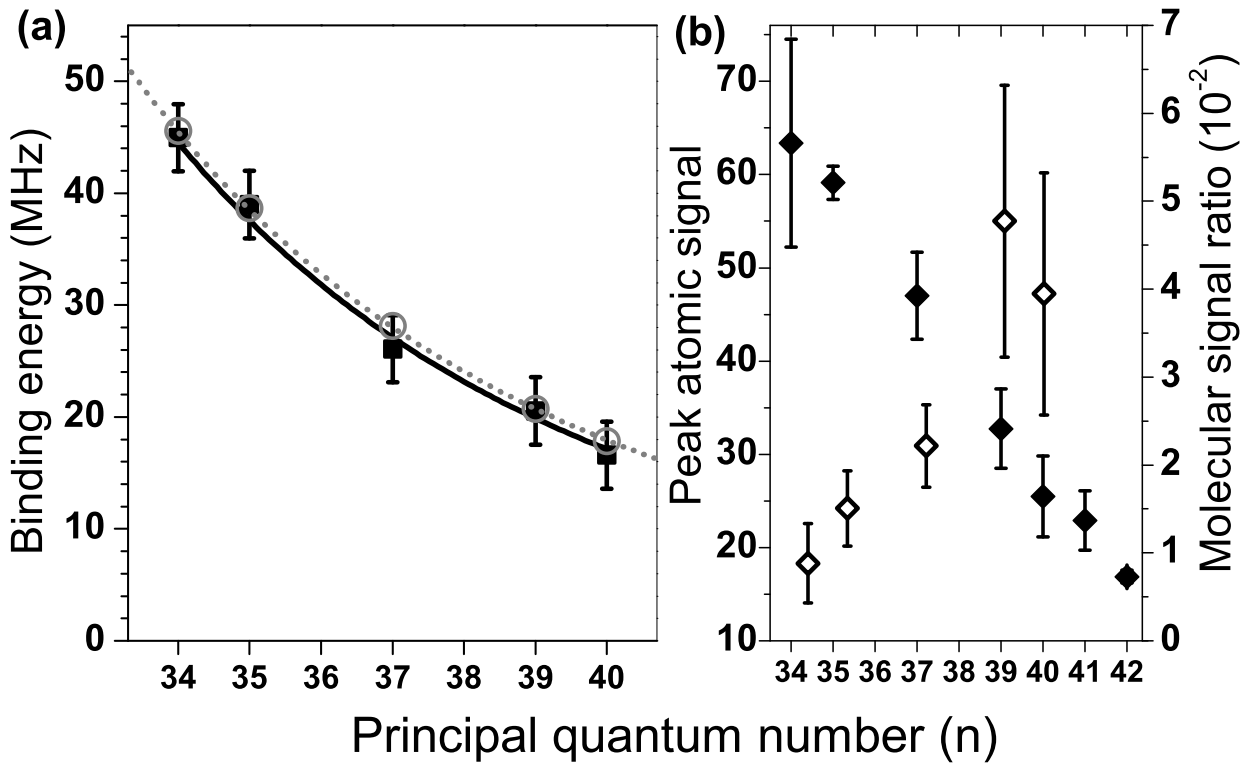

Figure 4.4: (a) Binding energies obtained from Gaussian fits to the molecular lines identified in Fig. 4.3 vs n. An allometric fit (solid curve) to the experimental binding energies yields a $n^{-5.9\pm0.4}$ scaling. Also shown are theoretical binding energies for the ^{87}Rb($nD_{5/2}$+$5S_{1/2}$)(ν = 0) molecular states with A_{s0}=−14 a_0 (hollow circles and dotted curve). (b) Peak number of detected ions on the $nD_{5/2}$ atomic Rydberg line (solid diamonds, left axis) and ratio of molecular and atomic line strengths (hollow diamonds, right axis) vs n.

As shown in Fig. 4.4b, the ratio of molecular and atomic line strengths ranges from $\approx 1-5\%$. Taking the peak atomic density in the experiment into consideration, this agrees quite well with the relative signal strengths of previous experiments with S-type molecules [20, 29]. Qualitatively, one may expect the molecule-Rydberg atom signal strenth ratio to scale with the probability of finding a $5S_{1/2}$ atom within the Rydberg-atom volume (which scales as n^6), corresponding to an increase of about a factor of 2.5 over the n-range in Fig. 4.4b. The observed increase, however, is significantly larger, namely by about a factor of 5. This enhancement is likely due to a Rydberg excitation blockade caused by electrostatic Rydberg-atom interactions [68, 70], which suppresses the atomic line [67]. Since the blockade's effectiveness increases with n, the molecular-signal ratio scales faster than n^6. This

interpretation is corroborated by the atomic-signal strength, which drops by a factor of 4 over the n-range in Fig. 4.4b. In the absence of an excitation blockade, the atomic signal would drop as n^{-3}, *i.e.* by only a factor of 2 in Fig. 4.4b. The suppression of the Rydberg line due to the blockade prevents a direct measurement of excitation probabilities to the molecular states from the relative signal strengths in Fig. 4.4b.

4.3 An S-wave Fermi model

For a quantitative description of the experimental data, the binding energies are calculated using a Fermi-type model that includes the S-wave triplet scattering between the Rydberg electron and ground-state atom, the fine-structure coupling of the Rydberg atom, and the hyperfine structure of the ground-state atom. The Rydberg atom's fine structure and the perturber's hyperfine structure are included because they are on the same order or larger than the molecular binding. For low Rydberg electron momenta, k, the S-wave triplet scattering length is taken to first order in k as $A_s^T(k) \approx A_{s0} + \frac{\pi}{3}\alpha k$ [12], where $A_{s0} = A_s^T(k=0)$ is the zero-energy scattering length and α is the polarizability of the perturbing Rb $5S_{1/2}$ atom. The P-wave scattering interaction strongly influences the inner part of the molecular potentials [19] but leaves the outermost well, where the bound states relevant to this work are found, largely unaffected. It is therefore not included in the model at this time. The P-wave interaction is included in the theoretical study presented in Chapter V where its effects on the molecular potentials and properties are discussed. For the $5S_{1/2}$ atom located at $\mathbf{R} = Z\mathbf{z}$, the Hamiltonian is

$$\hat{H}_0 + 2\pi A_s^T(k(r))\delta^3(\mathbf{r} - Z\mathbf{z})(\hat{\mathbf{S}}_1 \cdot \hat{\mathbf{S}}_2 + \frac{3}{4}) + A\hat{\mathbf{S}}_2 \cdot \hat{\mathbf{I}}_2 \tag{4.1}$$

where the unperturbed Hamiltonian $\hat{H}_0$ includes Rydberg quantum defects and fine structure [56]. The operators $\hat{\mathbf{S}}_1$ and $\hat{\mathbf{S}}_2$ are the spins of the Rydberg electron and $5S_{1/2}$ atom, respectively. The ^{87}Rb $5S_{1/2}$ atom has $\ell_2 = 0$, a nuclear spin $\hat{\mathbf{I}}_2$ with $I_2 = 3/2$, and a hyperfine

parameter $A = h \times 6.8$ GHz$/F_> = h \times 3.4$ GHz (in SI units). The projector $\hat{\mathbf{S}}_1 \cdot \hat{\mathbf{S}}_2 + \frac{3}{4}$ has the eigenvalue one (zero) for the triplet (singlet) states of $\hat{\mathbf{S}}_1$ and $\hat{\mathbf{S}}_2$, enabling only triplet scattering (for a derivation and detailed description of these these spin projectors see Appendix B.1). In the classically allowed range of the Rydberg electron $k = \sqrt{-1/(n_{\text{eff},1}\, n_{\text{eff},2}) + 2/r}$ (in atomic units), and $k = 0$ elsewhere. There, $n_{\text{eff},1}$ and $n_{\text{eff},2}$ are the effective quantum numbers of the Rydberg states coupled by the scattering term. In the calculation we include configuration mixing [88] with neighboring Rydberg manifolds. For this we choose a basis that includes levels that are within $\pm 4.9 n_{\text{eff}}$ quantum numbers from the target level. Since only states with $m_{\ell 1} = 0$ are non-vanishing on the internuclear axis in the S-wave limit, the relevant Hilbert space is restricted to $\{|n, \ell_1, j_1, m_{j1} = \pm 1/2, m_{s2} = \pm 1/2, m_{i2} = \pm 1/2, \pm 3/2\rangle\}$. The Hamiltonian in Eq. 4.1 conserves $m_k := m_{j1} + m_{s2} + m_{i2}$ and the space breaks up into separated sub-spaces with $m_k = \pm 5/2, \pm 3/2, \pm 1/2$, where the scattering term couples states with the same $m_{j1} + m_{s2}$, while the hyperfine term couples states with the same $m_{s2} + m_{i2}$.

The Hamiltonian in Eq. 4.1 is diagonalized, resulting in adiabatic potential surfaces $V_{ad,i}(Z)$ and associated adiabatic states $\Psi_{ad,i}(Z)$. Here i is an arbitrary label assigned to a potential $V_{ad}(Z)$. The permanent electric dipole moment associated with the adiabatic states are also obtained using $d_i(Z) = \langle \Psi_{ad,i}(Z)|Z|\Psi_{ad,i}(Z)\rangle$. The molecular vibrational states $W_{i,\nu}$ and their wave functions $\Psi_{i,\nu}(Z)$ are obtained by solving Schrödinger's equation with the potential $V_{ad,i}(Z)$ and a reduced mass of 87 amu/2. The electric dipole moment of each vibrational state is obtained by integrating over the dipole moment of the adiabatic state weighted by the local molecular state probability density as $d_{i,\nu} = \int |\Psi_{i,\nu}(Z)|^2 d_i(Z) dZ$. The magnetic moments $\mu_i(Z)$ of the molecular states are obtained analogously using $\mu_{i,\nu} = \int |\Psi_{i,\nu}(Z)|^2 \mu_i(Z) dZ$.

Figures 4.5a and b show all calculated potentials $V_{ad}(Z)$ associated with the $35D_{5/2}$ and $35D_{3/2}$ Rydberg states that connect to the $F = 2$ hyperfine level of the $5S_{1/2}$ atom. The vibrational ground and first-excited states ($\nu = 0, 1$) of the deep potentials for both fine structure components are also plotted. The deep potentials arise from pure triplet scattering

channels while the shallow potentials are due to hyperfine-induced spin-mixing between the electronic singlet and a triplet state. The deep and shallow potentials and their states have degeneracies of 6 and 4, respectively. In Fig. 4.5c and d the calculated vibrational energies W_ν for $\nu = 0, 1$ are plotted over a range of n for both the $nD_{5/2} + 5S_{1/2}$ and $nD_{3/2} + 5S_{1/2}$ molecules.

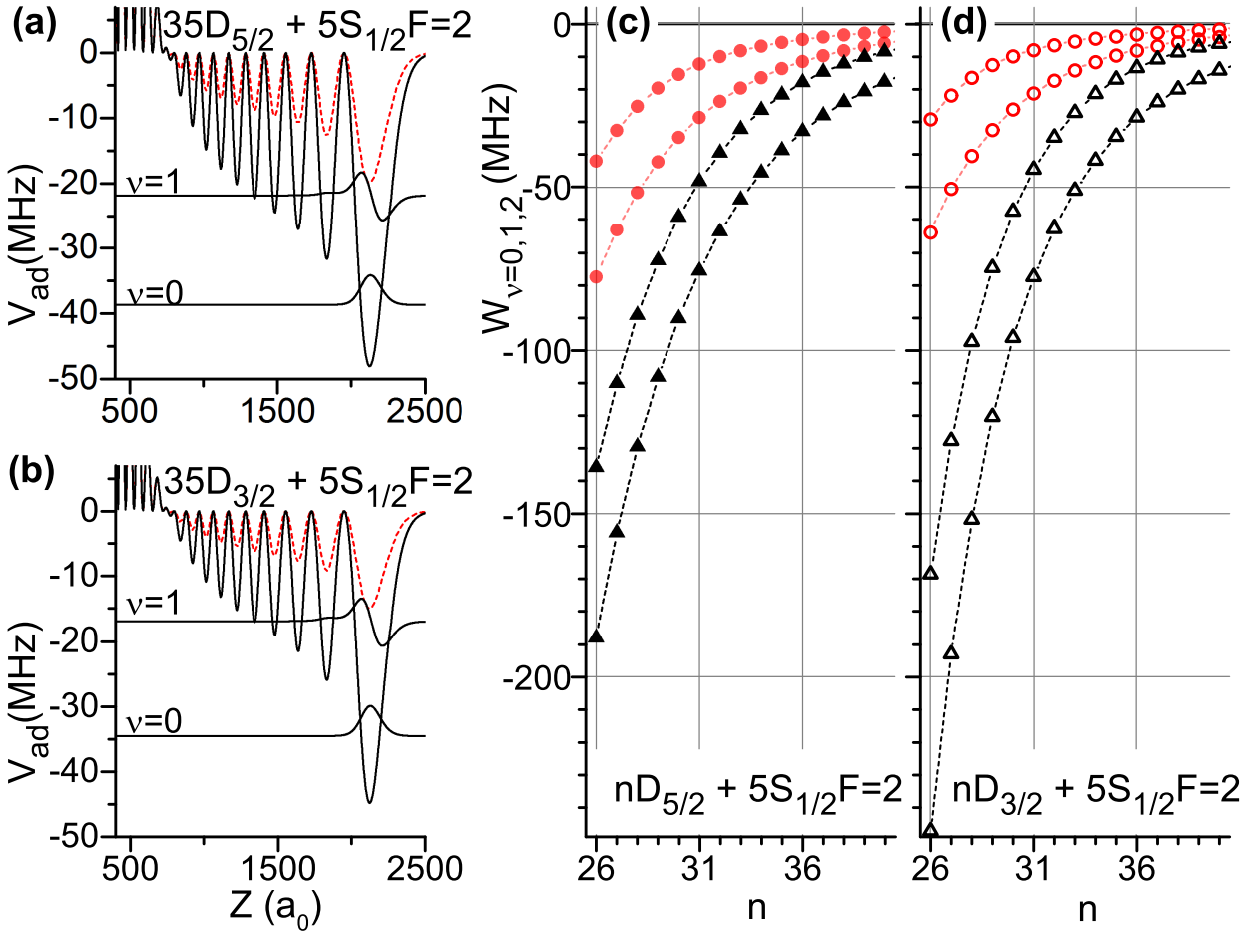

Figure 4.5: (a) and (b): Deep (solid) and shallow (dashed) potentials for $35D_{3/2}$ and $35D_{5/2}$-type molecules, for $A_{s0} = -14\ a_0$, and vibrational wave functions for $\nu = 0, 1$ in the deep potentials. (c) and (d): Energy levels for $\nu = 0, 1$ in the deep (triangles) and shallow (circles) potentials vs n.

In the experiment we excite molecules below the $F = 2$ dissociation limit, for which the states in the deep potential $V_{ad}(Z)$ have the larger degeneracy and are easier to observe due to their larger binding energies. In the model, the Rydberg wave functions are defined by quantum defects [56] and the polarizability of the perturbing Rb $5S_{1/2}$ atom α, leaving the

zero-energy S-wave scattering length A_{s0} as the only free parameter. Hence, we adjust A_{s0} so that the energies of the $\nu = 0$ levels in the deep $V_{ad}(Z)$ match the experimental data in Fig. 4.3 and obtain a value of $A_{s0} = (-14 \pm 0.5)\ a_0$. The calculated binding energies are plotted in gray in Fig. 4.4a with the experimentally measured binding energies. The uncertainty in the value of A_{s0} is obtained from the fit and is set by the uncertainty in the experimentally measured binding energies. (For $37D_{5/2}$ the $\nu = 0$ binding energy increases by about 4 MHz when changing A_{s0} from -13.5 to $-14.5\ a_0$.) This value of A_{s0} lies within the range of published values -13 to -19.48 a_0 [16, 17, 18, 20, 29].

4.4 Transition between Hund's cases (a) and (c)

As a result of their relatively weak bonds and large internuclear separations, long-range diatomic Rydberg molecules exhibit properties that are largely dictated by the properties of their constituent atoms. It follows that the angular-momentum coupling configurations and Hund's cases in Rydberg molecules are linked directly to the angular-momentum couplings of the individual Rydberg and ground-state atoms. For the D-type Rydberg molecules considered here, the fine-structure of the Rydberg atom is comparable to the scattering-induced binding interaction between the Rydberg electron and ground-state atom. This results in the $nD_j + 5S_{1/2}$ molecular states exhibiting a transition between Hund's case (a) at low n where the scattering-induced binding interaction exceeds the Rydberg atom fine structure coupling, and Hund's case (c) at high n where the fine structure dominates the scattering interaction.

The effects of the Rydberg atom fine-structure on the molecular binding in Hund's case (c) for low-ℓ long-range Rydberg molecules can be understood using the Fermi-type model in Eq. 4.1 considering the triplet S-wave scattering interaction term evaluated in the fine structure basis of the Rydberg atom. For a Rydberg electron in a state $|n, \ell, j, m_j\rangle$, the part

of the scattering interaction that depends on the Rydberg levels is given by

$$2\pi A_s(k)\langle n', \ell', j', m_j'|n, \ell, j, m_j\rangle, \tag{4.2}$$

where the unprimed and primed state vectors represent the initial and final Rydberg states evaluated at the location of the perturbing atom, respectively. Following the rules for addition of angular momenta (A.5), the coupled $|n, \ell, j, m_j\rangle$ states can be expressed as linear combinations of the uncoupled $|n, \ell, m_\ell, m_s\rangle$ basis states, where for the two fine-structure components $j = \ell + 1/2$ and $j = \ell - 1/2$ of the Rydberg atom we have (see pages 212-214 in [75])

$$\left.\begin{aligned} |n,\ell,j,\tfrac{1}{2}\rangle &= \sqrt{\frac{\ell+1}{2\ell+1}}|n\ \ell\ 0\ \uparrow\rangle + \sqrt{\frac{\ell}{2\ell+1}}|n\ \ell\ 1\ \downarrow\rangle \\ |n,\ell,j,-\tfrac{1}{2}\rangle &= \sqrt{\frac{\ell+1}{2\ell+1}}|n\ \ell\ 0\ \downarrow\rangle + \sqrt{\frac{\ell}{2\ell+1}}|n\ \ell\ -1\ \uparrow\rangle \end{aligned}\right\} \quad j = \ell + \frac{1}{2} \tag{4.3}$$

$$\left.\begin{aligned} |n,\ell,j,\tfrac{1}{2}\rangle &= -\sqrt{\frac{\ell}{2\ell+1}}|n\ \ell\ 0\ \uparrow\rangle + \sqrt{\frac{\ell+1}{2\ell+1}}|n\ \ell\ 1\ \downarrow\rangle \\ |n,\ell,j,-\tfrac{1}{2}\rangle &= \sqrt{\frac{\ell}{2\ell+1}}|n\ \ell\ 0\ \downarrow\rangle - \sqrt{\frac{\ell+1}{2\ell+1}}|n\ \ell\ -1\ \uparrow\rangle \end{aligned}\right\} \quad j = \ell - \frac{1}{2} \tag{4.4}$$

In the S-wave limit, only $m_\ell = 0$ components of the Rydberg wave function are non-zero in their projection onto the internuclear axis, and only the first terms in Equations 4.3 and 4.4 (highlighted boxes) couple via the S-wave scattering interaction. The interaction strength in this case is fine-structure dependent with factors of $\ell/(2\ell + 1)$ for $j = \ell - 1/2$ and $(\ell + 1)/(2\ell + 1)$ for $j = \ell + 1/2$. As a result, the depth ratio of the adiabatic molecular potentials for the $j = \ell - 1/2$ and $j = \ell + 1/2$ components is $\ell/(\ell+1)$. For Rydberg molecules formed by a D-state Rydberg atom, $\ell = 2$ and the depth ratio of the adiabatic molecular potentials for the two $j = 3/2$ and $j = 5/2$ components is 2/3.

From this it follows that in Hund's case (c) (high n) the $\nu = 0$ binding-energy ratio for $nD_j + 5S_{1/2}$ $j = 3/2$ and 5/2 molecules should also be about 2/3. This is seen in Fig. 4.6a

which shows the calculated $W_{\nu=0}$ binding energies for both of the fine structure molecules (from Figs. 4.5c and d) over a range of n, with the Rydberg D-state fine-structure coupling also plotted for reference. In the high-n limit in Fig. 4.6a the $\nu = 0$ binding-energy ratio for $D_{3/2}$ and $D_{5/2}$ approaches 2/3, as expected for Hund's case (c), and both sets of binding energies approximately scale inversely with the atomic volume (i.e., as $n_{\rm eff}^{-6}$)). At low n, the system transitions into Hund's case (a) where the scattering interaction becomes larger than the fine structure coupling and the binding-energy ratio changes from 2/3 to $\gg 1$. The $\nu = 0$ binding energies for the lower $D_{3/2}$ fine structure level in this limit exceed the fine structure coupling and keep scaling as $n_{\rm eff}^{-6}$, while those for the $D_{5/2}$ level approach the fine structure splitting and its scaling ($n_{\rm eff}^{-3}$).

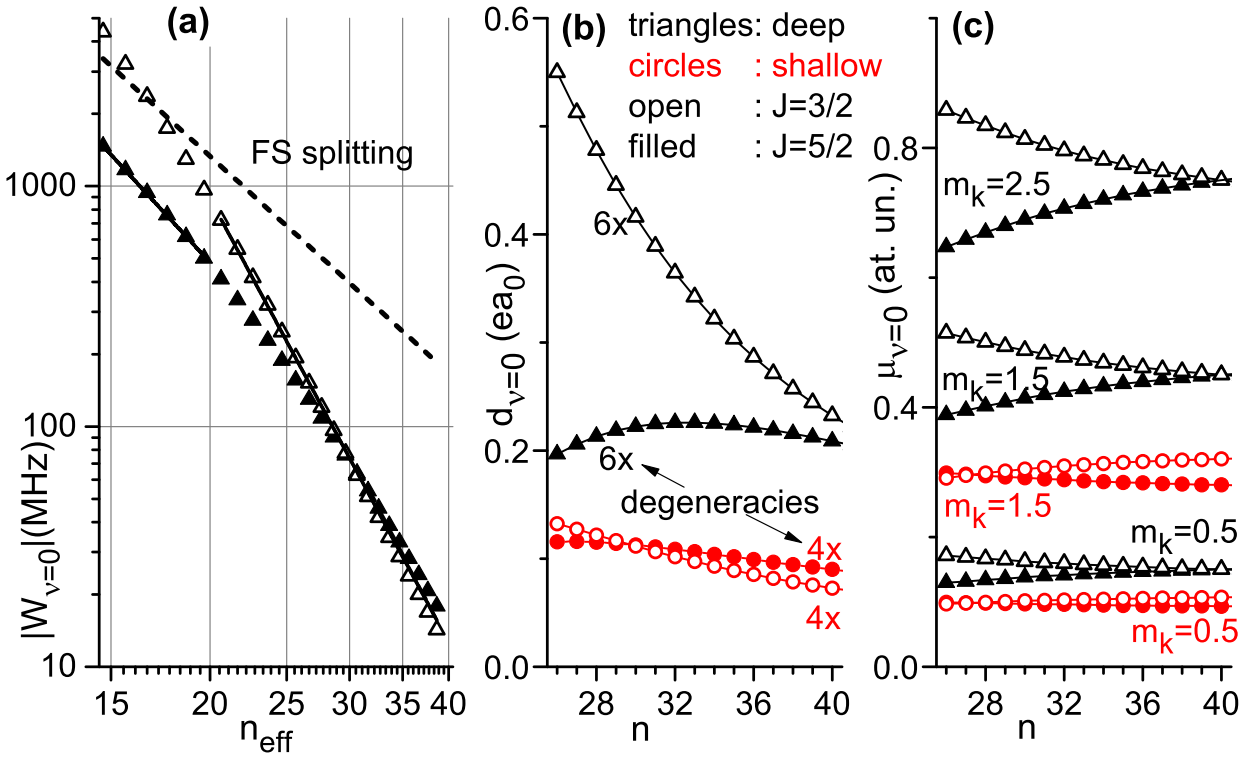

Figure 4.6: (a) $\nu = 0$ binding energies in the deep molecular potentials for $nD_{5/2}$ (filled triangles), $nD_{3/2}$ (open triangles), and the D fine structure splitting (dashed line), vs effective quantum number. Solid lines are fits. The $D_{3/2}$ energies are fit well by 84.2 GHz/$n_{\rm eff}^{6.13}$. The $D_{5/2}$ energies do not exhibit a global scaling; at low n they tend to scale as 23 MHz/$n_{\rm eff}^{3.6}$. (b) Electric dipole moments for $\nu = 0$ vs n for the deep (triangles) and shallow (circles) $V_{\rm ad}(Z)$ for $j = 3/2$ (open) and $j = 5/2$ (filled). (c) Magnetic dipole moments for the same states as in (b).

Given these trends, the $\nu = 0$ binding energy ratio for the $j = 3/2$ and $j = 5/2$ molecules is a convenient experimental measure to characterize the system. Figure 4.7 shows spectra of the two fine structure components of $37D$. Molecular peaks are present for both $j = 3/2$ and 5/2, with respective binding energies of 24 ± 3 MHz and 26 ± 3 MHz, corresponding to a ratio of 0.92 ± 0.15. Since this is significantly larger than 2/3, for $n = 37$ the system is in the transition regime between Hund's case (a) and (c).

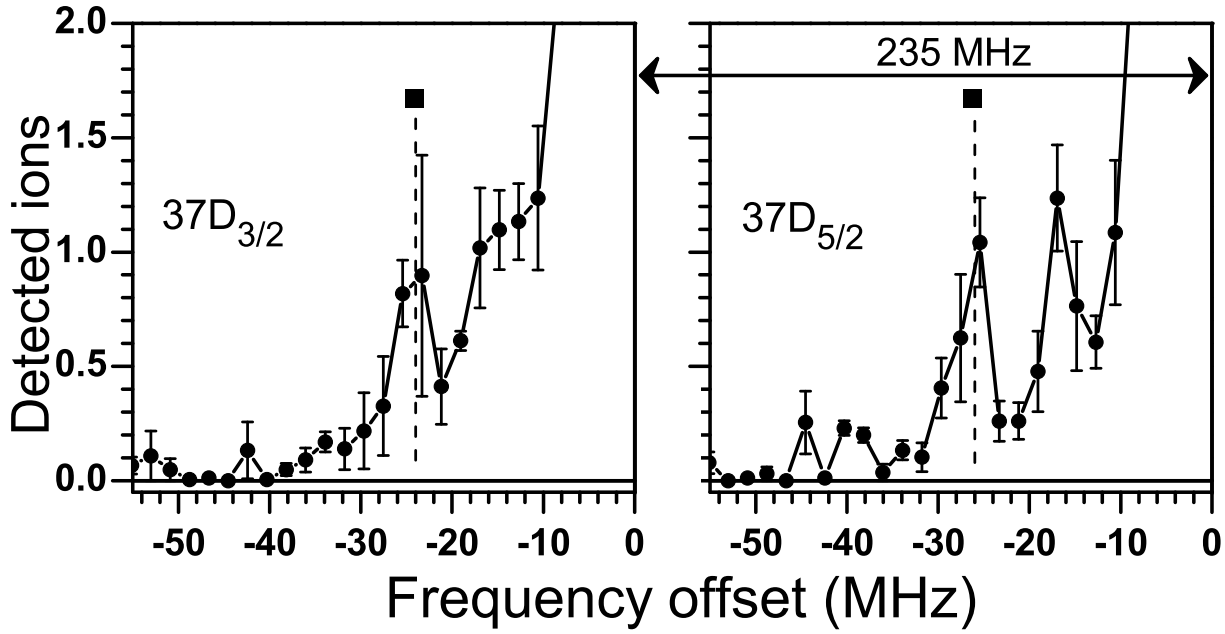

Figure 4.7: Experimental spectra centered on the $37D_j$ atomic Rydberg lines for $j = 3/2$ (left) and $j = 5/2$ (right; same as in Fig. 4.3). $^{87}\mathrm{Rb}(37D_j + 5S_{1/2})(\nu = 0)$ molecular signals are indicted by vertical dashed lines and squares.

4.5 Molecular line broadening

The lifetimes of long-range Rydberg molecules is generally an interesting topic due to the peculiar nature of the binding interaction. Because the molecular states arise via an electron-atom scattering interaction, the bound molecular states can be characterized as metastable scattering resonances with line widths determined by tunneling rates out of the local scattering potential. A calculation and discussion of the quasi-bound molecular states for D-type molecules and their tunneling-limited lifetimes is given in section 5.3 of Chapter V.

The calculated line widths range from μHz for the $\nu = 0$ vibrational states of interest here to ∼MHz for higher-lying states. In the molecular spectra shown in Figs. 4.3 and 4.7 several broadening mechanisms contribute to the observed line widths.

The resolution in photoassociation spectroscopy is itself limited by several factors including the transition line width, laser line widths and temperature of the atomic sample [21]. To achieve high resolution, the kinetic energy of the colliding atoms needs to be comparable to or less than the transition line width. The transition line width is dominated by the laser excitation bandwidth ≈ 2 MHz, which exceeds the Doppler broadened $5S \rightarrow 35D$ transition line width $\Delta\nu_{Doppler} = 319$ kHz FWHM. At T= 17μK, we have $k_B \times 17\mu\text{K}/h = 354$ kHz< 2 MHz, readily satisfying this condition and setting the resolution limit of the photoassociation spectroscopy equal to the laser bandwidth.

Residual fields in the experiment also contribute to the observed line widths. Figure 4.6b and c show calculated electric and magnetic dipole moments for D-type molecules. These are discussed in more detail in section 5.5 of Chapter V. Noting that $d_{\nu=0} \lesssim 0.25\, ea_0$ and that the stray electric field in the experiment is $\lesssim 200$ mV/cm, the experimental permanent-electric-dipole shift is well below 1 MHz and therefore not expected to contribute significantly. Similarly, the Stark shifts of the atomic lines are small. The atomic and molecular lines experience more substantial energy shifts due to the local $\lesssim 1$ Gauss magnetic trapping field. In this field, the maximum Zeeman shifts of the atomic m_j states are $\lesssim 8$ MHz, which is much less than the measured molecular binding energy. The individual atomic m_j states are not distinguishable in the spectra, contributing only to the observed broadening of the atomic lines.[1] The calculated magnetic moments of the molecules are given in Fig. 4.6c. In the magnetic field of the atom trap, the molecular lines are expected to be broadened over a range $\lesssim 4$ MHz, compared to the $\lesssim 8$ MHz of the atomic lines. These estimates agree well with the line widths observed in the experimental spectra.

[1]The Zeeman shift is given by $\Delta E_B = \mu_B g m_j B$, where μ_B=1.4 MHz/Gauss, the g factors are $(m_j = 1/2, 3/2, 5/2) = (-2, 1.33, 1.2)$ for the D states, and B=1 Gauss. The shift is -1.4 MHz for $m_j = +1/2$, 2.8 MHz for $m_j = +3/2$, and 4.2 MHz for $m_j = +5/2$. The largest shift is that of the $m_j = +5/2$ level and the maximum field-induced broadening $= 2 \times 4.2\ MHz \approx 8\ MHz$.

Since the PA experiments are necessarily performed in relatively high density ground-state atom samples, broadening due to the polarization interaction between the Rydberg electron and nearby ground-state atoms is also considered. This can be estimated for a given density n of the ground-state atom sample from [10]

$$\Delta_{pol} = 17.5 \frac{\alpha e^2}{2(4\pi\epsilon_0)^2} n^{4/3}. \tag{4.5}$$

For the ground-state atom density used in the experiment this amounts to a $\Delta_{pol} \lesssim 60$ Hz, which is negligible compared to the laser line widths and field-induced shifts discussed above.[2]

4.6 Summary

In this Chapter I described an experimental study of ^{87}Rb(nD_j+$5S_{1/2}$) Rydberg molecules. The binding energies of the molecular states were found to be larger than those of previously observed ^{87}Rb($nS_{1/2} + 5S_{1/2}$) molecules, in agreement with the expected $\sqrt{2\ell+1}$-scaling of the angular wave functions $Y_l^{m=0}(\theta = 0)$. The transition of rubidium D-type molecules between Hund's case (a) at low n, where the scattering-induced binding interaction exceeds the Rydberg-atom fine structure, to Hund's case (c) at high n where the fine structure dominates was investigated and probed experimentally. Molecular and atomic line broadenings were discussed, and the observed line broadenings found to be consistent with laser line widths and Zeeman shifts due to the magnetic trapping field.

The work presented here motivates a number of studies on long-range D-type Rydberg molecules. With improved spectroscopic resolution the electric and magnetic dipole moments of the D-type molecular states could be measured, as well as their higher-lying vibrational levels in the deep potentials in Fig. 4.5 and in the shallow potentials. The transition behavior of the molecular dipole moments and between Hund's cases (a) and (c) could also

[2]The pre-factor in Eq. 4.5 reflects the statistical distribution of ground-state atoms surrounding the Rydberg electron. The value of 17.5 is the most probable value of $\sum_i r_i^{-4}$ calculated by G.C. Wick [89], where r_i is the distance of atom i from the Rydberg electron [10].

be directly probed. As is discussed in more detail in Chapter V, inclusion of the P-wave scattering interaction strongly modifies the adiabatic potentials at smaller interatomic separations. This results in additional bound vibrational states as well as unexpectedly long-lived resonances near the dissociation threshold, which should also be observable in experiments. The lifetimes and decay processes of these molecular states could be investigated in future work.

CHAPTER V

Angular-momentum couplings in long-range Rydberg molecules

In addition to the electron-atom scattering interaction, the molecular potentials and properties of long-range Rydberg molecules are dependent on the Rydberg-atom wave function as well as the angular-momentum couplings of the Rydberg- and ground-state constituents. Rydberg molecules can exhibit a broad range of different angular momentum coupling schemes. For low-ℓ Rydberg molecules ($\ell \lesssim 2$ in rubidium), the angular-momentum coupling configurations span three Hund's cases [(a), (b), and (c)], dictated by the relative strength of the Rydberg atom's fine structure coupling compared to that of the $e^- + 5S_{1/2}$ scattering interaction. The Rb($nD_j + 5S_{1/2}$) molecules are unique among the low-ℓ molecules because their Rydberg fine-structure couplings are comparable to the scattering interaction strength, and they fall anywhere between two Hund's cases (a) and (c) by a mere change in principal quantum number n. For high-ℓ Rydberg molecules, the molecular binding interaction is stronger than the fine structure coupling, and is comparable to the hyperfine coupling of the ground-state perturber. In this work we predict the existence of new spin-mixed potentials and molecular states that arise from the hyperfine structure coupling of the ground-state atom. Inclusion of the $5S_{1/2}$ hyperfine coupling in the Fermi model generates additional adiabatic potentials of mixed triplet and singlet character for both high- and low-ℓ molecules, that are deep enough to sustain bound states.

In this chapter I present a theoretical study of the influence of angular-momentum couplings on the properties of long-range Rydberg molecules. I first describe a Fermi model for Rydberg molecules with all the relevant interactions and angular-momentum couplings including S-wave and P-wave singlet and triplet scattering of the Rydberg electron with the $5S_{1/2}$ atom, along with the fine structure coupling of the Rydberg atom and hyperfine structure coupling of the $5S_{1/2}$ atom. By selectively enabling the different interactions in the model, the effects of each of the individual interactions on the adiabatic molecular potentials are revealed. Typical vibrational-state wave functions, molecular binding energies, lifetimes, and dipole moments are calculated and discussed with an emphasis on the role of angular-momentum couplings. In the final section I describe the effects of the ground-state atom hyperfine coupling on the relatively deeply bound trilobite Rydberg molecules formed by a Rydberg atom in a degenerate high-ℓ state.

5.1 The complete Fermi model

The Fermi model [10, 12] used here to describe diatomic Rydberg molecules takes into account the angular-momentum couplings in the Rydberg atom and perturbing ground-state atom system whose strengths are comparable to the Rydberg e^-+perturber interaction. A schematic of the relevant couplings is shown in Fig. 5.1a. The perturbing ^{87}Rb $5S_{1/2}$ atom is located at a position Z from the ionic core of the Rydberg atom, which is fixed at the origin. The internuclear axis is along $\hat{\mathbf{z}}$. The orbital and spin angular momenta of the Rydberg atom are denoted by L_1 and S_1, respectively. For $L_1 \leq 2$ and within the n-range of interest, the Rydberg-atom fine structure is of the same order as the $e^- + 5S_{1/2}$ scattering interaction and is therefore included. The hyperfine coupling of the electron spin S_2 and nuclear spin I_2 of the perturbing $5S_{1/2}$ ground-state atom is also included, because it is several GHz and is, in most cases, stronger than the Rydberg electron's fine structure coupling and the $e^- + 5S_{1/2}$ scattering interaction. The orbital angular momentum of the $5S_{1/2}$ atom is $L_2 = 0$. The Rydberg atom's hyperfine structure decreases as n^{-3}; for the lowest S-states relevant to our

work it does not exceed several MHz [90, 91], and it is much lower for higher-ℓ states [92]. The Rydberg atom's hyperfine structure is therefore not included.

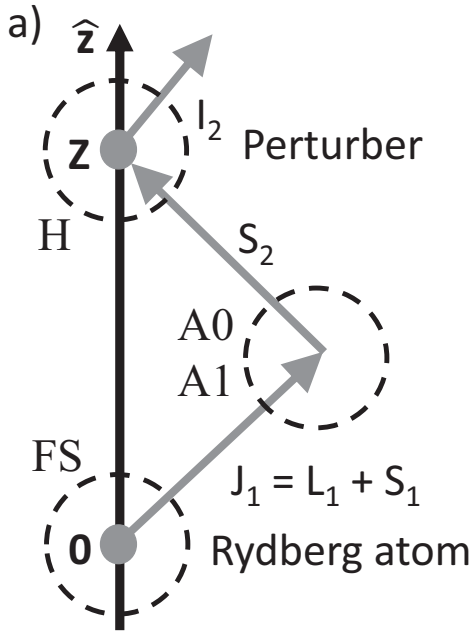

b)

	$m_k = +1/2$			*diagonal*		
	m_{j1}	m_{s2}	m_{i2}	A0	A1	H
	+3/2	+1/2	-3/2		X	X
H						
	+3/2	-1/2	-1/2		X	X
A1						
	+1/2	+1/2	-1/2	X	X	X
H						
	+1/2	-1/2	+1/2	X	X	X
A0						
	-1/2	+1/2	+1/2	X	X	X
H						
	-1/2	-1/2	+3/2	X	X	X
A1						
	-3/2	+1/2	+3/2		X	X

Figure 5.1: a) Angular momentum coupling scheme for diatomic ^{87}Rb($nD_j + 5S_{1/2}, F$) Rydberg molecules. The relevant interactions are circled. Here, A0 and A1 denote $e^- + 5S_{1/2}$ scattering interactions involving the $m_{l1} = 0$ (S-wave and P-wave) and the $|m_{l1}| = 1$ (P-wave only) components of the Rydberg electron's state, respectively, and H denotes the hyperfine interaction of the $5S_{1/2}$ atom. FS denotes the fine structure coupling. b) States in the $m_k = m_{j1} + m_{s2} + m_{i2} = +1/2$ subspace and their relevant interactions. In the left column, horizontal gray bars are placed between (m_{j1} m_{s2}) or (m_{s2} m_{i2}) for states in neighboring rows that are coupled by either the scattering or the hyperfine interaction. The Xs in the right column indicate the interactions that have diagonal terms in (m_{j1} m_{s2} m_{i2}).

For a Rydberg atom with its ionic core at the origin and the Rydberg electron located at $\mathbf{r}$, and with a $5S_{1/2}$ atom located at $\mathbf{R} = Z\hat{\mathbf{z}}$, the Hamiltonian is written as

$$\begin{aligned}\hat{H}(\mathbf{r}, Z) = \hat{H}_0 &+ \sum_{i=S,T} 2\pi A_s^i(k)\delta^3(\mathbf{r} - Z\hat{\mathbf{z}})\hat{\mathbb{I}}_i \\ &+ \sum_{i=S,T} 6\pi A_p^i(k)\delta^3(\mathbf{r} - Z\hat{\mathbf{z}})\overleftarrow{\nabla} \cdot \overrightarrow{\nabla}\ \hat{\mathbb{I}}_i \\ &+ A\hat{\mathbf{S}}_2 \cdot \hat{\mathbf{I}}_2\end{aligned} \tag{5.1}$$

In the unperturbed Rydberg Hamiltonian $\hat{H}_0$ we use published quantum defects [56], which account for core penetration and fine structure. For $\ell \geq 5$ we use the fine structure correction of hydrogen as well as a small quantum defect to account for core polarization, $\delta_\ell = 0.75\alpha_D/\ell^5$ [56], with a dipolar polarizability for Rb^+ of $\alpha_D = 9.023$ atomic units [62]. The energy-dependent S-wave ($l = 0$) and P-wave ($l = 1$) scattering lengths (A_s and A_p, respectively) have the general form $A_l(k) = -\tan\delta_l/k^{2l+1}$, where δ_l is the l- and energy-dependent scattering phase shift. For our calculations the non-relativistic scattering phase shifts $\delta_{l=0}$ and $\delta_{l=1}$ were provided by I. I. Fabrikant based on [1] (see Fig. 2.2 in Chapter II). The electron momentum is given by $k = \sqrt{-1/n_0^{*2} + 2/r}$ (atomic units) in the classically allowed range of the Rydberg electron and $k = 0$ elsewhere. Here, n_0^* is the effective Rydberg quantum number of the level of interest. To account for configuration interactions, we employ basis sets $\{|n, L_1, J_1, m_{j1}\rangle \otimes |m_{s2}, m_{i2}\rangle\}$ that include all Rydberg levels with effective quantum numbers $|n^* - n_0^*| \lesssim 2.5$. For the Rydberg atom, all L_1, J_1 and m_{j1} are included (as in [88]), and for the perturber atom all m_{s2} and m_{i2} are included. The singlet (S) and triplet (T) channels of the $e^- + 5S_{1/2}$ scattering interaction include projectors $\hat{\mathbb{I}}_{(S,T)}$, defined as $\hat{\mathbb{I}}_T = \hat{\mathbf{S}}_1 \cdot \hat{\mathbf{S}}_2 + \frac{3}{4}$, which has an eigenvalue of one (zero) for the triplet (singlet) states, and $\hat{\mathbb{I}}_S = \hat{\mathbb{I}} - \hat{\mathbb{I}}_T$. The operators $\hat{\mathbf{S}}_1$ and $\hat{\mathbf{S}}_2$ are the spins of the Rydberg electron and $5S_{1/2}$ atom, respectively, and $\hat{\mathbb{I}}$ is the identity operator. The last term in Eq. 5.1 accounts for the hyperfine interaction of the perturber. The $^{87}Rb(5S_{1/2})$ perturber atom has nuclear spin $\hat{\mathbf{I}}_2$ with $I_2 = 3/2$, and hyperfine levels $F_< = 1$ and $F_> = 2$, with a hyperfine coupling parameter $A = h \times 3.4$ GHz.

Only levels with $m_{\ell 1} = 0, \pm 1$ components have non-vanishing wave functions or wave function gradients on the internuclear axis. The S-wave interactions couple Rydberg states with $m_{\ell 1} = 0$ components. The P-wave interactions couple states with $m_{\ell 1} = 0$ components through the radial derivative of the Rydberg wave function and states with $m_{\ell 1} = \pm 1$ components through the polar-angle derivative of the wave function. The electron scattering term in Eq. 5.1 conserves $m_{j1} + m_{s2}$, while the hyperfine term conserves $m_{s2} + m_{i2}$. The full

Hamiltonian conserves $m_k := m_{j1} + m_{s2} + m_{i2}$. Hence, the Hilbert space can be broken up into subspaces of fixed quantum number m_k. As an example, the subspace for $m_k = +1/2$ and its couplings via the S-wave, P-wave, and hyperfine interactions is shown in Fig. 5.1b. The gray bars in Fig. 5.1b illustrate that the couplings are organized in a block-diagonal structure in the magnetic quantum numbers. Since the couplings via the scattering terms require $|m_{j1}| \leq 3/2$, the $^{87}Rb_2$ Rydberg molecules have $|m_k| \leq 7/2$.

5.2 Adiabatic molecular potentials

Adiabatic molecular potentials $V_i(Z)$ (i is an arbitrary label) are obtained by diagonalizing the Hamiltonian in Eq. 5.1 for a grid of perturber atom positions, Z, through the extent of the Rydberg wave function. To highlight the effects of the different terms in Eq. 5.1 on $V_i(Z)$, in Figs. 5.2 and 5.3 we show adiabatic potentials calculated for D-type Rydberg molecules with the different interaction terms in Eq. 5.1 selectively turned on.

First, we consider adiabatic potentials without hyperfine coupling. Figure 5.2a shows adiabatic potentials for the $31D + 5S_{1/2}$ molecule with only the ^{3}S interaction turned on and no fine structure coupling. This results in three degenerate oscillatory potentials, one corresponding to each triplet state, and a flat potential corresponding to the singlet state (which has no ^{3}S interaction). The triplet potential curves are similar to those calculated in [4], in which the S-wave scattering length $-\tan\delta_s/k$ is taken to first order in the electron momentum [12]. With an appropriate choice of the zero-energy S-wave scattering length, the ^{3}S interaction reproduces measured binding energies of vibrational ground states of S-type Rydberg molecules [20]. Similarly, the ^{3}S interaction with the addition of the fine structure reproduces vibrational ground states of D-type Rydberg molecules [25]. The effect of the fine structure coupling on the molecules is discussed further below.

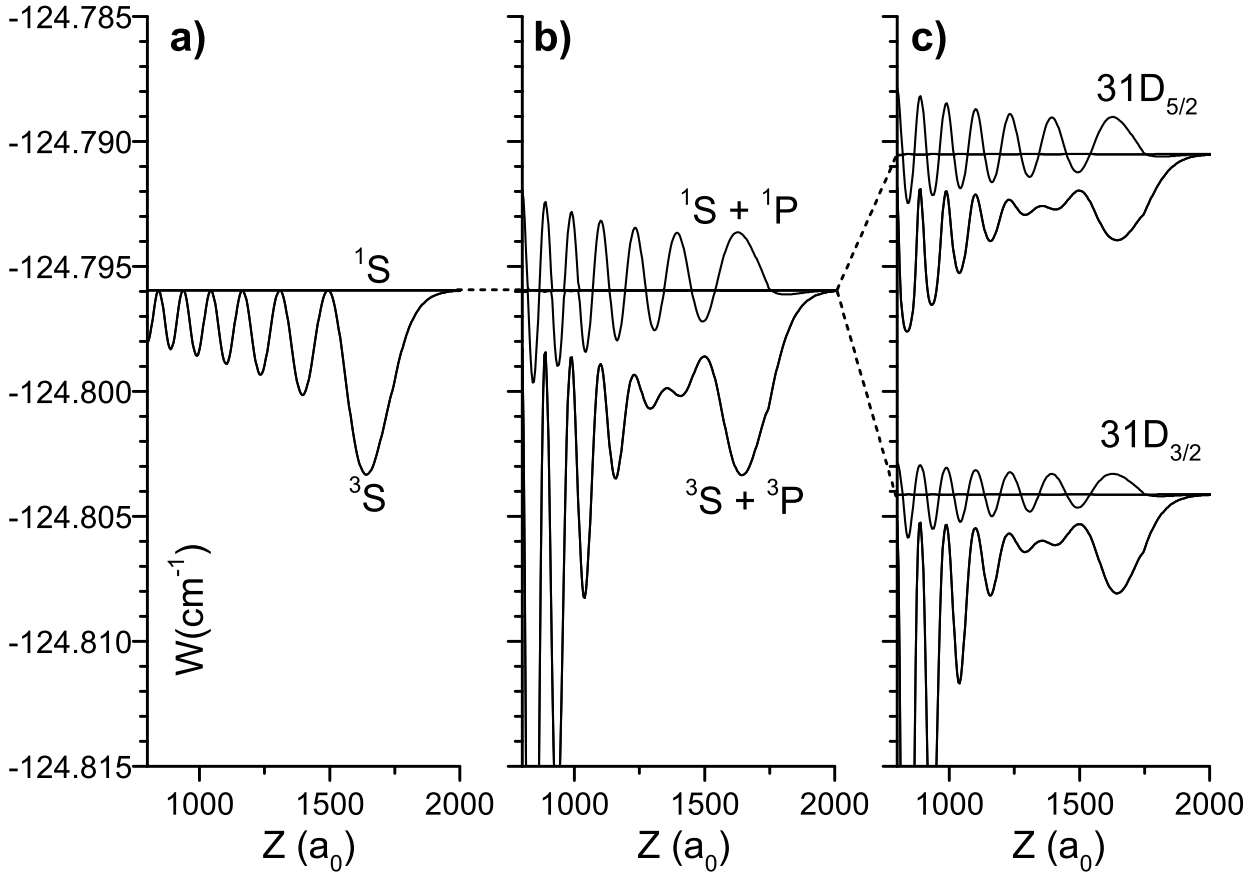

Figure 5.2: Adiabatic potentials for the $31D + 5S_{1/2}$ molecule with the following interaction terms in Eq. 5.1 selectively turned on (without the hyperfine interaction): a) ^{3}S scattering, b) ^{3}S, ^{1}S, ^{3}P, and ^{1}P scattering, and c) ^{3}S, ^{1}S, ^{3}P, and ^{1}P scattering with fine structure coupling.

Figure 5.2b shows adiabatic potentials resulting from the ^{3}S, ^{1}S, ^{3}P, and ^{1}P scattering interactions turned on and no fine structure coupling. At smaller internuclear separations, the influence of P-wave scattering becomes more significant due to higher electron energies closer to the Rydberg atom's ionic core (and therewith larger wave function gradients). The effect of the ^{3}P scattering interaction is evident in Fig. 5.2b, where the inner wells become notably deeper, while the outermost well remains relatively unaffected. The increasing contribution of P-wave scattering at smaller Z generates deep molecular potentials. The repulsive ^{1}S and attractive ^{1}P scattering interactions turn the flat singlet potential in Fig. 5.2a into an oscillatory singlet potential with maxima above and wells below the dissociation threshold,

as seen in Fig. 5.2b.

Figure 5.2c shows adiabatic potentials resulting from the the addition of the fine structure coupling of the Rydberg atom to the ^{3}S, ^{1}S, ^{3}P, and ^{1}P scattering interactions. The top and bottom plots show $31D_j + 5S_{1/2}$ potentials for the $j = 5/2$ and $3/2$ fine structure states, respectively. Qualitatively, the fine-structure coupling splits the molecular bonding strength (adiabatic-potential depth) of the fine-structure-free case between the two fine-structure levels, resulting in less deep potentials. The splitting ratio depends on which Hund's case is more relevant (see Sec. 5.4).

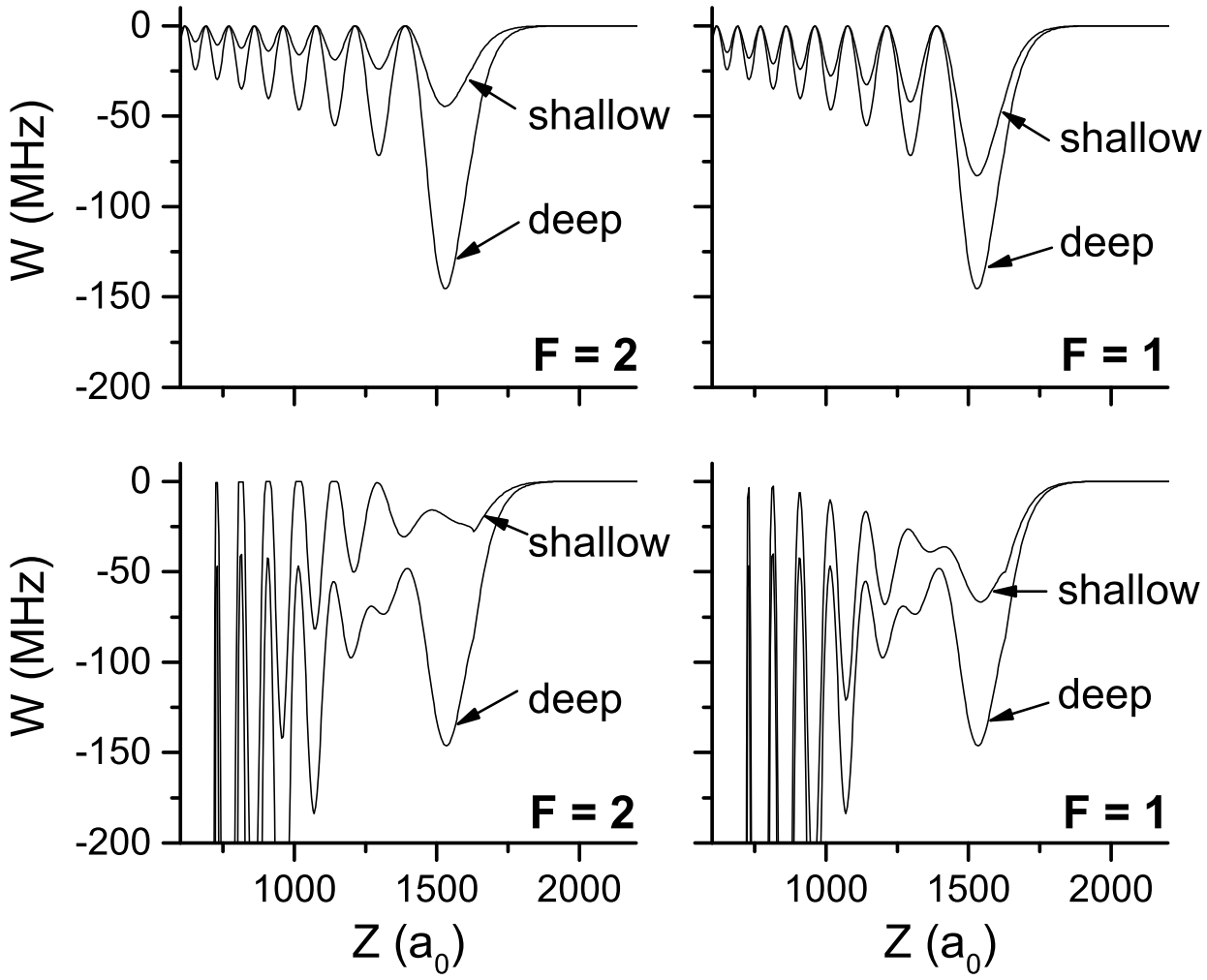

Figure 5.3: Binding adiabatic potentials for the ^{87}Rb($30D_{3/2} + 5S_{1/2}, F = 1, 2$) molecules with fine and hyperfine structure included, with ^{3}S scattering only (top row) and with ^{3}S, ^{1}S, ^{3}P, and ^{1}P scattering (bottom row). The hyperfine coupling leads to the shallow adiabatic potentials. The shallow potentials are different for the $F = 1$ and $F = 2$ hyperfine levels. The deep potentials do not depend on the hyperfine structure.

The hyperfine interaction of the ground-state perturber in Eq. 5.1 mixes the singlet and some triplet scattering channels, resulting in the replacement of the pure singlet potentials in Fig. 5.2 with shallow adiabatic potentials of mixed singlet-triplet character. As an example, in Fig 5.3 we show the adiabatic potentials for the $30D_{3/2}$+$5S_{1/2}, F = 1, 2$ molecules including the hyperfine interaction. The deep adiabatic potentials are of pure triplet character and are unaffected by the hyperfine interaction of the $5S_{1/2}$ atom. The $F = 1$ shallow, mixed singlet-triplet potentials are always deeper than the $F = 2$ shallow potentials. The shallow

potentials can typically sustain a few bound states that should be observable in experiments.

5.3 Quasi-bound molecular states and lifetimes

Due to the lack of an inner potential barrier, the molecular vibrational states have the character of metastable scattering resonances in potentials that are unbound on the inside. Figure 5.4 shows the (deep) adiabatic potential for the ^{87}Rb$(31D_{3/2}+5S_{1/2}, F=2)$ molecule and its quasi-bound states. These are qualitatively similar to those of S-type molecules [29]. The molecular wave functions consist of low-amplitude standing waves formed by outgoing and reflected ingoing waves in the region $Z \lesssim 1000\ a_0$, and a high-amplitude, resonantly enhanced portion in the outer adiabatic-potential wells at $Z \sim 1500\ a_0$. The latter are identified with quasi-bound molecular vibrational states that are metastable against tunneling-induced decay (decay into the region $Z \lesssim 1000\ a_0$).

The resonances are found by computing the wave function phase at a fixed location in the unbound region (we use $Z = 300\ a_0$) as a function of energy W. The phase and its derivative are plotted as a function of energy in the right and middle panels of Fig. 5.4, respectively. The quasi-bound molecular states occur at energies at which the phase undergoes sudden changes of $\Delta\Phi = \pi$. The quasi-bound molecular states are centered at energies at which the derivative of the phase is maximal (circles in the middle panel of Fig. 5.4). The resonances obey a single-level Breit-Wigner formula with frequency linewidths of the quasi-bound molecular states given by $\Gamma_\nu = 2/(h \times d\Phi/dW)$ [75], corresponding to lifetimes of $\tau = (\hbar/2)d\Phi/dW$. The lifetimes scale as the Wigner tunneling time delay [93]. Resonances with larger slopes $d\Phi/dW$ in Fig. 5.4 correspond to longer-lived quasi-bound states. In addition to the sharp resonances there are three broad resonances, as indicated by hatched regions in the middle panel of Fig. 5.4. While the broad resonances are not likely to cause observable effects in molecular spectra, they add to the total phase change over an energy range. For instance, within the energy range displayed in Fig. 5.4 the broad resonances account for a phase change of 3π and the quasi-bound molecular states for a change of 11π, corresponding to a

total change of 14π. The distinction between broad and narrow resonances may, in practice, depend on experimental parameters such as excitation bandwidth and atom temperature (which affects Frank-Condon factors).

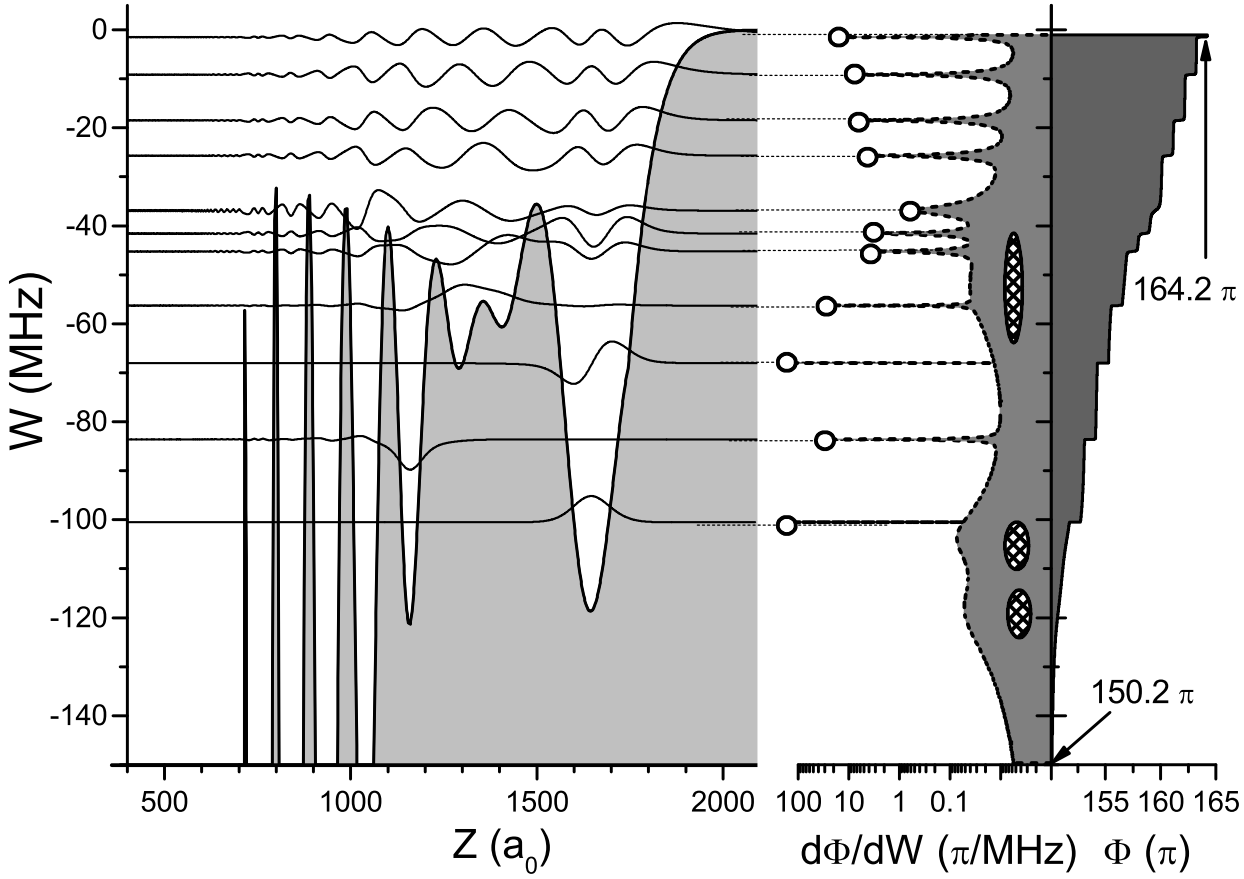

Figure 5.4: (Left) Adiabatic potential of the ^{87}Rb$(31D_{3/2} + 5S_{1/2}, F = 2)$ Rydberg molecule and vibrational wave functions. Each wave function corresponds to a narrow scattering resonance, characterized by a sudden change in the wave function phase by π in the unbound, inner region of the potential. (Right) Wave function phase at location $Z = 300\ a_0$. (Middle) The maxima of $d\Phi/dW$, indicated by circles, are used to determine resonance widths and lifetimes. Several broad resonances (hatched regions) are spread out over the displayed energy range.

Table 5.1: For the ^{87}Rb($31D_{3/2} + 5S_{1/2}, F = 2$) Rydberg molecule, we show the vibrational quantum number ν, binding energy, linewidth Γ_ν, decay time, and bond length.

ν	Energy (MHz)	Linewidth (MHz)	Decay time (μs)	<Z> (a_0)
0	-100.52	1.79E-11	8.89E9	1647.5
1	-83.59	2.18E-2	7.30	1160.0
2	-68.03	6.00E-8	2.65E6	1655.3
3	-56.27	2.37E-2	6.72	1324.0
4	-45.24	1.48E-1	1.08	1413.0
5	-41.58	1.87E-1	0.85	1527.9
6	-36.91	1.01E+0	0.16	1169.3
7	-26.58	1.28E-1	1.24	1428.4
8	-18.48	9.99E-2	1.59	1467.0
9	-9.14	7.78E-2	2.05	1481.8
10	-1.48	3.71E-2	4.29	1697.0

In Table 5.1 we give the binding energies, linewidths, decay times, and average internuclear separation of the scattering resonances shown in Fig. 5.4. Each quasi-bound state is assigned a vibrational quantum number ν, sequentially increasing from 0 for the most strongly bound state in the outermost well to 10 for the most weakly bound state. Generally, one expects bound states furthest from the dissociation threshold to have the longest lifetimes. Here, the ground and first excited states of the outermost potential well (labeled ν=0 and 2, respectively) are well-confined and have lifetimes in the range of hours and seconds, respectively. These lifetimes only reflect tunneling-induced decay. The actual lifetimes of these molecular states are, in fact, much shorter due to additional decay mechanisms, such as radiative decay of the Rydberg state and collisions with ground-state atoms [94]. An early

dissociation process via the energy exchange between the Rydberg electron and ground-state atom has also been used to explain shorter molecular lifetimes observed in experiments [95]. Nevertheless, the relatively long lifetimes and large Frank-Condon factors associated with these outermost states make them the easiest to isolate experimentally [20, 25, 30]. There are also several resonances in the inner potential wells (ν=1 and 3) with lifetimes on the order of that of the Rydberg atom (which for ^{87}Rb $31D_{3/2}$ is about 20 μs in a 300 K blackbody radiation field). The resonances at higher energies ($\nu = 4-6$) exhibit shorter lifetimes because of the smaller potential barrier through which they more readily tunnel inward. Surprisingly, above these short-lived resonances additional resonances with longer lifetimes appear ($\nu = 7-10$). Here, the inner oscillatory wells act like an aperiodic Bragg reflector of the molecular wave functions, resulting in unexpectedly long-lived resonances near the dissociation threshold. The lifetime of these states is largest when a Bragg reflection condition is met. This occurs in a range of Rydberg principal quantum numbers n at which the periodicity of the vibrational wave function approximately equals that of the Rydberg-electron wave function. This Bragg-reflection has previously been described as an internal quantum reflection process in S-type molecules [29].

5.4 Hund's cases for nD Rydberg molecules revisited

Low-ℓ diatomic Rydberg molecules ($\ell \lesssim 2$ in rubidium) exhibit a variety of Hund's coupling cases, determined by the relative strength of the Rydberg atom's fine structure coupling to the e^-+perturber scattering interaction. For ^{87}Rb(nD_j+$5S_{1/2}$) molecules the fine structure coupling is comparable to the scattering interaction strength. Due to this, D-type molecules trend from Hund's case (c) at large n, where the fine structure coupling exceeds the scattering interaction strength, to Hund's case (a) for $n \lesssim 35$, where the scattering interaction strength exceeds the fine structure coupling. In the previous chapter (IV), ^{87}Rb(nD_j + $5S_{1/2}, F = 2)(\nu = 0)$ molecules were observed in transition between the two Hund's coupling cases (a) and (c) [25]. In this section, the focus is on the molecular potentials and quasi-bound

states of the ^{87}Rb($nD_j + 5S_{1/2}$), $j = 3/2$ and $5/2$ molecules in the two limiting Hund's cases and in the transition regime. It should be noted that the Hund's case behavior discussed is not dependent on the additional interaction terms in the Fermi model used here (P-wave and hyperfine coupling), but only dependent on the Rydberg wave functions. Nevertheless, inclusion of these interactions results in more accurate potential curves and also provides insight into the Hund's case behavior of the hyperfine potentials and molecular states.

Figure 5.5a shows $V_i(Z)$ for the j=3/2 and 5/2 ($22D_j + 5S_{1/2}$) molecules (left) and j=3/2 and 5/2 ($40D_j + 5S_{1/2}$) molecules (right) calculated with all interaction terms in Eq. 5.1, excluding hyperfine-structure coupling. At high n, the molecules trend towards Hund's case (c), where the dominant adiabatic molecular potentials are reduced by the product of two Clebsch-Gordan coefficients of the type $\langle m_\ell = 0, m_s = \pm 1/2 | j, m_j = \pm 1/2 \rangle$. This leads to adiabatic potentials whose depths carry spin-dependent factors $\ell/(2\ell + 1)$ for $j = \ell - 1/2$ and $(\ell + 1)/(2\ell + 1)$ for $j = \ell + 1/2$ [75]. For nD ($\ell = 2$) molecules at high n, the depth ratio of the potentials for $j = 3/2$ and $j = 5/2$ approaches 2/3. This is seen in the depths of the outermost wells of the high-n $j = 3/2$ and $5/2$ ($40D_j + 5S_{1/2}$) molecular potentials in Fig. 5.5a. For decreasing n, the fine structure splitting increases as n^{-3} while the scattering interaction strength increases as n^{-6}, and the molecules tend towards Hund's case (a). The $j = 3/2$ and $5/2$ ($22D_j + 5S_{1/2}$) molecular potentials in Fig. 5.5 exhibit this case, where the scattering interaction strength is large compared to the fine structure splitting. In the low-n limit, the $j = 3/2$ potential becomes notably deeper than the $j = 5/2$ potential.

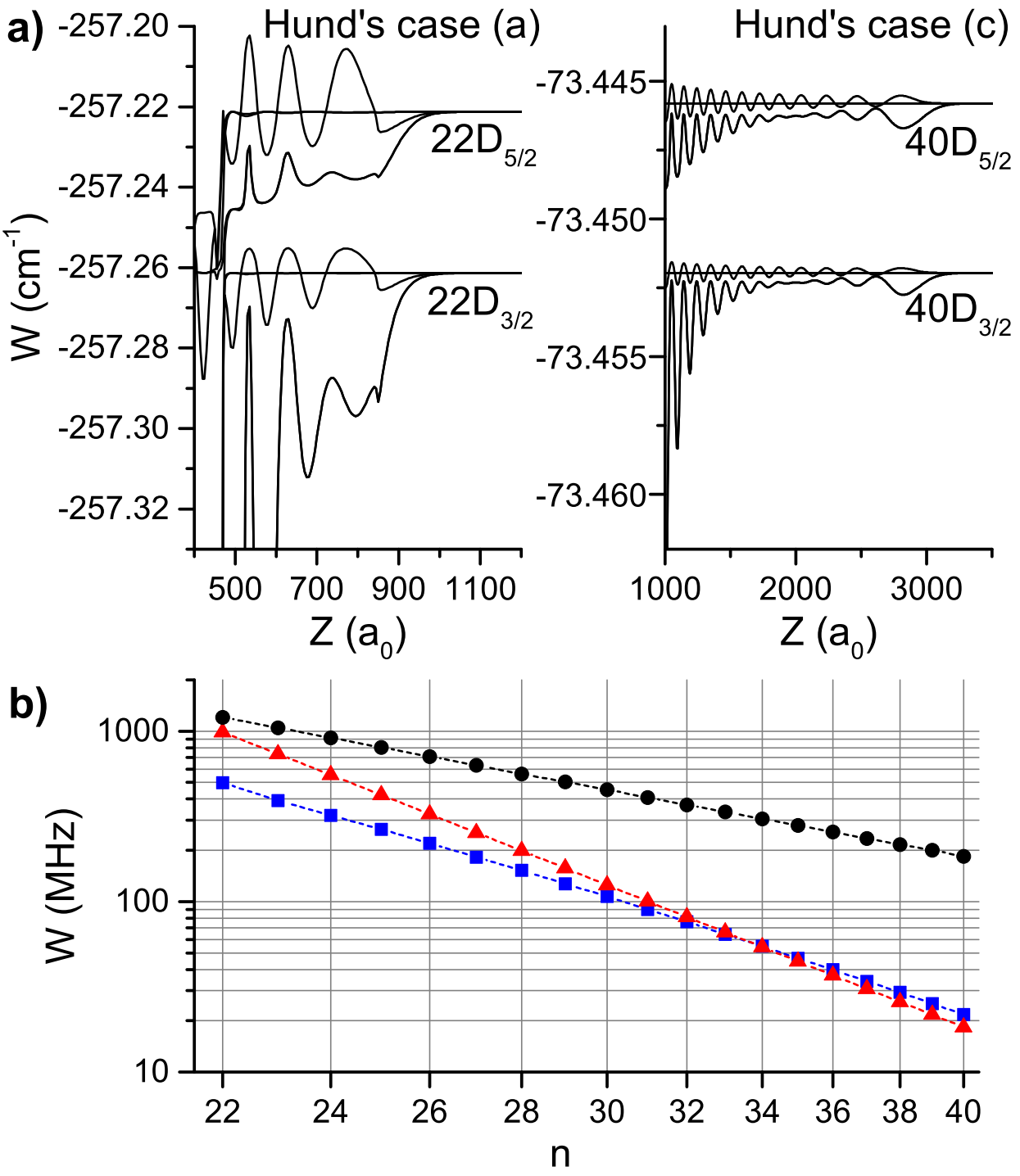

Figure 5.5: a) Adiabatic potentials for ^{87}Rb$(22D_j + 5S_{1/2})$ (left) and ^{87}Rb$(40D_j + 5S_{1/2})$ (right) with ^3S,^1S,^3P,^1P interactions and no hyperfine interaction. b) Binding energies for the $\nu = 0$ ground vibrational state of the $nD_{5/2} + 5S_{1/2}$ (blue squares) and $nD_{3/2} + 5S_{1/2}$ (red triangles) molecular potentials versus n. The D fine-structure splitting is also plotted (black circles).

The binding energies of the vibrational ground states in the outermost potential wells, $W_{i,\nu=0}$, closely track the depth of those wells and therefore mirror the transition of the molecule between the two Hund's cases. In Fig. 5.5b, we plot $W_{i,\nu=0}$ for the $j = 3/2$ and $5/2$ ($nD_j + 5S_{1/2}$) molecules for a range of n from Hund's case (a) (low-n) to Hund's case (c) (high-n). In the high-n limit, the molecular binding energies $W_{i,\nu=0}$ for both fine structure levels approximately scale as n^{-6}, inversely with the atomic volume. In the low-n limit, the lowest binding energy for the lower fine-structure level ($j = 3/2$) is larger and continues to scale as $\sim n^{-6}$, while that of the upper fine structure level ($j = 5/2$) trends towards a $\sim n^{-3}$ scaling, approaching the scaling of the fine structure splitting. For the Rb($nD_j + 5S_{1/2}$) molecules, the binding energies of the vibrational ground states in the outermost potential wells for $j = 3/2$ and $j = 5/2$ are approximately equal at $n = 34$ (see Fig. 5.5b). Further, due to the described Hund's case behavior, at sufficiently low n the inner wells of adiabatic potentials of the $nD_{3/2} + 5S_{1/2}$ molecule become deep enough to support vibrational states that are more deeply-bound and long-lived than the ground states of the outermost well of the $nD_{5/2} + 5S_{1/2}$ potentials.

5.5 Electric and magnetic dipole moments

Rydberg molecules present the only known case of homonuclear molecules with permanent electric dipole moments [4, 28]. For high-ℓ Rydberg molecules dipole moments on the order of 10^3 ea_0 are predicted to exist [4]. Smaller permanent dipole moments arise in low-ℓ S-, P-, and D-type molecules from fractional admixing of high-ℓ state character. Permanent electric dipole moments of ~ 0.5 ea_0 have previously been measured in rubidium S-type Rydberg molecules [28]. Dipolar cesium Rydberg molecules with electric dipole moments of $\sim 5 - 50$ ea_0 [22] have also been prepared. In this section we calculate both the electric and magnetic dipole moments for nD Rydberg molecules, with all terms in the Hamiltonian in Eq. 1 included.

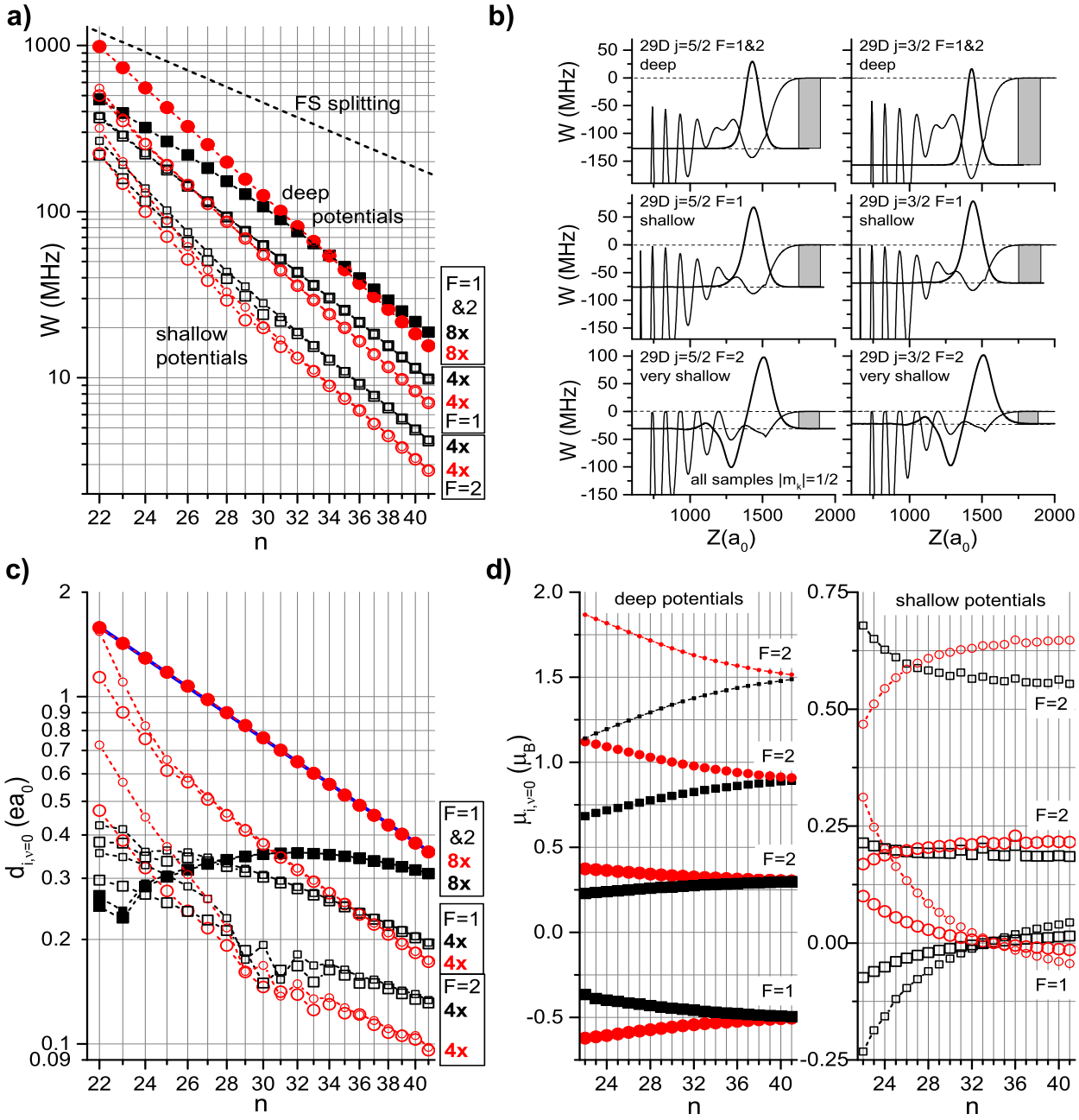

Symbol legend: (See figure caption on the following page.)

Solid: deep, triplet potentials. These are identical for $F = 1$ and $F = 2$.

Hollow: shallow, mixed singlet-triplet potentials. These are different for $F = 1$ and $F = 2$.

Black squares: $j = 5/2$. Red circles: $j = 3/2$.

Large size: $|m_k| = 1/2$. Medium size: $|m_k| = 3/2$. Small size: $|m_k| = 5/2$.

Figure 5.6: a) Binding energies for $\nu = 0$ in the outermost potential wells vs n, with all terms in Eq. 1 included. The $n\mathrm{D}_j$ fine structure splitting is plotted for reference. Numbers indicate degeneracies summed over all m_k. b) Representative adiabatic potentials and wave functions for $^{87}\mathrm{Rb}(29D_j{+}5S_{1/2}, F = 1, 2)(\nu = 0)$, for $j = 5/2$ (left column) and $j = 3/2$ (right column). The pure triplet potentials are the same for $F = 1$ and $F = 2$ (top row), while the mixed singlet/triplet potentials are generally shallow and different for $F = 1$ (middle row) and F=2 (bottom row). The gray bars on the right indicate binding energy, to visualize that the deep potentials are closer to Hund's case (a) ($j = 3/2$ potential deeper than $j = 5/2$ potential) than the shallow ones ($j = 5/2$ potentials deeper than $j = 3/2$ potentials). c) Electric dipole moments $d_{i,\nu}$ for $\nu = 0$ in the outermost potential wells vs n, with all terms in Eq. 1 included. The blue line through the data for the deep $j = 3/2$ potentials is an allometric fit with exponent -2.4. d) Magnetic dipole moments $\mu_{i,\nu}$ for $\nu = 0$ in the outermost potential wells vs n, with all terms in Eq. 1 included. We only show data for positive m_k (results for negative m_k are the same with flipped sign). There are no degeneracies in $\mu_{i,\nu=0}$.

We obtain the adiabatic electric $[d_{i,z}(Z)]$ and magnetic $[\mu_{i,z}(Z)]$ dipole moments in the diagonalization of Eq. 5.1. The dipole moments of a molecular state ν follow from the expectation values of $d_{i,z}(Z)$ and $\mu_{i,z}(Z)$ over the vibrational wave function densities,

$$\begin{aligned} d_{i,\nu} &= \int |\Psi_{i,\nu}(Z)|^2 d_{i,z}(Z) dZ \\ \mu_{i,\nu} &= \int |\Psi_{i,\nu}(Z)|^2 \mu_{i,z}(Z) dZ \quad . \end{aligned} \tag{5.2}$$

Electric dipole moments for the ground vibrational states of the j=3/2 and 5/2 $^{87}\mathrm{Rb}(nD_j + 5S_{1/2}, F = 1, 2)$ deep (pure triplet) and shallow (mixed singlet/triplet) molecular potentials are shown in Fig. 5.6. In Figs. 5.6a and b we show the binding energies and representative potentials with wave functions, respectively, for all angular-momentum coupling cases that arise from Eq. 1. We note that for $^{87}\mathrm{Rb}(nD_j + 5S_{1/2}, F = 1, 2)$ molecules the hyperfine quantum numbers F are well-defined because the hyperfine coupling is much larger than the molecular binding. As seen in Figs. 5.6a and b, the delineation between Hund's cases (a) and (c) is shifted to lower n for the shallow potentials (which are due to hyperfine-induced mixing of singlet and triplet states at the $5S_{1/2}$ atom). Essentially, the generally weaker scattering interaction associated with the mixed singlet/triplet cases pushes those molecules

more towards Hund's case (c).

The electric dipole moments of the deep molecular potentials are 8-fold degenerate when summed over all m_k, and those of the shallow potentials are 4-fold degenerate (see Fig. 5.6c). It is noted that with decreasing n the degeneracies in energy and electric dipole moment become increasingly lifted. This may be attributed to a stronger configuration mixing at low n caused by the relative increase of the e^-+perturber scattering term in Eq. 1. The only case in which the dipole moments of the $^{87}\mathrm{Rb}(nD_j + 5S_{1/2}, F = 1, 2)$ molecules exhibit a clear scaling behavior in n is for the $j = 3/2$ deep potentials (which are the same for $F = 1$ and $F = 2$). A fit to the top-most data set in Fig. 5.6c gives an $n^{-2.4}$ scaling, similar to a result found previously for $^{87}\mathrm{Rb}_2$ S-type Rydberg molecules [28]. Here, the scattering-induced mixing between the atomic Rydberg levels gives rise to a significant change in the electric dipole moments as a function of n. In the range $n \gtrsim 30$, the electric dipole moments for both types of shallow potentials of $^{87}\mathrm{Rb}(nD_{3/2}+5S_{1/2}, F = 1, 2)$ also approximately scale as $n^{-2.4}$. The electric dipole moments for the upper fine structure component $j = 5/2$ have less clear scaling trends (squares in Fig. 5.6c). In particular, the electric dipole moments for the deep $^{87}\mathrm{Rb}(nD_{5/2} + 5S_{1/2}, F = 1, 2)$ potentials do not exhibit a clear scaling behavior. This is likely a result of the transition from Hund's case (a) to Hund's case (c).

The magnetic moments for the molecular states are shown in Fig. 5.6d. The magnetic moments are non-degenerate due to the different g-factors of the involved types of spins. The n-dependence again reflects the transition in angular-momentum coupling behavior between the two Hund's cases (a) and (c). We expect that experiments in weak electric and magnetic fields can reveal the electric and magnetic dipole moments of the vibrational states. The dipole moments computed in this work are for the weak-field limit, *i.e.* results are expected to be accurate as long as molecular Zeeman and Stark shifts are smaller than other relevant energy scales (such as the energy splitting between adjacent vibrational states).

5.6 Hyperfine-structure effects in deep ^{3}S- and ^{3}P-dominated potentials

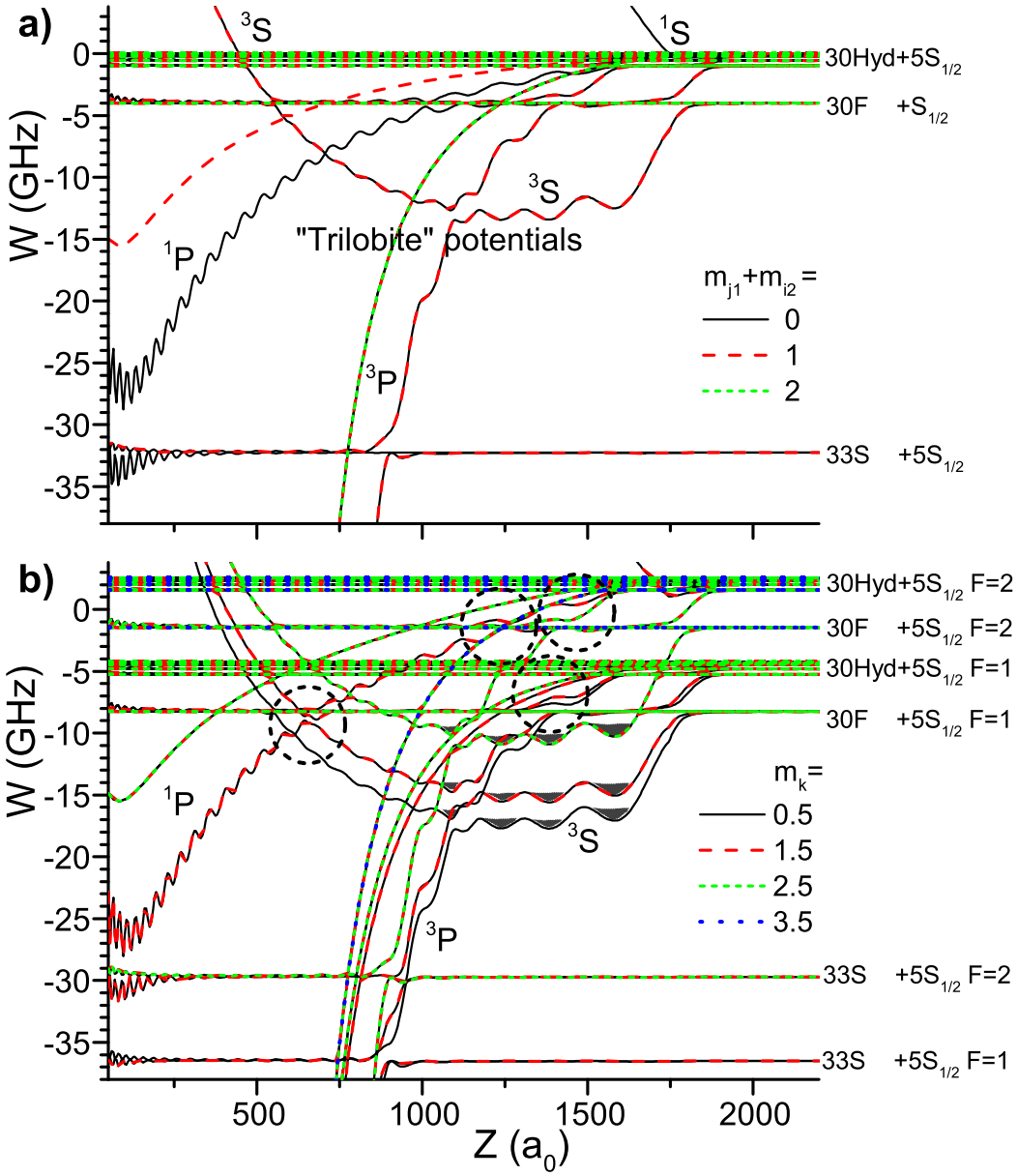

Figure 5.7: High-ℓ adiabatic potentials near $n = 30$ of $^{87}Rb_2$ Rydberg + $5S_{1/2}$ molecules a) without and b) with hyperfine structure included. The plots indicate the trilobite potentials [4], the dominant types of scattering interactions leading to deep potentials, the asmyptotic states of the potentials, the regions where bound trilobite molecules may be found (gray areas), and the intersections between trilobite potentials and F ($\ell = 3$) lines (dashed circles).

The trilobite molecules [4] generated by the ^{3}S interaction are long-range and on the order of 10 GHz deep, which is on the same order as the hyperfine interaction of the $5S_{1/2}$ perturber. It is therefore of interest to explore hyperfine effects on the trilobite adiabatic potentials. In Figs. 7a and b we show these potentials without and with hyperfine coupling for $n = 30$, for all relevant values of $m_{j1} + m_{s2}$ and $m_k = m_{j1} + m_{s2} + m_{i2}$, respectively. While the hyperfine interaction does not affect the general shape and depth of the "trilobite" potentials, with hyperfine structure included there are three instead of only one. Since the number of ^{3}P potential curves also triples, the crossing pattern between ^{3}S and ^{3}P potentials becomes considerably more complex, as seen in Fig. 5.6. Considering that the modulations near the bottom of the "trilobite" potentials are several 100 MHz deep, which is sufficient to support individual bound vibrational states, the hyperfine structure is expected to have profound effects on the detailed vibrational level structure of these molecules. In Fig. 7b, one may expect to find long-lived ^{3}S-dominated states in the gray regions. Further, as indicated by the circles in Fig. 7b, the crossing locations and the detailed coupling behavior of ℓ=3 Rydberg levels (which are optically accessible form low-lying atomic states) to molecular states in the long-range potentials also strongly depend on the hyperfine structure of the system under investigation.

5.7 Summary

In this chapter we systematically explored the role of fine-structure and hyperfine angular-momentum couplings in $^{87}Rb_2$ molecules formed between Rydberg and $5S_{1/2}$ ground-state atoms. As has been done extensively in previous work, we have treated the electron-$5S_{1/2}$ scattering with a Fermi model that includes S-wave and P-wave singlet and triplet scattering. The fine structure mostly influences the behavior of low-ℓ Rydberg molecules. We have explored in detail how ^{87}Rb($nD + 5S_{1/2}$) molecules realize Hund's cases (a) and (c). The hyperfine structure originates in the perturber atom and therefore has consequences for all types (low-ℓ and high-ℓ) of Rydberg molecules. In the case of ^{87}Rb($nD + 5S_{1/2}$)

molecules, mixing of singlet and triplet potentials results in a set of shallow adiabatic potentials, whose quasi-bound states should be experimentally observable (in addition to those in the hyperfine-independent pure triplet potentials). We have obtained electric and magnetic dipole moments, which could, in future work, be measured spectroscopically in weak electric and magnetic fields. The hyperfine structure has also been seen to alter the deep, ^{3}S-scattering-induced trilobite potentials as well as their crossing behavior with ℓ=3 Rydberg states; experimental spectroscopic studies should reveal these details. We expect the hyperfine structure to have a particularly significant effect on Cs_2 trilobite potentials and molecules [96], where the trilobite potentials intersect and strongly mix with the low-ℓ nS potentials. (In Cs the fractional part of the nS quantum defect is small, $\delta_S = 4.05$ [97, 98], making the S-states energetically close to the degenerate high-ℓ manifold.) Since molecular level energies and properties are very sensitive to the scattering phase shifts used in the Fermi model, we expect that spectroscopy of Rydberg molecules can serve as a sensitive tool to provide measurement-based input to future theoretical studies in low-energy electron scattering.

CHAPTER VI

Production and trapping of cold circular Rydberg atoms

This chapter constitutes the second part of the dissertation. Here I move away from molecules formed by Rydberg and ground-state atom interactions and focus on the production, trapping, and dynamics of single Rydberg atoms in extreme angular-momentum or circular states. In the system described, collisional effects between cold circular Rydberg atoms and ground-state atoms nevertheless play an important role, inspiring future work looking for molecular formation in these systems.

Circular Rydberg states correspond to highly-excited, Bohr-like electron trajectories with maximal orbital angular momenta [31]. Circular-state (CS) atoms exhibit a unique combination of properties including long radiative lifetimes $\sim n^5$, large magnetic moments $|m| = \ell = n - 1$, zero linear and small quadratic Stark shits. Several of these features have made CS atoms model quantum systems for a variety of precision measurements [45, 46, 47], which benefit from the reduced nuclear and QED perturbations of these high-angular-momentum states as a result of the small overlap of their torus-like wave functions with the atomic core. Transitions between circular and near-circular states provide a near-perfect two-level system for probing atom-cavity interactions, a feature exploited in landmark cavity-QED experiments [39, 40], a body of work recognized by the 2012 Nobel prize in physics shared by David Wineland and Serge Haroche [42]. A number of proposed

measurements require CS atoms at low temperature. These include an on-going effort towards a high-precision measurement of the Rydberg constant [48] using a shallow optical lattice modulation technique to drive transitions between circular states [49], for which generating circular atoms at low-temperature is a prerequisite. Cold circular Rydberg states have also recently been proposed for use in quantum information processing [50]. The realization of cold high-ℓ Rydberg atoms also enables studied of low-temperature interactions involving high-ℓ Rydberg atoms. These include low-energy collision experiments with circular and high-ℓ states, a regime which has not been explored to date.

In addition to realizing Rydberg atoms at low temperature, many studies and applications require Rydberg atoms to be trapped. For this reason Rydberg atom trapping has been a topic of general interest in recent years, and significant progress has already been made in developing and realizing a variety of trapping techniques. Optical, electro-static and high-gradient magnetic trapping methods for Rydberg atoms have all been considered theoretically [99, 100, 101] and demonstrated in experiments [102, 103, 104, 105]. These have all involved the trapping of atoms in low-ℓ Rydberg states, which can be readily accessed by direct optical excitation in experiments. In addition, the trapping of Rydberg atoms with magnetic fields has also previously only been achieved for mixtures of Rydberg states [105] and not for well-defined quantum states.

In this chapter I describe and demonstrate a technique for producing and magnetically trapping cold circular Rydberg atoms. I begin with an overview of the approach starting with a description of the adiabatic crossed-fields method [5] for producing circular Rydberg atoms. The experiment is then described, including a characterization of the ground-state magnetic trap used and the implementation of the adiabatic crossed-fields method for the production of circular state atoms in the cold ground-state atom sample. The large magnetic moment of a trapped near-circular state atom is measured and its magnetic trapping is characterized by direct spatial imaging of ion distributions, ion counting and state-selective field ionization. A classical model is described and used to determine collision cross sections between circular-

state and ground-state atoms which is found to be in good qualitative agreement with the observed loss rate. The internal-state evolution of circular state atoms in the magnetic trap in a 300 Kelvin background is also probed and found to be in good qualitative agreement with calculated thermally-induced transition rates and internal-state redistribution.

6.1 Adiabatic crossed-fields method for circular state production

Circular Rydberg atoms are in a maximal angular momentum state and therefore cannot be generated by direct optical excitation. In this work cold circular Rydberg atoms are generated using the adiabatic crossed-fields method [5, 36]. This method is well established [37, 106] and is chosen here over others [31, 107] largely due to its relative experimental simplicity, requiring a single optical excitation to a high-lying Stark state and the switching of one external electric field in the presence of a perpendicular magnetic field. Qualitatively, the time-dependent switching of external electric and magnetic fields imparts angular momentum into the atom which results in the circular state. The method is particularly well suited for magnetically trapping circular atoms since the magnetic field required in their production can be provided by the local magnetic trapping field of an already trapped ground-state atom sample. Using this method the circular Rydberg atoms can therefore be generated locally inside a magnetic trap with high spatial resolution, afforded by the initial optical excitation.

The preparation of a circular state by the crossed-fields method is shown schematically in Fig. 6.1. First, a ground-state atom is excited to the upper-most Rydberg Stark state in the hydrogenic manifold of a given n in a large electric field $\mathbf{E}$ and small perpendicular magnetic field $\mathbf{B}$. Here, the field strengths are chosen such that the system is in a Stark-dominated regime, where the Stark frequency $\omega_S = \frac{3nEea_0}{2\hbar}$ exceeds the Larmor frequency $\omega_L = \frac{eB}{2m_e}$. This is followed by a reduction of the electric field to zero such that $\omega_S < \omega_L$, during which the Rydberg atom remains in a well-defined state as it is transferred from a Stark-dominated regime to a Zeeman-dominated regime. Provided the electric field is switched slowly enough,

maintaining adiabaticity, the initial Rydberg Stark state is transferred with high efficiency to the highest level of the Zeeman manifold, which is the circular state with $m = n - 1$.

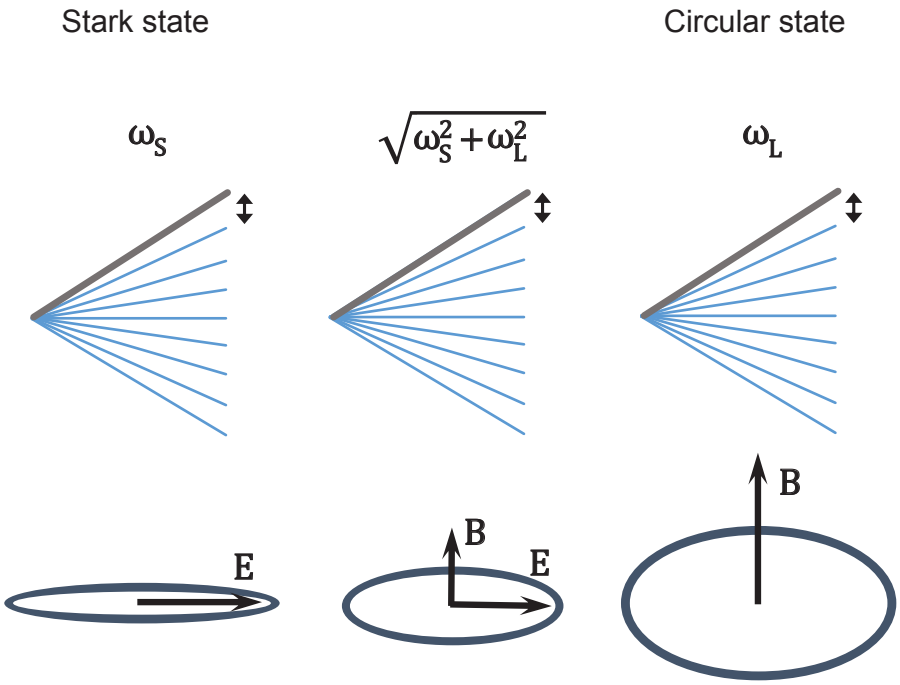

Figure 6.1: Schematic of the adiabatic crossed-fields method for circular state production adapted from [5]. The top row shows the structure of the hydrogenic manifold in the Stark (left), Zeeman (right), and intermediate (middle) regimes. The bottom row shows the classical electron trajectories associated with the upper most state of the corresponding hydrogenic manifold.

An important part of this method is that the initial high-ℓ Rydberg Stark state can be accessed optically. In rubidium and other hydrogen-like atoms, at a sufficiently large electric field the non-degenerate low-ℓ states intersect and mix with the high-ℓ hydrogenic manifolds, making the hydrogenic states optically accessible from low-lying states. The left panel in Fig. 6.2 is a calculated Stark map (with zero magnetic field) in the vicinity of the $n = 57$ hydrogenic manifold in rubidium and its intersection with the $60P$ states. At their intersections, the red-shifted $60P$ Stark states and blue-shifted hydrogenic Stark states couple due to their overlap at the finite-sized ionic core and exhibit avoided crossings.[1] At the avoided crossings, which are seen more clearly in the right panel of Fig. 6.2, the most high-

[1] Chapter 6 in [56].

lying state of the hydrogenic manifold carries enough S and D character at the intersection with the 60P states, and can be optically accessed from low-lying S and P states.

To ensure efficient transfer into the circular state, the initial hydrogenic Stark state must evolve adiabatically during the electric field sweep. The $60P_{1/2}$ avoided crossing in Fig. 6.2 is a good candidate for the initial excitation in this region because it is the first to connect to the upper-most hydrogenic Stark level which then does not cross with other states at lower electric fields. Since the initial excitation is at an avoided crossing, the initially excited Stark state contains a significant amount of low-ℓ character. Here, the electric field must be ramped down adiabatically away from the avoided crossing so to avoid diabatic transitions from this initially excited state into states in proximity of the avoided crossing, and in particular into the nearby red-shifted $60P_{1/2}$ Stark state, which connects to the $60P_{1/2}$ state at zero electric field instead of the circular state.

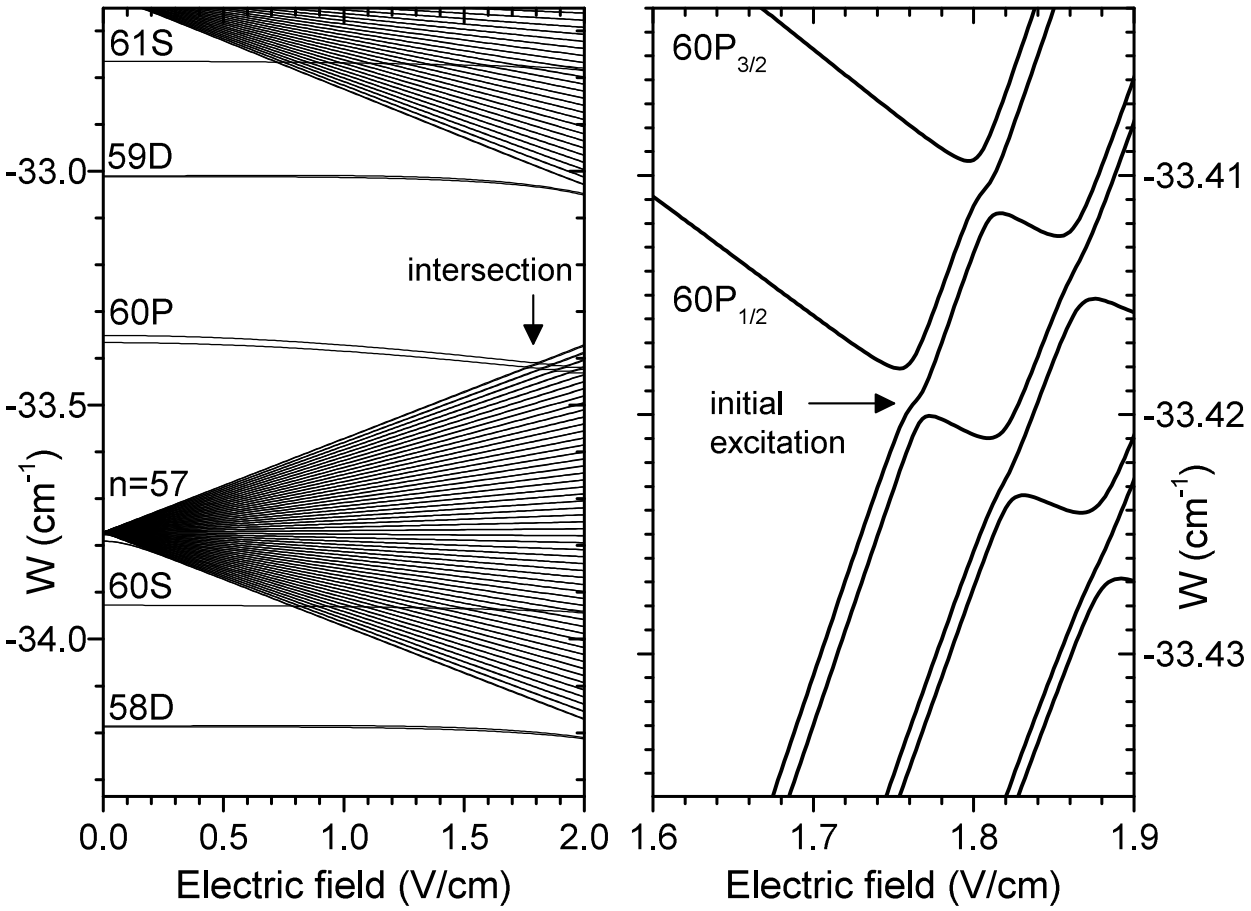

Figure 6.2: Left: Calculated Stark map for rubidium of $m_j = 0.5$ states in the vicinity of the $60P$ and $n = 57$ manifold intersection. Right: High resolution plot of the $60P$ and $n = 57$ manifold intersection indicated in the left panel.

The probability of a diabatic transition into the red-shifted $60P_{1/2}$ Stark state during the onset of the electric field sweep can be estimated using the Landau-Zener formula for the tunneling probability between the most blue-shifted Stark state of the manifold and the red-shifted $60P_{1/2}$ Stark state for an electric field sweep through their avoided crossing. If the unperturbed energy-level separation $W = W_2 - W_1$ of the two states involved varies linearly with time, the Landau-Zener probability P of a diabatic transition from state $|1\rangle$ to state $|2\rangle$ is given by [108]

$$\begin{aligned} \mathrm{P} &= e^{-2\pi\Gamma} \\ \Gamma &= \frac{|a|^2}{\hbar(dW/dt)}, \end{aligned} \tag{6.1}$$

where a is the coupling matrix element connecting two states (in units of energy) and $dW/dt = dE/dt(dW_2/dE - dW_1/dE) = dE/dt\ \Delta(dW/dE)$. The probability of a diabatic transfer from the initial state into the final state depends on their coupling strength, the slew rate of the electric field sweep and the dipole moments of the unperturbed atomic states. For the avoided crossing at the intersection of the $60P_{1/2}$ and $n = 57$ hydrogenic states shown in the right panel of Fig. 6.2, we have $a \approx h \times 10\ MHz$ (equal to half the width of the avoided crossing), and $\Delta dW/dE \approx h \times\ GHz/(V/cm)$. Choosing a slew rate of $dE/dt = 1\ V/cm/\mu s$, the diabatic transition probability P$\lesssim 10^{-2}$ ($2\pi\Gamma \approx 4$) and the evolution from the initial state into the upper most hydrogenic Stark state is well in the adiabatic limit. Here, the slew rate was chosen such that the full electric-field sweep time is less than the relevant Rydberg state lifetimes, which ensures circularization before thermal and radiative decays begin to dominate, and such that the sweep could be realistically implemented in experiments.

Exciting the upper-most hydrogenic Stark state is essential for the efficient production of high-n circular Rydberg states by the crossed fields method so it is important to consider the n-dependence of Γ in Eq. 6.1 when determining experimental parameters. It can be shown that the coupling strength a between intersecting Rydberg Stark states of similar n with $|m| << n$ scales approximately as n^{-4} [56], contributing an n^{-8}-dependence to Γ. This rapid decrease of the coupling strength with n imposes an additional requirement that the excitation bandwidth be less than a/h in order to selectively excite the appropriate level at the avoided crossing. The dipole moments, as discussed previously, scale with the atom size $\approx n^2$, which results in an overall scaling of $\Gamma \approx n^{-10}$. This is significant. Using the avoided crossing at $n \approx 60$ in Fig. 6.2 as an example, the same intersection at $n = 65$ ($\Delta n = +5$) would result in about an order of magnitude increase in the diabatic transition probability for the same electric field slew rate. The choice of the electric field ramp in the vicinity of the avoided crossing therefore largely dictates the efficiency of reaching the upper-most hydrogenic Stark state and ultimately the efficiency of producing circular Rydberg atoms by this method.

Once in the upper-most hydrogenic Stark state, the electric field is decreased within the fixed perpendicular magnetic field such that the atom evolves into the circular state as $\omega_L > \omega_S$. In the transition from the Stark- to Zeeman-dominated regime, the adiabatic condition on the electric field slew rate is given by [5, 36, 37]

$$\frac{dE}{dt} << \frac{e\hbar}{6m_e^2 a_0}\frac{B^2}{n}. \tag{6.2}$$

For the slew rate $dE/dt \approx 1$ V/cm/μs considered above, a transverse magnetic field greater than a few Gauss is required. Generally, from Eqs. 6.1 and 6.2 we see that the adiabatic conditions for efficient circular Rydberg state production by the crossed fields method become more stringent at higher n but can be readily satisfied in most experiments with modest magnetic field strengths and electric field ramp speeds.

6.2 Ground-state magnetic trap

The experiment to produce and magnetically trap cold circular Rydberg atoms begins with a sample of 10^7 ^{87}Rb atoms prepared and magnetically trapped in the $|F{=}2, m_F{=}2\rangle$ ground state at a temperature of $\sim$100 μK and density of $\sim 10^{10}$ cm^{-3}. This is done following the methods described in Chapter III. The trap parameters relevant to the CS experiment are the ground-state trap oscillation frequencies, to which the CS oscillations are later compared, and the magnetic trap field strength at the location of the optical excitation, which provides the magnetic field required in the CS production by the crossed-fields method.

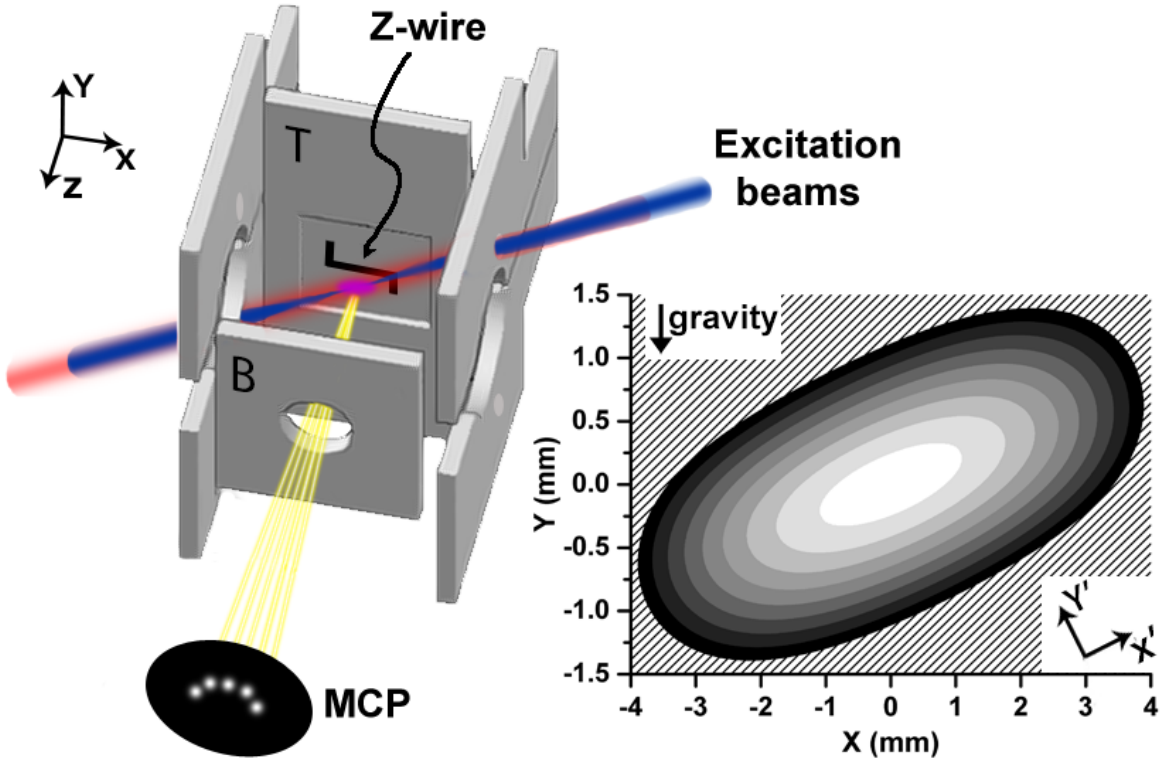

Figure 6.3: Left: schematic of the experiment. Six gold-coated copper electrodes enclose a magnetically trapped atom sample to control the electric fields at the excitation location. An MCP is used for ion detection. The location of the Z-wire and the counter-propagating 480nm and 780nm beams for excitation to Rydberg states are also shown. Right: plot of the magnetic field strength in the xy-plane through the center of the trap. The linear gray-scale ranges from $|B|$=5.5 G (white) to 9.5 G (black) in steps of 0.5 G. The hatched region indicates $|B|\geq$10 G.

A cross section of the magnetic trapping field used in this experiment is shown in Fig. 6.3. The $\omega_{x'}$ and $\omega_{y'}$ ground-state atom trap frequencies are measured by initiating center-of-mass (COM) oscillations of a small, trapped ground-state atom sample and tracking its COM displacement in the trap over time. The ground-state atom sample is first cooled by forced radio-frequency evaporation to a temperature $\leq 30\mu$K resulting in a cloud size with a diameter of ≈ 100 μm along the radial trap axis (cross section in the $y'z'$-plane at x'=0). To measure $\omega_{y'}$, oscillations are induced by shifting the magnetic trap minimum in y by $\approx 250\mu$m and back to its original position by applying a 500 μs-long 0.5 Gauss magnetic field pulse in the z direction. This trap displacement time is chosen to be less than the expected oscillation

period to ensure the atom sample does not adiabatically follow the trap minimum. The top of Fig. 6.4 shows a sequence of absorption images taken of the atom sample with the imaging axis along x' at increasing time delays after the initial displacement. The trap frequencies are independent of the imaging angle so the measurement is unaffected by the choice of primed and non-primed coordinate systems for the imaging axis (see Fig. 6.3). A plot of the atom cloud COM positions as a function of delay time after the initial displacement is shown in the bottom of Fig. 6.4. A sinusoidal fit gives a y' COM oscillation frequency of $\omega_{y'}=2\pi\times39.6\pm0.1$ Hz.

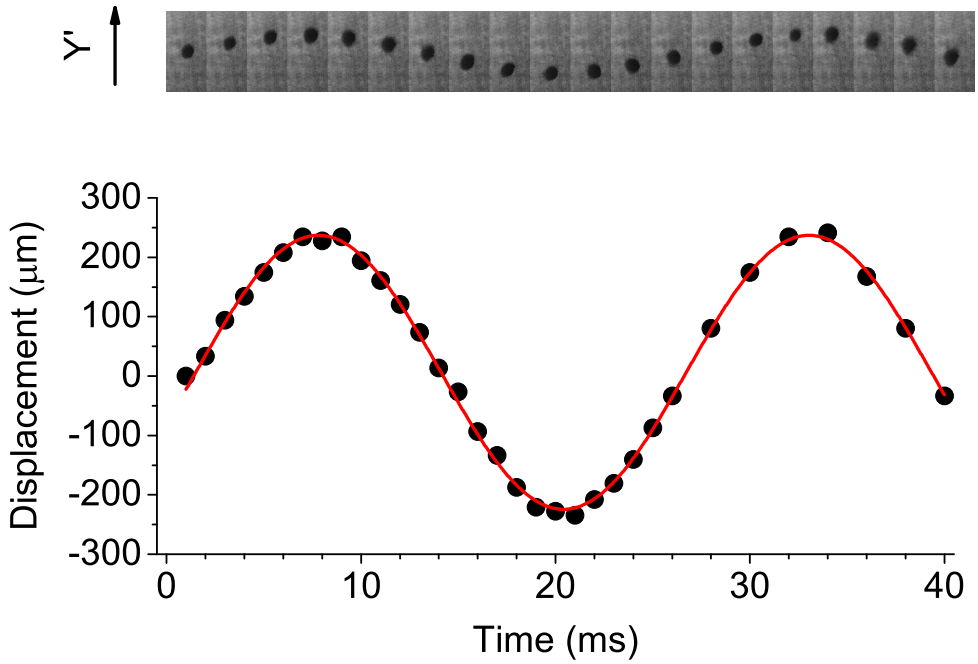

Figure 6.4: Center-of-mass oscillations of the magnetically-trapped ground-state atom cloud along y'. Top: Sequence of absorption images of the oscillating atom cloud in 2 ms time intervals from 2 ms to 40 ms (left to right) after the initial trap displacement. Bottom: Center-of-mass positions from the top image sequence as a function of delay time after the initial displacement (black circles). The sinusoid fit (red curve) gives an oscillation frequency $\omega_{y'}=2\pi\times39.6\pm0.1$ Hz.

To measure $\omega_{x'}$, the atom sample itself is displaced away from the trap minimum by imparting momentum to the COM of the atom cloud with a resonant optical pulse. This is done instead of a displacement of the trap minimum in x' because such a displacement cannot be achieved by the application of a single external bias field with a Z-wire magnetic trap configuration.

The evaporatively-cooled atom sample is illuminated for 100 μs by a laser beam tuned to resonance with the ^{87}Rb $5^2S_{1/2} \rightarrow 5^2P_{3/2}$ transition at an intensity of $I_{sat}/5$, directed mostly along the x' direction of the elongated atom trap, and whose size is large enough to ensure a near-uniform intensity distribution across the entire atom cloud. This intensity corresponds to a photon scattering rate of $3.1 \times 10^6\ s^{-1}$ and an average COM momentum transfer to the atom sample of $m_{87} \times 3.1 \times 10^6\ s^{-1} \times 100\ \mu s \times v_{recoil} = \approx m_{87} \times 2$ m/s, where the photon recoil velocity v_{recoil}=5.88 mm/s [3] and m_{87} is the rubidium atom mass. The atom sample COM then becomes initially displaced along the x' direction by $\approx 180\ \mu m$ from the trap minimum. The pulse duration is much less than the expected oscillation period which again ensures a non-adiabatic displacement of the atom sample from the minimum of the trap. The pulse area is chosen such that the number of photons scattered does not cause substantial heating and diffusion of the atom cloud during its subsequent oscillations. The COM motion along x' is tracked by taking absorption images of the atom sample at increasing delay times from the initial optical pulse. The imaging axis and initial COM velocity component deviate from the x'-axis of the magnetic trap by a small angle, allowing low amplitude oscillations to be observed in the absorption images. A sinudoidal fit to the observed COM displacements over time (not shown) gives an x' COM oscillation frequency of $\omega_{x'}$=$2\pi \times 7.9 \pm 0.3$ Hz.

Having measured the relevant ground-state magnetic trap frequencies, we next measure the magnetic field strength at the center of the ground-state atom trap used in the circular state production by the cross-field method. The magnetic field at the bottom of the ground-state atom trap is measured by taking advantage of the position-dependent Zeeman shifts of ground-state magnetic sub-levels in the magnetic trapping potential. Atoms in the trap that are located at the trapping-field minimum $|B_0|$ experience the smallest trap-induced Zeeman shifts and can be selectively probed using the RF evaporative cooling sequence described in section 3.1.2 to measure the value of $|B_0|$. Here, the number of atoms remaining in the trap after one evaporation sequence is monitored as a function of RF stop frequency ν_{RF}^{stop}. The ν_{RF}^{stop} at which all of the atoms are removed from the trap corresponds to the Zeeman

splitting at the minimum trapping field strength, which is given by

$$|B_0| = \frac{\nu_{RF}^{stop}}{700 \text{ kHz/Gauss}}, \tag{6.3}$$

where 700 kHz/Gauss is the Zeeman splitting between adjacent m_F sub-levels of the $|5S_{1/2}, F = 2\rangle$ atoms [3]. The field minimum for the trap in Fig. 6.3 is measured to be 5.7±0.6 G, where the uncertainty is given by the 10% shot-to-shot fluctuation in the atom number measurements.

6.3 Production of circular states by the adiabatic crossed-fields method

The production of circular state Rydberg atoms is accomplished using the crossed-field method described in section 6.1. As discussed, good control of electric fields is important when producing circular states using this method. To selectively excite the initial Stark state, the electric field needs to be homogeneous enough to not broaden the lines at the Stark $60P$ and $n = 57$ manifold intersection such that the states are distinguishable at the avoided crossings. The electric field also needs to be controlled to a level such that for a given transverse magnetic field the condition $\omega_S < \omega_L$ is satisfied at the end of the electric field ramp. In this experiment, the magnetic trapping region is enclosed by an electrode structure consisting of six individually-addressable electrodes, shown in Fig. 6.3, with which the electric fields are controlled to an accuracy of ≤30 mV/cm in all coordinates by Stark spectroscopy on high-lying Rydberg states on $85D$ Rydberg states, following the methods described in chapter III. The electrode labeled "T" is used for Rydberg-atom field ionization and the electrode labeled "B" produces the electric field ramp required for the CS production. The MCP located 10 cm from the excitation region is used for ion detection, which in this case includes spatial imaging of the ion distributions and time of flight information as well as ion counting.

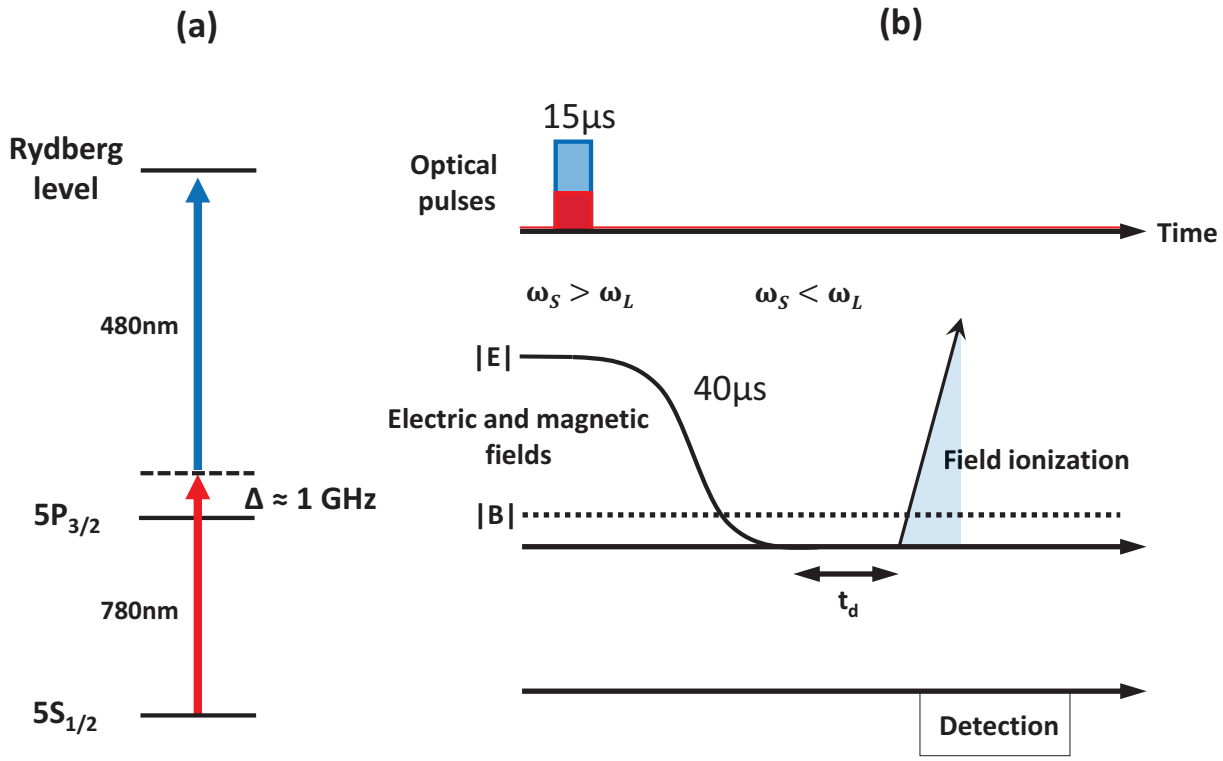

Figure 6.5: Left: Schematic of the two-photon excitation to Rydberg states. Right: Schematic of the experimental timing sequence for Rydberg excitation, field-ionization and detection.

A schematic of the experimental timing sequence is shown in Fig. 6.5b. Circular Rydberg atoms with principal quantum number n=57 are generated by first optically exciting, in the presence of an electric field $\mathbf{E} = -E\hat{\mathbf{z}}$ generated by applying a voltage to the B-electrode, into the highest-lying Stark state of the n=57 hydrogenic manifold. This is done by a two-photon excitation with 480 nm and 780 nm laser beams as shown in Fig. 6.5a, which are pulsed on simultaneously as shown in Fig. 6.5b. The frequency of the 780 nm laser is fixed 1 GHz off-resonance from the $5S_{1/2} \rightarrow 5P_{3/2}$ transition to minimize heating of the ground-state atom sample over a series of excitations in a single ground-state atom sample. The 480 nm laser is frequency tunable to excite Rydberg levels. The 480 nm beam is focused to a waist of w_0=50 μm and the 780 nm beam is collimated to w_0=1.5 mm, with powers of 35 mW and 2 mW, respectively. Both beams are linearly polarized perpendicular to the axis of the applied electric field. As seen in Fig. 6.2, at a field of ≈1.8 V/cm the 60P states intersect with

the n=57 hydrogenic states. Experimental and calculated two-photon excitation spectra of this region are shown in Fig. 6.6a and b, respectively. In the experimental spectrum, we see the hydrogenic states appear only in regions where they intersect with 60P states due to field-induced state mixing of S and D character into the P Rydberg states. The coupling between the 60P and high-ℓ hydrogenic Stark states is evident at their intersections, which are avoided crossings with splittings of 20 MHz or more. These features are reproduced in the calculated spectra in Fig. 6.6b, which shows calculated energy-levels with the small 5.7 Gauss perpendicular magnetic field from the magnetic trap taken into account, as well as the two-photon excitation rates for the experimental parameters used. The calculated two-photon excitation rates take into account the effects of laser line widths and inhomogeneous field broadening evident in the experimental spectrum. A detailed description of the two-photon excitation rate calculations is given in Appendix C. For the initial step in the CS production we excite to regions labeled I and II in Fig. 6.6a. Regions labeled IV are avoided crossings with state crossings at lower electric-field values and are therefore not chosen for the initial excitation in the circular state production. Region labeled III marks the red-shifted $60P_{1/2}$ Stark state away from its avoided crossing with the upper-most hydrogenic Stark state.

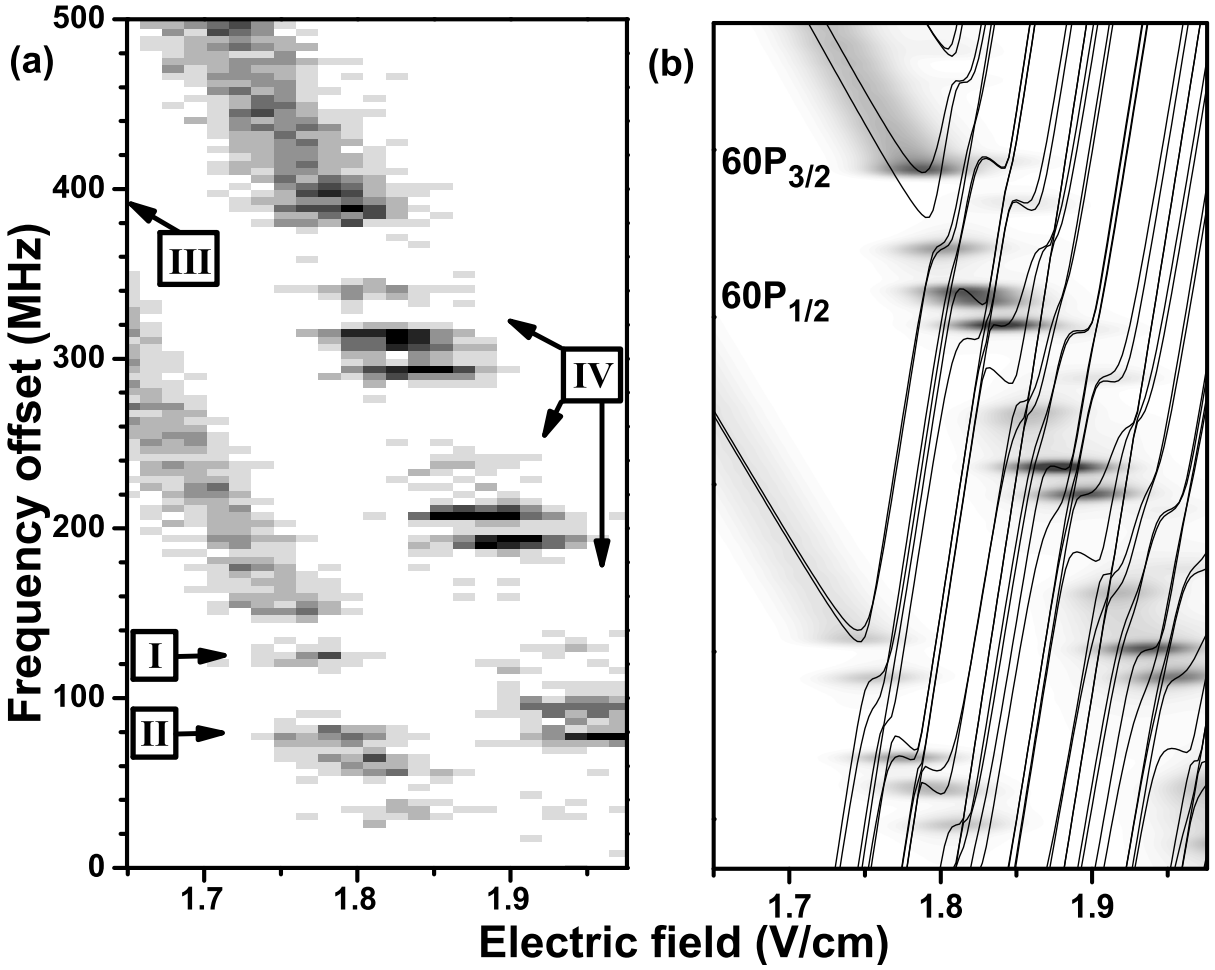

Figure 6.6: (a) Experimental Stark spectrum showing the intersection of 60P with the n=57 hydrogenic manifold. Plotted are average counts per excitation pulse (linear scale ranging from 0 (white) to >3.5 (black)) as a function of applied electric field and frequency offset of the 480 nm laser from an arbitrary reference frequency. Each data point is an average of 50 excitation pulses. The electric field axis is scaled by a factor of 0.98 to match the calculation in (b). Minor deviations in frequency between (a) and (b) are attributed to long-term excitation-laser drifts. (b) Energy levels (solid lines) and excitation rates per atom calculated for our laser polarizations and intensities (overlay; linear gray-scale from 0 to 150 s^{-1}). In the excitation-rate calculation we assume Gaussian distributions for the excitation frequency and electric field, with FWHM of 5 MHz and 50 mV/cm, respectively.

After a 15 μs excitation pulse to region I, the electric field is ramped down over 40 μs from its initial value of 1.76 V/cm to 0 V/cm, within the residual electric-field uncertainty. This ramp speed is slow enough to ensure adiabatic evolution of the Rydberg atoms within the avoided crossings in Fig. 6.6. (This is 40× slower than the adiabatic ramp described in section 6.1 for the states of interest and well within the adiabatic transfer limit given by 6.1). To avoid

abrupt changes in field during switching, the ramp is also designed with some curvature in its initial and final sections, as shown in Fig. 6.5b. Here, the 5.7 G magnetic field at the bottom of the atom trap is always on and is perpendicular to the ramped electric field. At the beginning of the electric field ramp the Stark frequency $\omega_S \approx 2\pi \times 200$ MHz is much larger the fixed Larmor frequency ω_L=$2\pi\times8$ MHz. At the end of the ramp, the residual Stark frequency $\omega_S \lesssim 2\pi\times3$ MHz, which is less than the Larmor frequency in the magnetic field of the trap. In the adiabatic sweep from the Stark-dominated ($\omega_S > \omega_L$) to the Zeeman-dominated regime ($\omega_S < \omega_L$) the atoms initially prepared into region I in Fig. 6.6a evolve with near unity probability into the $|n$=57, ℓ=56, m_ℓ=56, m_s=+0.5$\rangle$ CS. The CS has good quantum numbers m_ℓ and m_s because in high-ℓ states the Zeeman effect dominates their small fine structure coupling (see sections 2.2 and 2.3). The magnetic field stabilizes the CS by lifting its degeneracy with any other hydrogenic state. Here, the angular momentum of the trapped CS atom is parallel to the magnetic field at the trap minimum, which points along $\mathbf{x}'$ in Fig. 6.3. This CS is low-field seeking. The complementary $|n$=57, ℓ=56, m_ℓ=-56, m_s=-0.5$\rangle$ CS is connected to the red-most shifted hydrogenic Stark state in the Stark limit (see left panel of Fig. 6.2), and is unsuitable for magnetic atom trapping because it is a high-magnetic-field seeking state.

6.4 Circular-state trapping and center-of-mass oscillations

Due to their large magnetic moments, CS atoms in a magnetic trap experience significantly deeper confining potentials than ground-state atoms. The magnetically trapped $|F$=2, m_F=2$\rangle$ atoms (Landé factor g_F=$\frac{1}{2}$) have a magnetic moment of one Bohr magneton, $\mu_{GS} = -\mu_B$. The CS atoms described above have a magnetic moment μ_{CS}=$-\mu_B(m_\ell + g_s m_s)$=$-57\mu_B$, where $g_s \approx 2$. In a harmonic magnetic trap, the CS atom experiences a potential increase, U_{CS}=$(\frac{\mu_{CS}}{\mu_{GS}})U_{GS}$=$57U_{GS}$, and a corresponding trap frequency increase, ω_{CS}=$\sqrt{57}\omega_{GS}$, where U_{CS} and U_{GS} are the CS and ground-state magnetic potentials, and ω_{CS} and ω_{GS} are the CS and ground-state trap frequencies, respectively.

The minimum of the ground-state trap is substantially shifted due to gravity, while in the much stronger CS trap gravity can be ignored. This is illustrated in Fig. 6.7. The displacement vector pointing from the minimum of the ground-state trap to the minimum of the CS trap is calculated to be $\delta\mathbf{r} = (\delta x, \delta y, \delta z) = (710, 290, 0)$ μm, which is determined using calculated force constants and the 12±0.2 degree tilt of the trap with respect to gravity (see Fig. 6.3). This displacement of the trap minimum allows us to initiate sloshing-mode oscillations of trapped CS atoms in the $\mathbf{x}'$ and $\mathbf{y}'$ directions by doing the initial optical excitation and production of the CS at the center of the ground-state magnetic trap.

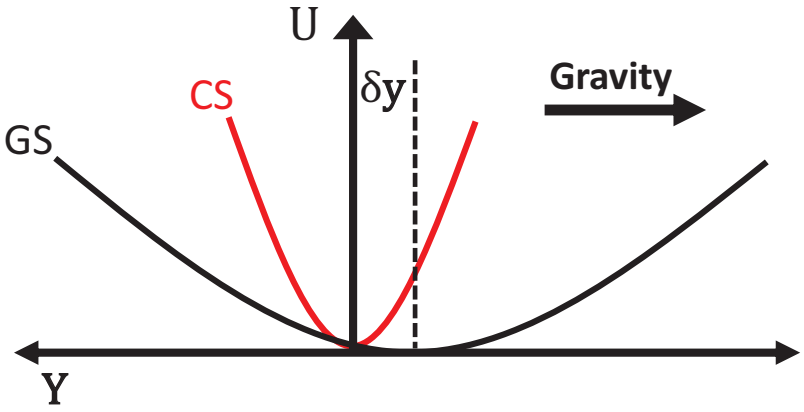

Figure 6.7: Illustration of the circular Rydberg atom magnetic trap displacement from the ground-state atom magnetic trap along $\mathbf{y}$.

To observe these oscillations the $|CS-1\rangle \equiv |n{=}57,\ \ell{=}56,\ m_\ell{=}55,\ m_s{=}{+}0.5\rangle$ near-CS is generated by an initial excitation to region II in Fig. 6.6. Excitation to region II is chosen because it provides a stronger experimental signal than I; both regions result in high-ℓ states that exhibit quantitatively similar trapping behavior. The expected trap period for the near-CS is $T_{CS-1}{=}\frac{T_{GS}}{\sqrt{n-1}}$, which equals 16.9 ms and 3.4 ms in $\mathbf{x}'$ and $\mathbf{y}'$, respectively. Since the excitation and circularization time interval of 55 μs is much smaller than T_{CS-1}, the atoms are prepared on the side of their trapping potential U_{CS-1}, at the location -$\delta\mathbf{r}$. A fast field-ionization pulse is applied at varying time-delays, t_d, from the end of the $|CS-1\rangle$ production, as shown in Fig. 6.5b. The ion positions are projected onto the MCP, where they generate spatially-resolved light pulses on a phosphor screen, which is imaged by a CCD

camera. The center-of-mass (COM) coordinates of the ion distributions in the MCP plane are obtained from sums of 2000 images at each t_d. Plots of the **x** and **y** COM coordinates as a function of t_d are shown in Fig. 6.8. The **y** COM data (Fig. 6.8a) is fit to a sinusoid out to 4 ms which gives an oscillation period of 3.4±0.1 ms. This is in excellent agreement with the predicted value. The **y** COM data is only considered out to 4 ms because of distortions in the ion trajectories thereafter, as suggested by the **x** COM data. Since $\delta x \approx 2.5\delta y$, a larger COM oscillation amplitude in **x** is expected. The **x** COM coordinate plotted in Fig. 6.8b develops a large displacement over about 4 ms. At t_d=4 ms there is an apparent reversal in the direction of motion of the **x** COM coordinate, which occurs about a factor of two earlier than expected. A possible explanation for this is that the **x** COM oscillation amplitude is so large that it brings the ions produced by field-ionization far enough off of the ion-imaging axis causing distortion and obstruction (see Fig. 6.8c and discussion below). This prevents a direct measurement of the **x** COM oscillation period, as well as the **y** COM oscillation period after 4 ms. A video of a time-series of composite images showing the evolution of the ion distribution as a function of t_d can be found in online supplemental material at `http://journals.aps.org/pra/abstract/10.1103/PhysRevA.88.031401#supplemental` [53].

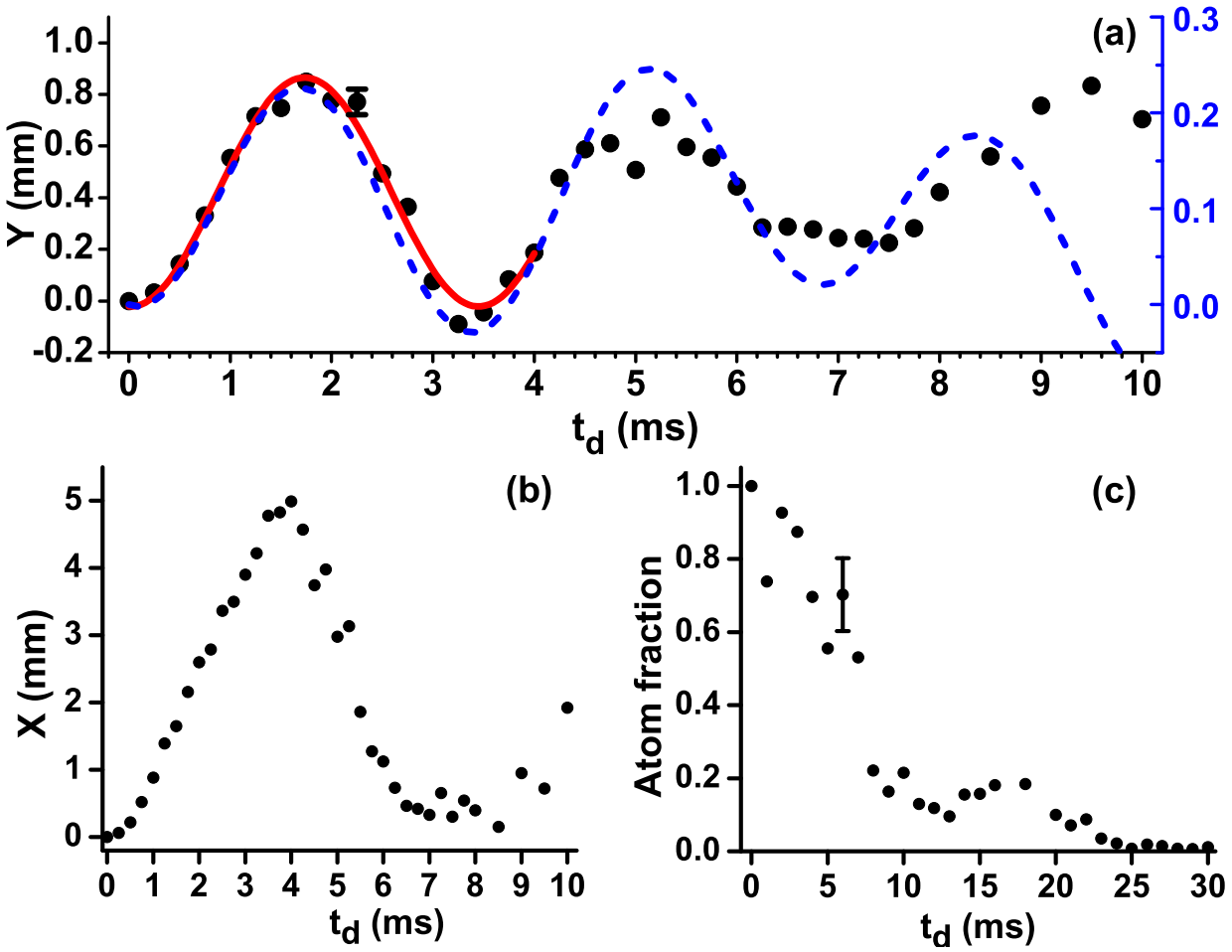

Figure 6.8: (color online). (a) Experimental center-of-mass (COM) displacement in **y** vs t_d (circles) in the MCP plane (left axis) with a fit to a sinusoid out to 4 ms (solid curve). The RMS spread of the data about the fit is 0.05 mm, indicated by the representative error bar. The simulated COM displacement in **y** vs t_d in the object plane (right axis) is shown out to 10 ms (dashed curve). A linear offset is subtracted to match the experimental data, accounting for ion-imaging abberations. (b) Experimental COM displacement in **x** vs t_d. (c) Fraction of detected atoms remaining vs t_d. Based on the variance of the data points, we estimate an uncertainty shown by the representative error bar.

To model the system, we perform Monte Carlo simulations of the internal-state evolution of a sample initially in the state $|CS-1\rangle$ in a T=300 K radiation background. Atom trajectories inside the magnetic trapping field are computed classically using a Runge-Kutta method. The simulations account for all radiative transitions, including thermal photoionization, but do not account for collisions. During its evolution in the trap, a typical circular atom undergoes many thermally-driven state transitions. The internal-state evolution changes m,

which in turn changes the COM motion of the atom sample in the magnetic trap. The internal-state evolution and trajectories are therefore coupled by the m quantum number. The calculated rate of thermally-induced transitions per atom is 6×10^3 s^{-1}, corresponding to about 60 thermal transitions over the 10 ms observation time in the COM measurement in Fig. 6.8. (For comparison, in a T=4 K cryogenic enclosure the thermal transition rate would be 0.1×10^3 s^{-1}, corresponding to 1 thermal transition over 10 ms.) The rapid state evolution from the $|CS-1\rangle$ due to the 300 K thermal radiation results in n-, ℓ- and m-redistribution of the initially prepared sample, leading to a time dependence of the average magnetic dipole force as well as a diffusive component of that force. The change in average m amounts to less than 1% over the 10 ms observation time. The corresponding change in average oscillation frequency is too small to be seen in the experiment. The diffusive component of the m evolution is more significant, reaching an RMS spread of $\pm15\%$ about the average m over 10 ms. This is large enough that some damping effect on the COM oscillations is expected. From the simulations we obtain COM trapping frequencies and decay constants of 16.5 ms and 36.2 ms in $\mathbf{x}'$ and 3.4 ms and 10.2 ms in $\mathbf{y}'$, respectively. In Fig. 6.8a the simulated $\mathbf{y}$ COM oscillation is plotted with a linear offset subtracted to match the experiment, accounting for ion-imaging abberations. In the simulation, we test the importance of thermally-driven m-state diffusion by turning off all radiative transitions, leaving trap anharmonicity-induced dephasing as the sole source of damping. We find that m diffusion and trap anharmonicity contribute in approximately equal parts to the decay of the COM oscillations over 10 ms.

6.5 Circular-state trap lifetime

To measure the magnetic trapping time, the number of detected Rydberg atoms is plotted as a function of t_d. Figure 6.8c shows the fraction of Rydberg atoms detected relative to t_d=0. As much as 70% of the initially prepared sample is found to remain in the trap after 6 ms. If any 60P atoms remained after the circularization sequence, our simulations show that only

a $\sim 5 \times 10^{-5}$ fraction of them would survive after 6 ms. From this we conclude that the crossed-fields circularization procedure implemented in the experiment is very efficient. In Fig. 6.8c one also sees that between 7 and 13 ms there is a rapid drop in ion signal, as well as a significant resurgence of ion signal at about 16 ms. The rapid drop is likely due to atoms moving out of the ion imaging field-of-view in the **x** direction, while the resurgence occurs because of atoms moving back into view along this axis at later times in their oscillation. This scenario is consistent with both the expected **x** oscillation period (16.5 ms) as well as the early reversal of the **x** COM evident in Fig. 6.8b.

From Fig. 6.8c we estimate an overall loss rate of $\gtrsim$50 s^{-1} for the trapped CS population. Collisions between Rydberg atoms are not expected to be significant given the low Rydberg atom densities used here, which are typically a few $\times 10^6$ cm^{-3} after optical excitation, and therefore unlikely to contribute to the observed loss. Our simulations of the state evolution show a loss rate of about 0.5 s^{-1}, (again at 300 K and accounting for all non-collisional loss channels), which is negligible in comparison to the measured loss rate. The observed loss rate is consistent with collisions between Rydberg and ground-state atoms being the primary loss mechanism, which is not unexpected given the long time the CS atom spends oscillating through the sample of trapped ground-state atoms. This loss rate is estimated from collisional cross sections between Rb low-ℓ Rydberg and ground-state atoms provided in [56].[2] However, the loss rate cannot be fully explained at a quantitative level because low-velocity CS atoms have not been produced in the lab until now and data on their collision cross sections are not available.

6.6 A model for collisions between circular Rydberg and ground-state atoms

Due to their large sizes, Rydberg atoms exhibit properties that are both quantum and classical in nature [109]. The classical view of the properties of Rydberg atoms follows from

[2]Depopulation cross sections are given on page 221 in [56]

the correspondence principle, which dictates that quantum mechanics in the limit of large quantum numbers must reproduce classical physics. Accordingly, classical simulations of Rydberg atom trajectories are often used to describe the dynamics and behavior of Rydberg atoms [110, 111]. It stands to reason, then, that a description of the collision behavior of Rydberg atoms may also be approached using a classical model.

In this section, the scattering cross sections for low-energy collisions between circular Rydberg and ground-state atoms are calculated using a classical model in which the ground-state atoms are treated as point-like particles impinging on the much larger circular Rydberg atom. A schematic is shown in Fig 6.9. In the model, a collision between the two atoms occurs with unity probability when the ground-state atom hits a classically allowed region within the Rydberg-atom wave function, ψ, and with zero probability if the ground-state atom passes through a classically forbidden region. The probability of a collision between the two atoms is therefore determined entirely by the spatial extent of ψ. For a given orientation of ψ during a collision event, the effective scattering cross section, σ_{eff}, is defined by the area projection of $|\psi|^2$ for the classically allowed regions of ψ onto the plane whose normal vector lies along the direction of motion of the ground-state atom (corresponding to the drop shadow on the plane in Fig. 6.9). The classical nature of the model rests upon the fact that the effective collision cross section is defined by the area projection of a well-defined classical object in three-dimensional space. Averaging over the full solid angle gives the total collision cross section,

$$\sigma = \frac{1}{4\pi} \int_0^{4\pi} \sigma_{eff}(\theta, \phi) \mathrm{d}\Omega. \tag{6.4}$$

The azimuthal symmetry of $|n, \ell = m\rangle$ hydrogenic wave functions simplifies Eq. 6.4 for the circular state ($\ell = m = n - 1$) by requiring an integration only over all θ interaction angles. Rydberg states with $\ell \neq m$ are not symmetric about ϕ and require an integration over both θ and ϕ.

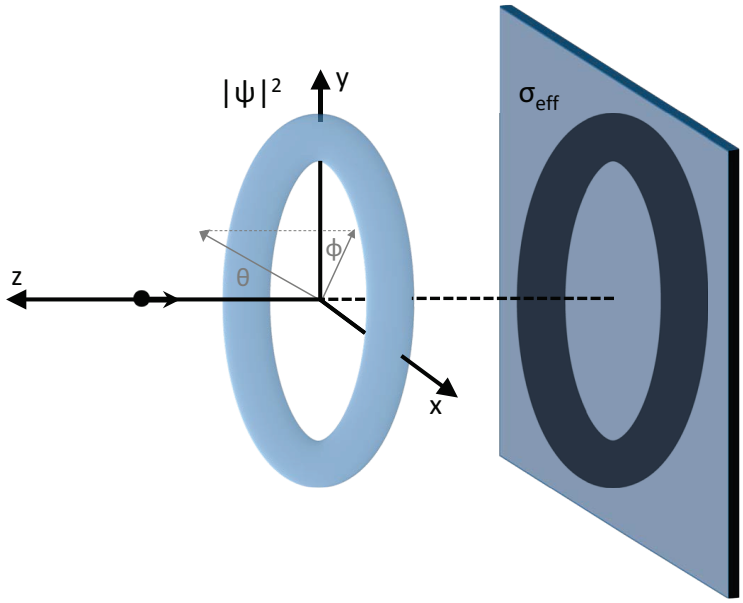

Figure 6.9: Schematic of the classical model for collisions between circular Rydberg atoms and ground-state atoms.

Classical turning points

For a quantum particle in an external potential, the classical turning points separate the classically-allowed and classically-forbidden regions of the particle wave function ψ. With increasing particle energy, the particle's probability density becomes concentrated around these turning points where the kinetic energy and the potential energy are equal. It follows from Eq. 2.1 that the curvature of ψ is identically zero at the classical turning points. Due to the separability of the Schrödinger equation in spherical coordinates (see sec. 2.1), the classical turning points of the hydrogenic states under consideration are determined independently for the radial and angular components of ψ.

The classical turning points of the radial wave function $u_{n,\ell}(r)$ are determined by finding the values of r where the wave function has an inflection point, or equivalently where the bound-state energy of the electron (E_n) equals the effective potential energy ($V_{\text{eff}}(r)$) in the radial wave equation (Eq. 2.6). We have

$$-\frac{\mu c^2 \alpha^2}{2n^2} = \frac{\ell(\ell+1)\hbar^2}{2\mu r^2} - \frac{e^2}{4\pi\epsilon_0 r}, \tag{6.5}$$

which, when multiplying through by $2r^2$, rearranging and converting into atomic units (letting $\mu = 1$) gives

$$\frac{1}{n^2}r^2 - 2r + \ell(\ell+1) = 0, \tag{6.6}$$

The roots of this quadratic equation give the classical turning points

$$r_{TP}^{\text{in}} = n(n - \sqrt{n^2 - \ell(\ell+1)}) \tag{6.7}$$

$$r_{TP}^{\text{out}} = n(n + \sqrt{n^2 - \ell(\ell+1)}). \tag{6.8}$$

Figure 6.10a shows a plot of Eqs. 6.7 and 6.8 for the circular states ($\ell = n - 1$) from n=1 to 65. Allometric fits show an n-scaling of $\sim n^{1.93}$ and $\sim n^{2.09}$ for r_{TP}^{out} and r_{TP}^{in}, respectively, deviating slightly from the n^2 scaling of their average value (not shown). The gray-shaded area indicates the classically-allowed region. The difference of the two turning points (r_{TP}^{out}-r_{TP}^{in}) gives the classical width of the circular state wave function along its radial dimension. This is also shown in Fig. 6.10a, with an allometric fit giving the $\sim n^{3/2}$ scaling expected from the difference of Eqs. 6.8 and 6.7 for $\ell = n - 1$.

The classical turning points of the angular wave function $\mathrm{Y}_{\ell,m}(\theta,\phi)$ are obtained by finding the angular coordinates at which its curvature equals zero. Due to the ϕ symmetry of the circular state (and all other $\ell = m$ states), only the θ coordinate needs to be considered. Following from Eq. 2.5, the inflection point is the obtained by solving

$$\frac{\partial^2}{\partial\theta^2}P_\ell^m(\theta) = 0. \tag{6.9}$$

Derivatives of the associated Legendre functions for arbitrary ℓ and m can readily be computed numerically (see, for example, methods to compute the derivatives of the associated Legendre function in Ref. [112]). In the present context, the solutions to Eq. 6.9 simplify

significantly for $\ell = m$ states and the turning points are given by the expression

$$\theta_{\mathrm{TP}} = \pm \arccos(\pm \frac{1}{\sqrt{\ell}}). \tag{6.10}$$

Classical turning points of the angular wave function for the $|n, \ell = m = n-1\rangle$ circular states are plotted in Fig. 6.10b up to $n = 65$ with classically-allowed regions shaded in gray.

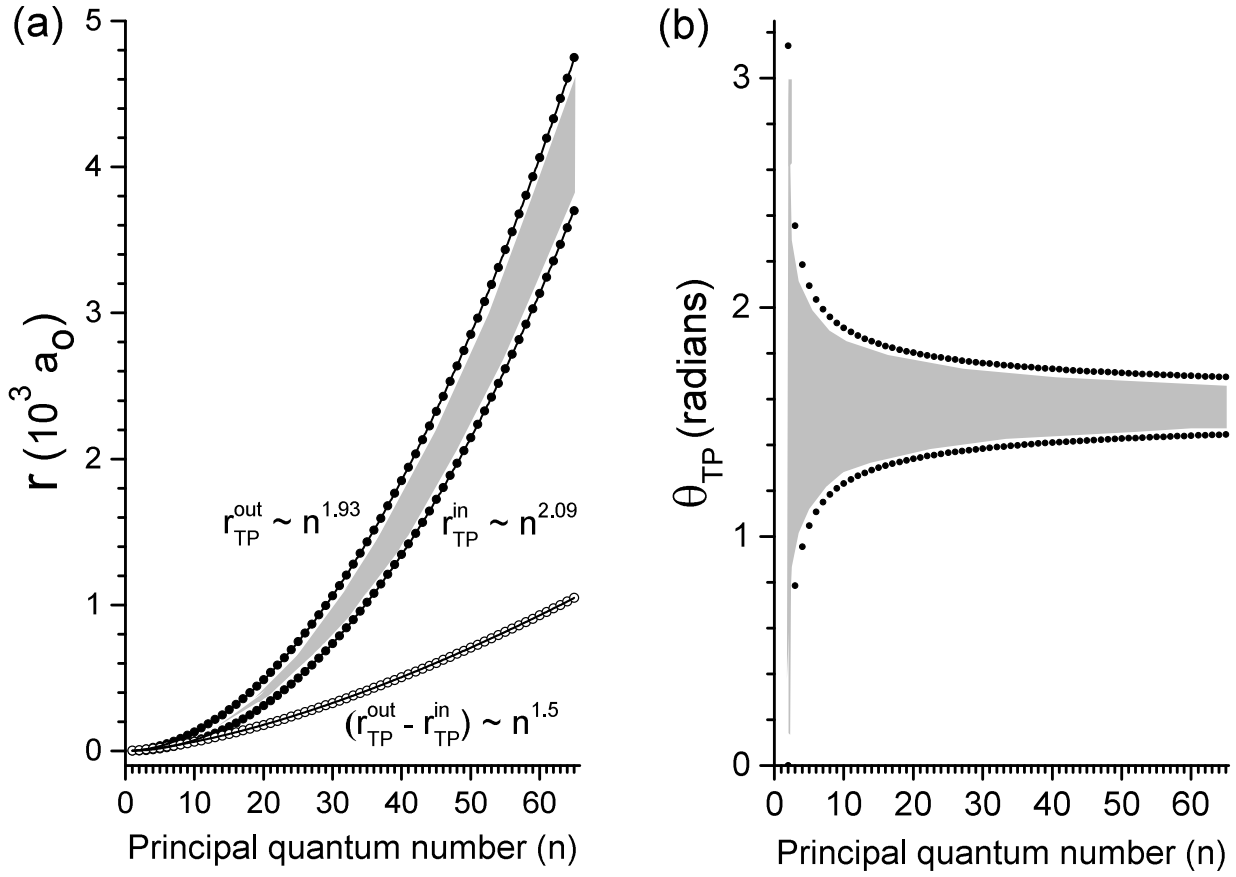

Figure 6.10: Classical turning points for the $|n, \ell = m = n-1\rangle$ circular state as a function of principal quantum number n. (a) Inner and outer classical turning points of the radial wave function $\mathrm{R}_{n\ell}(r)$ (black circles) and their difference (hollow circles). The n-dependence of each is obtained by an allometric fit (solid lines) and are indicated on the plot. (b) Classical turning points of the angular wave function $\mathrm{Y}_{\ell m}(\theta, \phi)$ (black circles). In both (a) and (b) the classically-allowed region is shaded in gray.

Cross sections

Collision cross sections are calculated from Eq. 6.4 by evaluating the electron probability

density of the CS wave function from Eq. 2.2 in the classically allowed regions defined by Eqs. 6.7, 6.8, and 6.10 on a $200 \times 200 \times 200$ grid and numerically integrating its projection onto the xy plane (i.e. σ_{eff}) over all θ. Figure 6.11 shows the calculated CS-ground atom cross sections over a range of n. The geometric cross sections given by $n^4 a_0^2$ are also plotted for reference. An allometric fit to the CS cross sections gives a scaling of $\sim n^{7/2}$, consistent with the area projection of the CS wave function as a torus with radius $\sim$n^2 and width $\sim$n$^{3/2}$.

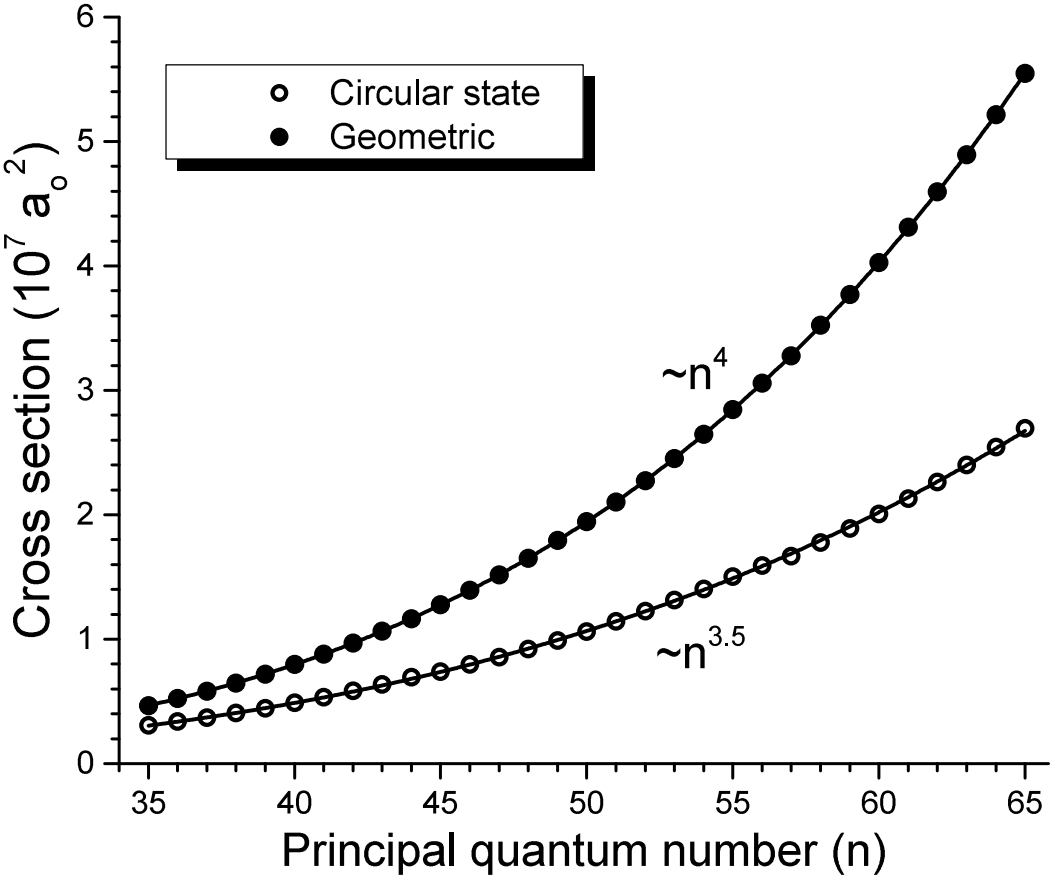

Figure 6.11: Cross sections for the $|n, \ell = m = n-1\rangle$ circular-state (hollow circles) as a function of principal quantum number n. The corresponding geometric cross sections are also plotted (solid circles). The n-dependence of the cross sections are obtained by allometric fits (solid lines) and indicated on the plot.

Here we obtain a collision cross section for the $n = 57$ circular Rydberg and ground-state atom of $\sigma = 1.7 \times 10^7\ a_0^2$. Taking into account the density of the ground-state atom sample used in the experiment $n \approx 10^{10}$ cm^{-3} and the average collision velocity of the two

atoms during the circular state atom's oscillation through the ground-state atom sample $\overline{v} \approx 50\ cm/s$, we find a collision rate $\gamma = n\sigma\overline{v} \approx 300\ s^{-1}$.[3] This agrees qualitatively with the loss rate estimated from the data in Fig. 6.8c and cross sections extrapolated from [56]. Considering the inherent limitation of this classical model to account for quantum effects in the low-energy collision between the two atoms, this close agreement between the calculated cross section and experimental observations is quite remarkable and suggestive of the quasi-classical nature of Rydberg atoms.

6.7 Internal-state evolution in a 300 K thermal radiation background

Given the influence of the internal-state dynamics on the trapping behavior, the internal-state evolution is probed in the experiment by performing state-selective field ionization (SSFI) on the trapped Rydberg atom sample. The near-linear SSFI ramp shown in Fig. 6.12a is applied reaching a field of >120 V/cm over the course of 50 μs (slew rate $\gtrsim$ 2.4 V/cm/μs). Different Rydberg states ionize at different points on the ramp, and can be distinguished by arrival time at the detector. Figure 6.12a shows SSFI traces for excitation to region III in Fig. 6.6, where only $60P_{1/2}$ atoms are excited. In this case, the electric field ramp in the circularization procedure fails to populate any atoms in the CS; all atoms remain in $60P_{1/2}$. Figure 6.12b shows SSFI traces for excitation to region I in Fig. 6.6, where the CS generation procedure is expected to circularize most of the atoms. In both cases we obtain SSFI traces for t_d=0 and 1 ms (thin and thick traces in Fig. 6.12, respectively). First, the total ion signal for both cases is compared by integrating the SSFI curves. Excitation to region I produces a long-lived signal (0.59 remaining fraction), while excitation to III does not (0.09 remaining fraction). This reaffirms the high yield of long-lived CS atoms.

[3]Here $\overline{v} = \sqrt{\overline{v}_{CS}^2 + \overline{v}_{GS}^2}$, where $\overline{v}_{CS} = 0.5$ m/s is the circular-state atom velocity obtained from the data in Fig. 6.8a and $\overline{v}_{GS} = 0.14$ m/s is the most probable velocity in a 100 μK ^{87}Rb atom sample.

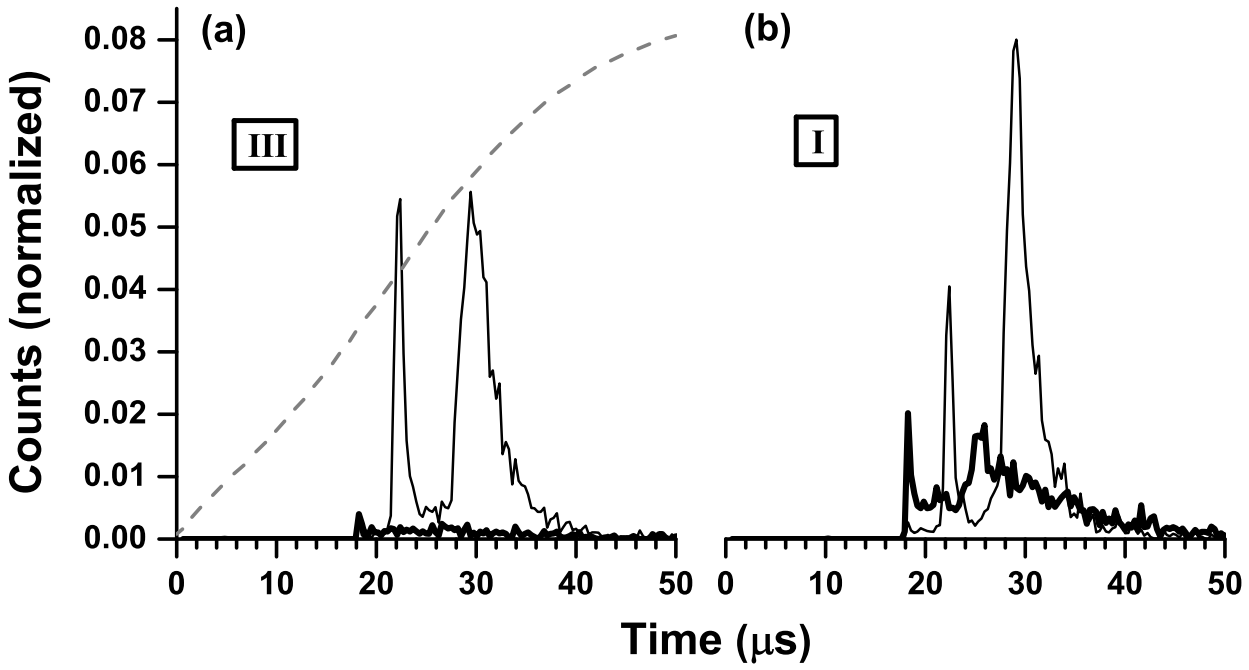

Figure 6.12: SSFI traces for an initial excitation into two different regions in Fig. 6.6: (a) into III, the $60P_{1/2}$ state and (b) into I, the first anti-crossing at the 60P-manifold intersection to generate the CS after the circularization procedure. In both (a) and (b) the thin and thick traces correspond to t_d=0 and 1 ms, respectively. Each trace is a sum of 2×10^4 experiments. The data are normalized such that for t_d=0 ms the curves integrate to the same value. The dashed curve in (a) shows the field-ionization ramp used in both experiments.

Next the structures of the SSFI curves are compared. In both Fig. 6.12a and b at t_d=0, there are two distinct peaks: an early (22 μs) peak, attributed to adiabatic field-ionization events that occur at lower electric fields, and a later (29 μs) diabatic, high-field-ionizing peak [56, 113]. Observation of both adiabatic and diabatic field ionization signals is not unexpected given the SSFI ramp used here has a slew rate that is not much higher than that of the adiabatic field ramp used to produce the circular states. In Fig. 6.12b, the diabatic peak for t_d=1 ms arrives earlier than for t_d=0 ms, and is substantially broadened. This indicates a reduced average ionization field for the trapped sample at later times (corresponding to a higher average n) and rapid state diffusion, respectively. Here, an additional peak emerges at an even earlier arrival time (18 μs). This peak is attributed to atoms accumulating in extremely high-n Rydberg states which ionize at much lower electric fields. The trends in

Fig. 6.12 are in qualitative agreement with our simulations, which also show a thermally-driven redistribution of population to longer-lived, very high-n states. For experimental reasons the field ionization is performed in crossed electric and magnetic fields, which further complicates the field ionization behavior. A detailed modeling of the SSFI curves in Fig. 6.12 is beyond the scope of this work. To gain more insight into the internal-state evolution of the magnetically-trapped cold CS atoms in the 300 K environment, one would want to experimentally distinguish between adiabatic and diabatic ionization events. This could be achieved by applying a fast field-ionization pulse to ensure only diabatic ionization events and varying the peak ionization field to selectively ionize Rydberg states of different n. By recording the ion signal as a function of maximum ionization field for each time delay one could map out the evolution of the n-distribution in the sample over time. In principle, m-selectivity could also be achieved with a Stern-Gerlach-type measurement by switching on an inhomogeneous magnetic field prior to field ionization. This would separate the m components which could be spatially resolved at the MCP upon ionization and extraction, from which their relative signal strengths could be obtained. These state-selective trap diagnostics could provide a tool for studying high-ℓ and circular Rydberg atom low-energy collisional processes, which might manifest as deviations of the measured state distributions from the expected thermally-driven n and m distributions.

6.8 Summary

In this chapter I described the experimental realization of a room-temperature magnetic trap for cold CS Rydberg atoms. The circular states were produced out of a cold atom sample using the adiabatic crossed-fields method, a method generally well-suited for localized CS generation in magnetically-trapped ground-state atom samples due to the high spatial resolution afforded by the optical excitation and the presence of the local magnetic trapping field. The circular state trap oscillation frequency and trapping time were measured and found to be in excellent agreement with predicted values and detailed simulations. The

internal-state evolution of the atom sample was probed, showing the effect of the 300 K black body radiation background on the n distribution in the trap. The method described and demonstrated here to produce and trap cold circular Rydberg atoms provides a means to perform low-temperature studies with Rydberg atoms in high-angular-momentum states. This trapping method could, for example, be employed in a 4 K cryogenic environment to suppress thermal transitions and provide a source of long-lived CS atoms for precision measurements [45, 46], which is of direct relevance to on-going efforts toward a new precision measurement of the Rydberg constant using high-n circular Rydberg atoms [48]. Low-energy interactions involving high-ℓ Rydberg states could also be investigated, for which interaction and collision processes are still unexplored. The highly anisotropic collision cross sections expected for thermal circular Rydberg atoms [**?**] could be studied at low temperature. At sufficiently high ground-state atom density, high-ℓ long-range Rydberg molecules [4] may also be produced in the generation of the CS. Due to their increased mass, these molecules might manifest as trailing signals in the COM oscillations of the CS in a magnetic trap such as the one described above.

CHAPTER VII

Conclusion

In the first part of this dissertation I experimentally and theoretically investigated the influence of angular momentum and angular-momentum couplings on the properties of long-range $^{87}Rb_2$ D-type Rydberg molecules. Due to their relatively recent discovery, experimental work on long-range Rydberg molecules is still in its infancy. To date only homonuclear Rydberg molecules have been studied (and only in Rb and Cs). Diatomic Rydberg molecules formed between non-alkali atoms could be investigated. The nature of the scattering-induced binding interaction also lends itself to the study of larger, more complex molecules. The interaction of a Rydberg electron with a polar molecule, for example, has been predicted to give rise to dipolar polyatomic long-range Rydberg molecules [114].

In the second part of this dissertation I described a technique for producing and trapping cold circular Rydberg atoms. The technique provides a means to perform low-temperature experiments with circular Rydberg atoms. Using this method one could study low-energy interactions involving high-angular-momentum Rydberg atoms, for which interaction processes and collision dynamics are still unknown. The proposed benefit of using high-ℓ and circular Rydberg atoms in quantum information relies on the long radiative lifetimes of these states [50]. In practice, collisions can limit the Rydberg lifetime thereby eliminating the benefit provided by these long-lived states. Systematic studies of collision-induced decoherence could be performed which may lend insight into how one might mitigate these effects.

APPENDICES

APPENDIX A

Angular momentum

In this Appendix I review the quantum treatment of angular momentum and the addition of angular momenta.

A.1 Angular momentum

The quantum formalism for angular momentum applies to both orbital angular momentum and spin, with the distinction that the orbital angular momentum of a particle is restricted to integer values of $\hbar$, which is a consequence of the uniqueness of the angular wave functions (see Eq. 2.5 and discussion in section 2.1), while its spin takes on either integer or half integer values of $\hbar$. The quantum operator for a general angular momentum $\hat{\mathbf{J}}$ is a vector whose components $(\hat{J}_x, \hat{J}_y, \hat{J}_z)$ obey the commutation relations

$$[\hat{J}_x, \hat{J}_y] = i\hbar\hat{J}_z, \qquad [\hat{J}_z, \hat{J}_x] = i\hbar\hat{J}_y, \qquad [\hat{J}_y, \hat{J}_z] = i\hbar\hat{J}_x. \tag{A.1}$$

From these it follows, as a consequence of an uncertainty relation for angular momentum, that any two components are incompatible observables and cannot be measured simultaneously (excluding the special case where $\hat{J}_x = \hat{J}_y = \hat{J}_z = 0$). From the relations in Eq. A.1 one can construct an operator for the magnitude of the angular momentum as $\hat{\mathbf{J}}^2 = \hat{J}_x^2 + \hat{J}_y^2 + \hat{J}_z^2$,

which commutes with all three components ($[\hat{J}_i, \hat{\mathbf{J}}^2] = 0$ for $i = x, y, z$). For a quantum state $|j, m\rangle$ with angular momentum quantum number j and its projection m along a chosen quantization axis, we then have

$$\hat{\mathbf{J}}^2|j, m\rangle = \hbar^2 j(j+1)|j, m\rangle, \tag{A.2}$$

where for each value of j there are $2j + 1$ possible projections $m = -j, -j+1, ..., j-1, j$. Choosing the quantization axis to be along z, each m is then an eigenvalue of the $\hat{J}_z$ operator

$$\hat{\mathbf{J}}_z|j, m\rangle = \hbar m|j, m\rangle. \tag{A.3}$$

For two particles with angular momenta $\hat{\mathbf{J}}_1$ and $\hat{\mathbf{J}}_2$, each obeying the commutation relations in Eq. A.1, the total angular momentum of the system is given by their sum $\hat{\mathbf{J}} = \hat{\mathbf{J}}_1 + \hat{\mathbf{J}}_2$, which also obeys the commutation relations in Eqs. A.1. Writing $\hat{\mathbf{J}}^2$ we then have

$$\hat{\mathbf{J}}^2 = (\hat{\mathbf{J}}_1 + \hat{\mathbf{J}}_2)^2 = \hat{\mathbf{J}}_1^2 + \hat{\mathbf{J}}_2^2 + 2\hat{\mathbf{J}}_1 \otimes \hat{\mathbf{J}}_2, \tag{A.4}$$

which commutes with the squares of the individual angular momenta ($[\hat{\mathbf{J}}^2, \hat{\mathbf{J}}_1^2] = [\hat{\mathbf{J}}^2, \hat{\mathbf{J}}_2^2] = 0$) as does its projection $\hat{J}_z$ ($[\hat{J}_z, \hat{\mathbf{J}}_1^2] = [\hat{J}_z, \hat{\mathbf{J}}_2^2] = 0$). For the combined two-particle system, $\hat{\mathbf{J}}^2$ and $\hat{\mathbf{J}}_z$ then have eigenvalues $\hbar^2 j(j+1)$ and $\hbar m$, respectively, as in Eqs. A.2 and A.3, where here j and m are the quantum numbers for the system's total angular momentum and its projection.

It follows that the system of two angular momenta can be described in either one of two basis representations: a composite (uncoupled) basis $|j_1, m_1\rangle|j_2, m_2\rangle$ or a combined (coupled) basis $|j, m\rangle$. The combined basis can be written as a linear combination of composite basis states as

$$|j, m_j\rangle = \sum_{m_1+m_2=m_j} C_{j_1,j_2,j}^{m_1,m_2,m_j} |j_1, m_1\rangle|j_2, m_2\rangle, \tag{A.5}$$

forming a complete orthonormal set with $(2j_1 + 1) \times (2j_2 + 1)$ states, where the weighting

factors are the Clebsch-Gordon coefficients $C^{m_1,m_2,m_j}_{j_1,j_2,j} = \langle j_1, m_1, j_2, m_2 | j, m_j \rangle = C = C^*$, which are non-zero for $m_1 + m_2 = m_j$ and satisfy

$$\sum_{m_1,m_2} C'^* C = \langle j', m_{j'} | j, m_j \rangle = \delta_{j',j} \delta_{m_{j'},m_j}. \tag{A.6}$$

APPENDIX B

Spin operators in the Fermi model for long-range Rydberg molecules

In this Appendix I derive the triplet and singlet spin projectors in the Hamiltonian of Eq. 5.1 in Chapters IV and II that account for the spin-dependent scattering channels in the interaction between the Rydberg electron and $5S_{1/2}$ electron of the ground-state atom.

B.1 Spin projectors

In this section we are interested in the coupling of electron spins in the scattering interaction between a Rydberg electron and the $5S_{1/2}$ electron in a ground-state rubidium atom. In this two-electron system each electron is described by a spin wave function $|s_i, m_{s_i}\rangle$, where $s_i = 1/2$ is its spin and $m_i = \pm 1/2$ is its projection (spin up $|\uparrow\rangle$ or spin down $|\downarrow\rangle$) along a chosen quantization axis. We can form the composite basis set for the two-electron system as $\{|s_1, m_{s1}\rangle|s_1, m_{s2}\rangle\} = \{|s_1, m_{s1}\rangle \otimes |s_2, m_{s2}\rangle\}$, where the Rydberg electron and $5S_{1/2}$ electron are denoted by subscripts 1 and 2, respectively. Following section A.1, the combined spin state of the system with total spin s and projection m_s along the quantization axis is expressed as

$$|s, m_s\rangle = \sum_{m_{s1}+m_{s2}=m_s} C_{s_1,s_2,s}^{m_{s1},m_{s2},m_s} |s, m_{s1}\rangle|s, m_{s2}\rangle, \tag{B.1}$$

forming a complete set with $(2s_1+1)\times(2s_2+1)=4$ states. Here, the Clebsch-Gordon coefficients are only non-zero for $m_{s1}+m_{s2}=m_s$ and satisfy

$$\sum_{m_{s1},m_{s2}} C'^{*}C = \delta_{s',s}\delta_{m_{s'},m_s}. \tag{B.2}$$

This basis set spans a four-dimensional space consisting of a triplet with $s=1$ and a singlet with $s=0$

$$\left.\begin{aligned} |1,\ 1\rangle &= |\uparrow\uparrow\rangle \\ |1,\ 0\rangle &= \frac{1}{\sqrt{2}}(|\uparrow\downarrow\rangle + |\downarrow\uparrow\rangle) \\ |1,-1\rangle &= |\downarrow\downarrow\rangle \end{aligned}\right\} \quad \text{s=1} \tag{B.3}$$

$$\left.|0,\ 0\rangle = \frac{1}{\sqrt{2}}(|\uparrow\downarrow\rangle - |\downarrow\uparrow\rangle).\right\} \quad \text{s=0} \tag{B.4}$$

The delta-function interaction terms in the Hamiltonian in Eq. 5.1 conserve the total electron spin of the system and its projection according to Eq. B.2, and the singlet and triplet scattering channels each have their associated l- and energy-dependent scattering phase shifts δ_l. To account for the spin-dependent scattering channels we generate singlet (S) and triplet (T) spin projectors $\hat{\mathbb{I}}_{(S,T)}$ to selectively enable the corresponding scattering interaction terms in the Hamiltonian. Considering first the single spin operators $\hat{\mathbf{S}}_1$ and $\hat{\mathbf{S}}_2$ for the Rydberg electron and $5S_{1/2}$ electron, respectively, we can write the total spin measurement operator as $\hat{\mathbf{S}}^2 = (\hat{\mathbf{S}}_1+\hat{\mathbf{S}}_2)^2 = \hat{\mathbf{S}}_1^2+\hat{\mathbf{S}}_2^2+2\hat{\mathbf{S}}_1\otimes\hat{\mathbf{S}}_2$. Rearranging into the more convenient form $\hat{\mathbf{S}}_1\otimes\hat{\mathbf{S}}_2 = \frac{1}{2}(\hat{\mathbf{S}}^2-\hat{\mathbf{S}}_1^2-\hat{\mathbf{S}}_2^2)$ and applying this operator to the combined spin state of the system $|s,m_s\rangle$ gives

$$\hat{\mathbf{S}}_1\otimes\hat{\mathbf{S}}_2|s,m_s\rangle = \frac{\hbar^2}{2}(s(s+1)-\frac{3}{4})|s,m_s\rangle = \begin{cases} +\frac{1}{4}\hbar^2|s,m_s\rangle & \text{for } s=1 \text{ (triplet)} \\ -\frac{3}{4}\hbar^2|s,m_s\rangle & \text{for } s=0 \text{ (singlet)} \end{cases} \tag{B.5}$$

where following Eq. A.2 we have used $\hat{\mathbf{S}}_i^2|s_i,m_{si}\rangle = \hbar^2 s_i(s_i+1)|s_i,m_{si}\rangle$ for a spin system i.

The operator $\hat{\mathbf{S}}_1 \otimes \hat{\mathbf{S}}_2$ can be expressed in matrix form using

$$\hat{\mathbf{S}}_1 \otimes \hat{\mathbf{S}}_2 = \hat{\mathbf{S}}_{1z}\hat{\mathbf{S}}_{2z} + \frac{1}{2}(\hat{\mathbf{S}}_{1+}\hat{\mathbf{S}}_{2-} + \hat{\mathbf{S}}_{1-}\hat{\mathbf{S}}_{2+}), \tag{B.6}$$

where the z-component spin operator $\hat{\mathbf{S}}_{iz}$ for each electron $i = 1, 2$ satisfies

$$\hat{\mathbf{S}}_{iz}|s_i, m_{si}\rangle = \hbar m_{si}|s_i, m_{si}\rangle, \tag{B.7}$$

and $\hat{\mathbf{S}}_{i\pm}$ are the raising and lowering operators defined as

$$\hat{\mathbf{S}}_{i\pm}|s_i, m_{si}\rangle = \hbar\sqrt{(s_i \mp m_{si})(s_i \pm m_{si} + 1)}|s_i, m_{si} \pm 1\rangle. \tag{B.8}$$

Evaluating Eq. B.6 in the composite basis we then obtain

$$|\uparrow\uparrow\rangle\,|\uparrow\downarrow\rangle\,|\downarrow\uparrow\rangle\,|\downarrow\downarrow\rangle \tag{B.9}$$

$$\hat{\mathbf{S}}_1 \otimes \hat{\mathbf{S}}_2 = \hbar^2 \begin{pmatrix} \frac{1}{4} & 0 & 0 & 0 \\ 0 & -\frac{1}{4} & \frac{1}{2} & 0 \\ 0 & \frac{1}{2} & -\frac{1}{4} & 0 \\ 0 & 0 & 0 & \frac{1}{4} \end{pmatrix} \tag{B.10}$$

which has eigenvalues $+\frac{1}{4}\hbar^2$ $(3\times)$ and $-\frac{3}{4}\hbar^2$ $(1\times)$, consistent with Eq. B.5. With this, the triplet projector is defined as $\hat{\mathbb{I}}_T = \hat{\mathbf{S}}_1 \otimes \hat{\mathbf{S}}_2 + \frac{3}{4}\hbar^2 \cdot \hat{\mathbb{I}}$, where $\hat{\mathbb{I}}$ is the identity operator. In matrix form this is

$$\hat{\mathbb{I}}_T = \hbar^2 \begin{pmatrix} 1 & 0 & 0 & 0 \\ 0 & \frac{1}{2} & \frac{1}{2} & 0 \\ 0 & \frac{1}{2} & \frac{1}{2} & 0 \\ 0 & 0 & 0 & 1 \end{pmatrix} \tag{B.11}$$

which has an eigenvalue of $\hbar^2$ (zero) for the triplet (singlet) states. Similarly, the singlet projector is defined as $\hat{\mathbb{I}}_S = \hat{\mathbb{I}} - \hat{\mathbb{I}}_T = -\hat{\mathbf{S}}_1 \otimes \hat{\mathbf{S}}_2 + \frac{1}{4} \cdot \hat{\mathbb{I}}$, written in matrix form as

$$\hat{\mathbb{I}}_S = \hbar^2 \begin{pmatrix} 0 & 0 & 0 & 0 \\ 0 & \frac{1}{2} & -\frac{1}{2} & 0 \\ 0 & -\frac{1}{2} & \frac{1}{2} & 0 \\ 0 & 0 & 0 & 0 \end{pmatrix} \tag{B.12}$$

which conversely has an eigenvalue of $\hbar^2$ (zero) for the singlet (triplet) states. Note that the Hamiltonians in chapters IVand V and these spin projection operators therein are written in atomic units where $\hbar = 1$.

APPENDIX C

Two-photon optical excitation rates of hydrogenic Stark states in the adiabatic crossed-fields method

In this Appendix I describe the calculation of two-photon excitation rates of linear Stark states for the production of circular Rydberg atoms using the adiabatic crossed-fields method described in Chapter VI.

C.1 Two-photon optical excitation rates of linear Stark states

If the initial population of a quantum system is in a well-defined ground state $|i\rangle$ and the optical excitation is fast compared to the lifetime of the target state $|f\rangle$, we can calculate the transition rate [115] between $|i\rangle$ and $|f\rangle$ using a two-step optical excitation with Fermi's Golden Rule

$$r_i^f = \frac{2\pi}{\hbar}|\langle f|V|i\rangle|^2\delta(E_f - E_i - \hbar\omega_2 - \hbar\omega_1). \tag{C.1}$$

Here, V is the perturbation between $|i\rangle$ and $|f\rangle$ and the Dirac delta function $\delta(E_f - E_i - \hbar\omega_2 - \hbar\omega_1)$ ensures energy conservation, where E_f, E_i, ω_1 and ω_2 are the final-state energy, initial state energy and first and second laser frequencies, respectively. Since $|f\rangle$ is part of a continuum of states (finite target-state lifetimes and spectral width of lasers) we weigh the

transition rate by a density of states $\rho(\Delta E)$, where $\Delta E = E' - E - \hbar\omega_2 - \hbar\omega_1$, and integrate over all ΔE:

$$\begin{aligned} R_i^f &= \int_{-\infty}^{\infty} r_i^f(\Delta E)\rho(\Delta E)\mathrm{d}\Delta E \\ &= \frac{2\pi}{\hbar}|\langle f|V|i\rangle|^2\rho(\Delta E) \end{aligned} \tag{C.2}$$

This transition rate is in units of s^{-1}. We are concerned with the transition rate for an off-resonant two-photon excitation from $|i\rangle$ to $|f\rangle$ through all intermediate states $|m\rangle$. To do this we write the perturbation as

$$\langle f|V|i\rangle \rightarrow \frac{1}{4}\sum_m \frac{\langle f|e\vec{E}_2\cdot\vec{r}|m\rangle\langle m|e\vec{E}_1\cdot\vec{r}|i\rangle}{\delta} \tag{C.3}$$

where $e\vec{E}_1\cdot\vec{r}$ and $e\vec{E}_2\cdot\vec{r}$ are the electric dipole energies of the first and second step in the excitation, respectively, and δ is the detuning from the intermediate states in units of energy. Note that in (C.3) we calculate a coherent sum over all m because we are concerned with a two-photon transition that is significantly off-resonance from the intermediate state $|m\rangle$ ($\delta > \hbar\Gamma_m$, where Γ_m is the linewidth of state $|m\rangle$). Denoting the Rabi frequencies in terms of the matrix elements as

$$\Omega_{fm} = \frac{\langle f|e\vec{E}_2\cdot\vec{r}|m\rangle}{\hbar} \tag{C.4}$$

and

$$\Omega_{mi} = \frac{\langle m|e\vec{E}_1\cdot\vec{r}|i\rangle}{\hbar} \tag{C.5}$$

in units of rads/second and taking the δ outside of the sum in (3) (which is a valid approximation as long as the external fields are not large enough to cause significant energy shifts of the m_j sub-levels of the intermediate $|m\rangle$ states) we write the full transition rate as

$$R_i^f = \frac{2\pi\hbar^3}{16\delta^2}|\sum_m \Omega_{fm}\Omega_{mi}|^2\rho(\Delta E). \tag{C.6}$$

The spectral width of the excitation lasers is typically much larger than the linewidth of target Rydberg states so we model the density of states by a Gaussian distribution (this is consistent with experimentally observed Rydberg lines):

$$\rho(\Delta E) = \frac{\sqrt{8\ln 2}}{\sqrt{2\pi}\nu h} \exp^{-\Delta E^2/2\sigma^2} \tag{C.7}$$

with $\sigma = \frac{h\nu}{\sqrt{8\ln 2}}$, where ν is the FWHM of the experimentally determined Rydberg line in units of Hz, and satisfying the normalization condition

$$\int_{-\infty}^{\infty} \rho(\Delta E) \mathrm{d}\Delta E = 1. \tag{C.8}$$

Inserting (C.7) into (C.6) we obtain

$$R_i^f = \frac{\pi\hbar^3}{8\delta^2} |\sum_m \Omega_{fm}\Omega_{mi}|^2 \frac{\sqrt{8\ln 2}}{\sqrt{2\pi}\nu h} \exp^{-\Delta E^2/2\sigma^2}. \tag{C.9}$$

Next, we calculate the two-photon matrix elements for the transition $5S_{1/2} \rightarrow 5P_{3/2} \rightarrow |R>$. We write the target Rydberg state as

$$|f\rangle = \sum_{n,\ell,j,m_j} C_{n,\ell,j,m_j} |n,\ell,j,m_j\rangle \tag{C.10}$$

Where C_{n,ℓ,j,m_j} is the complex amplitude for a state $|n,\ell,j,m_j\rangle$ with principal quantum number n, orbital quantum number ℓ, total angular momentum j and magnetic quantum number m_j. We then write the $5S_{1/2}$ ground-state with its two possible spin components ($-\frac{1}{2}$ and $\frac{1}{2}$) as

$$|i\rangle = \sum_{j=\frac{1}{2}, m_j=-\frac{1}{2},\frac{1}{2}} C_{5,S,j,m_j} |5,S,j,m_j\rangle \tag{C.11}$$

and the intermediate $5P_{3/2}$ state as

$$|m\rangle = \sum_{j=\frac{3}{2},m_j} C_{5,P,j,m_j}|5,P,j,m_j\rangle \tag{C.12}$$

where the sum is over all intermediate m_j projections of the $j = 3/2$ state. We describe the laser fields with linear polarization vectors $(x,y,z) = x\hat{x} + y\hat{y} + z\hat{z}$ and amplitudes E_1 and E_2. To simplify the evaluation of the matrix elements (C.4) and (C.5), we perform the transformation $(x,y,z) \rightarrow \frac{1}{2}(x-iy)\hat{S}_+ + \frac{1}{2}(x+iy)\hat{S}_- + z\hat{S}_z$, with $\hat{S}_+, \hat{S}_-$ and $\hat{S}_z$ [ref p.253 of Bethe and Salpeter], and define $(x,y,z) = \sum_a \hat{S}_a f_a$, where $a \in [+,-,z]$ and $f_+ = \frac{1}{2}(x-iy), f_- = \frac{1}{2}(x+iy), f_z = z$. The operators for steps 1 and 2 then become

$$E_1 \sum_a \hat{S}_a f_{a,1} \tag{C.13}$$

and

$$E_2 \sum_a \hat{S}_a f_{a,2}. \tag{C.14}$$

Putting this all together the two-photon matrix elements become

$$\begin{aligned} &\sum_m \Omega_{fm}\Omega_{mi} = \\ &\qquad (\frac{ea_0}{\hbar})^2 E_1 E_2 \sum_{n,\ell,j,m_j} C^*_{n,\ell,j,m_j}\Lambda_{n,\ell,j,m_j} \end{aligned} \tag{C.15}$$

where a_0 is the Bohr radius, C^*_{n,ℓ,j,m_j} are the Rydberg-state amplitudes of state $|f\rangle$, and

$$\begin{aligned} \Lambda_{n,\ell,j,m_j} = &\\ &\langle n,\ell,j,m_j| \sum_{a,b,j,m_j} \hat{S}_a f_{a,2}|5,P,j,m_j\rangle \times \\ &\langle 5,P,j,m_j|\hat{S}_b f_{b,1} \times \\ &\sum_{j=\frac{1}{2},m_j=-\frac{1}{2},\frac{1}{2}} C_{5,S,m_j,m_j}|5,S,m_j,m_j\rangle. \end{aligned} \tag{C.16}$$

Note that Λ_{n,ℓ,j,m_j} is a single value for a set of laser fields, polarizations and ground-state wave function.

In this work, we consider dipole-allowed transitions ($\Delta m = 0, \pm 1$) in rubidium. The diagrams in Fig. C.1 show all transitions from the $5S_{1/2}$ ground state to a Rydberg state with positive m_j through the intermediate $5P_{3/2}$ states. Generally, the ground state is in a superposition of $|\uparrow\rangle$ and $|\downarrow\rangle$, resulting in a total of $2 \times (1 + 3 + 5) = 18$ terms interfering in the sums of equation (C.16). The factor of 2 comes from including the transitions to negative m_j Rydberg states, which are not shown in Fig. C.1.

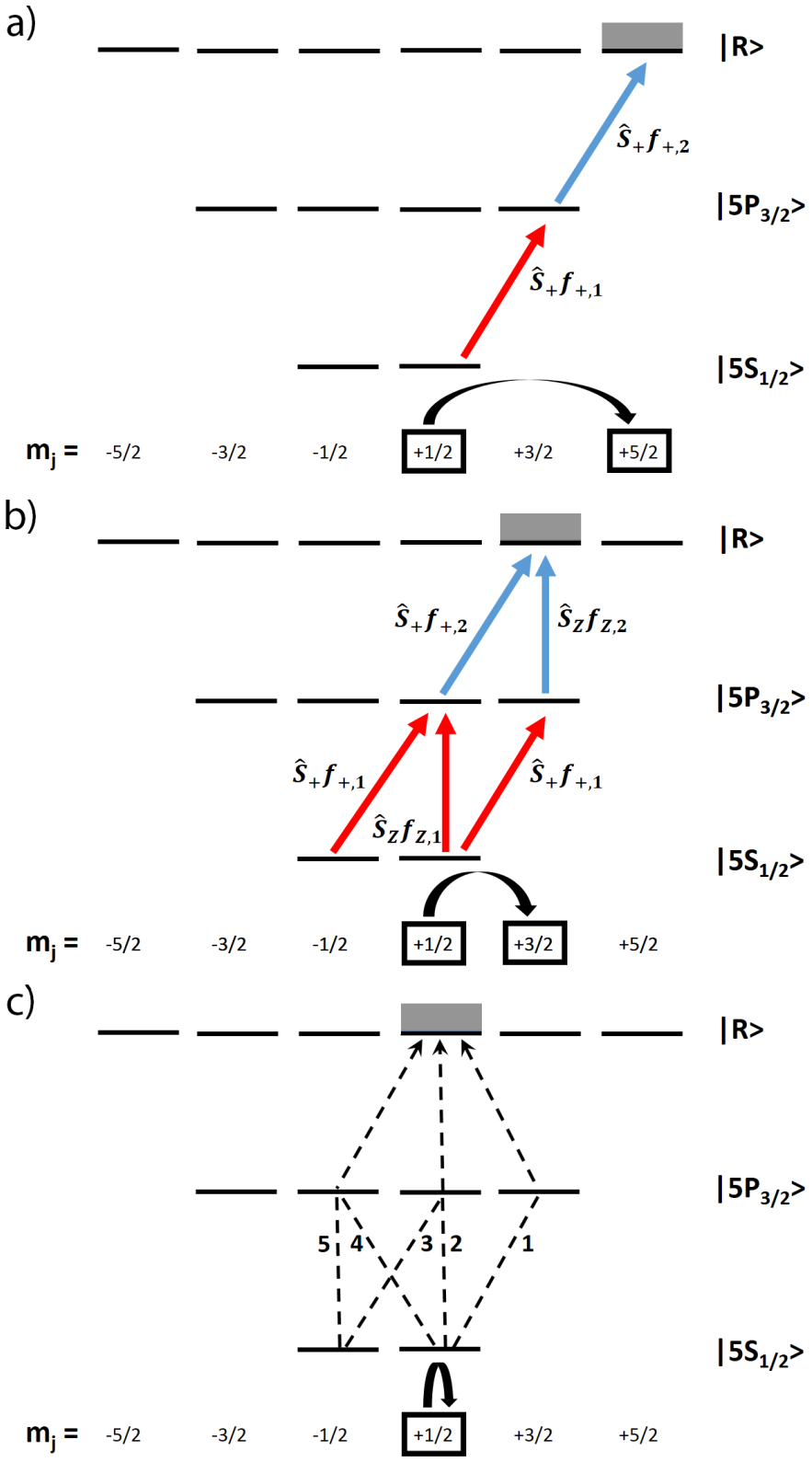

Figure C.1: (color online). Dipole-allowed, two-photon transitions from the $5S_{1/2}$ ground state to all positive m Rydberg states through the intermediate $5P_{3/2}$ state. Dipole operators are labeled. Transitions from the well-defined, $5S_{1/2}$ $m = +1/2$ ground-state to (a) $m_j = +2.5$, (b) $m_j = +1.5$ and (c) $m_j = +0.5$ Rydberg states are indicated.

BIBLIOGRAPHY

BIBLIOGRAPHY

[1] A. A. Khuskivadze, M. I. Chibisov, and I. I. Fabrikant. Adiabatic energy levels and electric dipole moments of rydberg states of rb_2 and cs_2 dimers. *Phys. Rev. A*, 66: 042709, Oct 2002. doi: 10.1103/PhysRevA.66.042709. URL `http://link.aps.org/doi/10.1103/PhysRevA.66.042709`.

[2] Rachel Elizabeth Sapiro. *Bose-Einstein Condensate Experiments in Optical Lattices*. PhD thesis, University of Michigan, 2010.

[3] Daniel A. Steck. Rubidium 87 d line data. `http://steck.us/alkalidata/rubidium87numbers.pdf`, 2010. [Online; accessed 2014-11-18].

[4] Chris H. Greene, A. S. Dickinson, and H. R. Sadeghpour. Creation of polar and nonpolar ultra-long-range rydberg molecules. *Phys. Rev. Lett.*, 85:2458–2461, Sep 2000. doi: 10.1103/PhysRevLett.85.2458. URL `http://link.aps.org/doi/10.1103/PhysRevLett.85.2458`.

[5] D. Delande and J. C. Gay. A new method for producing circular rydberg states. *EPL (Europhysics Letters)*, 5(4):303, 1988. URL `http://stacks.iop.org/0295-5075/5/i=4/a=004`.

[6] Ernest Rutherford. The scattering of α and β particles by matter and the structure of the atom. *Philosophical Magazine*, 21:669–688, 1911.

[7] Niels Bohr. On the constitution of atoms and molecules. *Philosophical Magazine*, 26: 161–233, July 1913.

[8] Walther Gerlach and Otto Stern. Das magnetische moment des silberatoms. *Zeitschrift für Physik*, 9:353–355, 1922.

[9] E. Amaldi and E. Segrè. Effetto della pressione sui termini elevati degli alcalini. *Il Nuovo Cimento*, 11(3):145–156, 1934. ISSN 0029-6341. doi: 10.1007/BF02959828. URL `http://dx.doi.org/10.1007/BF02959828`.

[10] Enrico Fermi. Sopra lo spostamento per pressione delle righe elevate delle serie spettrali. *Il Nuovo Cimento*, 11(3):157–166, 1934. ISSN 0029-6341. doi: 10.1007/BF02959829. URL `http://dx.doi.org/10.1007/BF02959829`.

[11] Shang-yi Ch'en and Makoto Takeo. Broadening and shift of spectral lines due to the presence of foreign gases. *Rev. Mod. Phys.*, 29:20–73, Jan 1957. doi: 10.1103/RevModPhys.29.20. URL `http://link.aps.org/doi/10.1103/RevModPhys.29.20`.

[12] Omont, A. On the theory of collisions of atoms in rydberg states with neutral particles. *J. Phys. France*, 38(11):1343–1359, 1977. doi: 10.1051/jphys:0197700380110134300. URL http://dx.doi.org/10.1051/jphys:0197700380110134300.

[13] T. W. Hänsch. Repetitively pulsed tunable dye laser for high resolution spectroscopy. *Appl. Opt.*, 11(4):895–898, Apr 1972. doi: 10.1364/AO.11.000895. URL http://ao.osa.org/abstract.cfm?URI=ao-11-4-895.

[14] M. H. Anderson, J. R. Ensher, M. R. Matthews, C. E. Wieman, and E. A. Cornell. Observation of bose-einstein condensation in a dilute atomic vapor. *Science*, 269(5221): 198–201, 1995. doi: 10.1126/science.269.5221.198. URL http://www.sciencemag.org/content/269/5221/198.abstract.

[15] K. B. Davis, M. O. Mewes, M. R. Andrews, N. J. van Druten, D. S. Durfee, D. M. Kurn, and W. Ketterle. Bose-einstein condensation in a gas of sodium atoms. *Phys. Rev. Lett.*, 75:3969–3973, Nov 1995. doi: 10.1103/PhysRevLett.75.3969. URL http://link.aps.org/doi/10.1103/PhysRevLett.75.3969.

[16] I I Fabrikant. Interaction of rydberg atoms and thermal electrons with k, rb and cs atoms. *J. Phys. B.*, 19(10):1527, 1986. URL http://stacks.iop.org/0022-3700/19/i=10/a=021.

[17] C. Bahrim and U. Thumm. Low-lying $^3P^o$ and $^3S^e$ states of rb^-, cs^-, and fr^-. *Phys. Rev. A*, 61:022722, Jan 2000. doi: 10.1103/PhysRevA.61.022722. URL http://link.aps.org/doi/10.1103/PhysRevA.61.022722.

[18] C Bahrim, U Thumm, and I I Fabrikant. 3 s e and 1 s e scattering lengths for e - + rb, cs and fr collisions. *Journal of Physics B: Atomic, Molecular and Optical Physics*, 34(6):L195, 2001. URL http://stacks.iop.org/0953-4075/34/i=6/a=107.

[19] Edward L Hamilton, Chris H Greene, and H R Sadeghpour. Shape-resonance-induced long-range molecular rydberg states. *Journal of Physics B: Atomic, Molecular and Optical Physics*, 35(10):L199, 2002. URL http://stacks.iop.org/0953-4075/35/i=10/a=102.

[20] Vera Bendkowsky, Bjorn Butscher, Johannes Nipper, James P. Shaffer, Robert Löw, and Tilman Pfau. Observation of ultralong-range rydberg molecules. *Nature*, 458: 1005–1008, April 2009. doi: 10.1038/nature07945. URL http://dx.doi.org/10.1038/nature07945.

[21] Kevin M. Jones, Eite Tiesinga, Paul D. Lett, and Paul S. Julienne. Ultracold photoassociation spectroscopy: Long-range molecules and atomic scattering. *Rev. Mod. Phys.*, 78:483–535, May 2006. doi: 10.1103/RevModPhys.78.483. URL http://link.aps.org/doi/10.1103/RevModPhys.78.483.

[22] J. Tallant, S. T. Rittenhouse, D. Booth, H. R. Sadeghpour, and J. P. Shaffer. Observation of blueshifted ultralong-range cs_2 rydberg molecules. *Phys. Rev. Lett.*, 109: 173202, Oct 2012. doi: 10.1103/PhysRevLett.109.173202. URL http://link.aps.org/doi/10.1103/PhysRevLett.109.173202.

[23] Heiner Saßmannshausen, Frédéric Merkt, and Johannes Deiglmayr. Experimental characterization of singlet scattering channels in long-range rydberg molecules. *arXiv:1412.0846*, December 2014. URL http://arxiv.org/abs/1412.0846.

[24] M. A. Bellos, R. Carollo, J. Banerjee, E. E. Eyler, P. L. Gould, and W. C. Stwalley. Excitation of weakly bound molecules to trilobitelike rydberg states. *Phys. Rev. Lett.*, 111:053001, Jul 2013. doi: 10.1103/PhysRevLett.111.053001. URL http://link.aps.org/doi/10.1103/PhysRevLett.111.053001.

[25] D. A. Anderson, S. A. Miller, and G. Raithel. Photoassociation of long-range *nd* rydberg molecules. *Phys. Rev. Lett.*, 112:163201, Apr 2014. doi: 10.1103/PhysRevLett.112.163201. URL http://link.aps.org/doi/10.1103/PhysRevLett.112.163201.

[26] A.T. Krupp, A. Gaj, J.B. Balewski, P. Ilzhöfer, S. Hofferberth, R. Löw, T. Pfau, M. Kurz, and P. Schmelcher. Alignment of *d*-state rydberg molecules. *Phys. Rev. Lett.*, 112:143008, Apr 2014. doi: 10.1103/PhysRevLett.112.143008. URL http://link.aps.org/doi/10.1103/PhysRevLett.112.143008.

[27] Björn Butscher, Johannes Nipper, Jonathan B. Balewski, Ludmila Kukota, Vera Bendkowsky, Robert Löw, and Tilman Pfau. Atom-molecule coherence for ultralong-range rydberg dimers. *Nat. Phys.*, 6:970–974, November 2010. doi: 10.1038/nphys1828. URL http://dx.doi.org/10.1038/nphys1828.

[28] W. Li, T. Pohl, J. M. Rost, Seth T. Rittenhouse, H. R. Sadeghpour, J. Nipper, B. Butscher, J. B. Balewski, V. Bendkowsky, R. Löw, and T. Pfau. A homonuclear molecule with a permanent electric dipole moment. *Science*, 334(6059):1110–1114, 2011. doi: 10.1126/science.1211255. URL http://www.sciencemag.org/content/334/6059/1110.abstract.

[29] V. Bendkowsky, B. Butscher, J. Nipper, J. B. Balewski, J. P. Shaffer, R. Löw, T. Pfau, W. Li, J. Stanojevic, T. Pohl, and J. M. Rost. Rydberg trimers and excited dimers bound by internal quantum reflection. *Phys. Rev. Lett.*, 105:163201, Oct 2010. doi: 10.1103/PhysRevLett.105.163201. URL http://link.aps.org/doi/10.1103/PhysRevLett.105.163201.

[30] Anita Gaj, Alexander T. Krupp, Jonathan B. Balewski, Robert Löw, Sebastian Hofferberth, and Tilman Pfau. From molecular spectra to a density shift in dense rydberg gases. *Nat. Comm.*, 5, August 2014.

[31] Randall G. Hulet and Daniel Kleppner. Rydberg atoms in "circular" states. *Phys. Rev. Lett.*, 51:1430–1433, Oct 1983. doi: 10.1103/PhysRevLett.51.1430. URL http://link.aps.org/doi/10.1103/PhysRevLett.51.1430.

[32] P. Nussenzveig, F. Bernardot, M. Brune, J. Hare, J. M. Raimond, S. Haroche, and W. Gawlik. Preparation of high-principal-quantum-number "circular" states of rubidium. *Phys. Rev. A*, 48:3991–3994, Nov 1993. doi: 10.1103/PhysRevA.48.3991. URL http://link.aps.org/doi/10.1103/PhysRevA.48.3991.

[33] W A Molander, C R Stroud Jr, and J A Yeazell. Excitation of high angular momentum rydberg states. *Journal of Physics B: Atomic and Molecular Physics*, 19(12):L461, 1986. URL http://stacks.iop.org/0022-3700/19/i=12/a=003.

[34] C. H. Cheng, C. Y. Lee, and T. F. Gallagher. Production of circular rydberg states with circularly polarized microwave fields. *Phys. Rev. Lett.*, 73:3078–3081, Dec 1994. doi: 10.1103/PhysRevLett.73.3078. URL http://link.aps.org/doi/10.1103/PhysRevLett.73.3078.

[35] L Chen, M Cheret, F Roussel, and G Spiess. New scheme for producing circular orbital states in combined rf and static fields. *Journal of Physics B: Atomic, Molecular and Optical Physics*, 26(15):L437, 1993. URL http://stacks.iop.org/0953-4075/26/i=15/a=002.

[36] Dominique Delande. *Atomes de Rydberg en champs statiques intenses*. PhD thesis, Université Pierre et Marie Curie - Paris VI, 1988. URL https://tel.archives-ouvertes.fr/file/index/docid/61112/filename/1988DELANDE.pdf.

[37] J. Hare, M. Gross, and P. Goy. Circular atoms prepared by a new method of crossed electric and magnetic fields. *Phys. Rev. Lett.*, 61:1938–1941, Oct 1988. doi: 10.1103/PhysRevLett.61.1938. URL http://link.aps.org/doi/10.1103/PhysRevLett.61.1938.

[38] Randall G. Hulet, Eric S. Hilfer, and Daniel Kleppner. Inhibited spontaneous emission by a rydberg atom. *Phys. Rev. Lett.*, 55:2137–2140, Nov 1985. doi: 10.1103/PhysRevLett.55.2137. URL http://link.aps.org/doi/10.1103/PhysRevLett.55.2137.

[39] M. Brune, E. Hagley, J. Dreyer, X. Mâitre, A. Maali, C. Wunderlich, J. M. Raimond, and S. Haroche. Observing the progressive decoherence of the "meter" in a quantum measurement. *Phys. Rev. Lett.*, 77:4887–4890, Dec 1996. doi: 10.1103/PhysRevLett.77.4887. URL http://link.aps.org/doi/10.1103/PhysRevLett.77.4887.

[40] Serge Haroche. Entanglement, decoherence and the quantum/classical boundary. *Physics Today*, 51, 1998. doi: 10.1063/1.882326. URL http://dx.doi.org/10.1063/1.882326.

[41] J. M. Raimond, M. Brune, and S. Haroche. Manipulating quantum entanglement with atoms and photons in a cavity. *Rev. Mod. Phys.*, 73:565–582, Aug 2001. doi: 10.1103/RevModPhys.73.565. URL http://link.aps.org/doi/10.1103/RevModPhys.73.565.

[42] Serge Haroche and David J. Wineland. The nobel prize in physics 2012. *Nobelprize.org*, 2014. URL http://www.nobelprize.org/nobel_prizes/physics/laureates/2012/.

[43] Serge Haroche. Controlling photons in a box and exploring the quantum to classical boundary. http://www.nobelprize.org/nobel_prizes/physics/laureates/2012/haroche-lecture.pdf, 2012. [Online; accessed 2015-03-10].

[44] Sebastien Gleyzes, Stefan Kuhr, Christine Guerlin, Julien Bernu, Samuel Deleglise, Ulrich Busk Hoff, Michel Brune, Jean-Michel Raimond, and Serge Haroche. Quantum jumps of light recording the birth and death of a photon in a cavity. *Nature*, 446:297–300, March 2007. doi: 10.1038/nature05589. URL http://dx.doi.org/10.1038/nature05589.

[45] J. Hare, A. Nussenzweig, C. Gabbanini, M. Weidemuller, P. Goy, M. Gross, and S. Haroche. Toward a rydberg constant measurement on circular atoms. *Instrumentation and Measurement, IEEE Transactions on*, 42(2):331 –334, april 1993. ISSN 0018-9456. doi: 10.1109/19.278576.

[46] Robert Lutwak, Jeffrey Holley, Pin Peter Chang, Scott Paine, Daniel Kleppner, and Theodore Ducas. Circular states of atomic hydrogen. *Phys. Rev. A*, 56:1443–1452, Aug 1997. doi: 10.1103/PhysRevA.56.1443. URL http://link.aps.org/doi/10.1103/PhysRevA.56.1443.

[47] Joel Christopher De Vries. *A precision millimeter-wave measurement of the Rydberg frequency*. PhD thesis, Massachusetts Institute of Technology, 2002. URL http://hdl.handle.net/1721.1/8292.

[48] Georg Raithel. High-precision microwave spectroscopy of long-lived circular-state rydberg atoms in microgravity. http://www.nasa.gov/content/physical-science-research-proposals-selected-for-cold-atom-laboratory/, 2014. [Online; accessed 2015-01-22].

[49] Kaitlin R. Moore, Sarah E. Anderson, and Georg Raithel. Forbidden atomic transitions driven by an intensity-modulated laser trap. *Nature Communications*, 6, January 2015. doi: 10.1038/ncomms7090. URL http://dx.doi.org/10.1038/ncomms7090.

[50] T. Xia, X. L. Zhang, and M. Saffman. Analysis of a controlled phase gate using circular rydberg states. *Phys. Rev. A*, 88:062337, Dec 2013. doi: 10.1103/PhysRevA.88.062337. URL http://link.aps.org/doi/10.1103/PhysRevA.88.062337.

[51] E. de Prunelé. Orientation effects in thermal collisions between "circular" ˘ rydberg-state atoms and ground-state helium. *Phys. Rev. A*, 31:3593–3602, Jun 1985. doi: 10.1103/PhysRevA.31.3593. URL http://link.aps.org/doi/10.1103/PhysRevA.31.3593.

[52] ElenaS. Mironchuk, AlexanderA. Narits, and VladimirS. Lebedev. Collisional destruction of circular rydberg states by atoms with small electron affinities. *The European Physical Journal D*, 68(12):368, 2014. ISSN 1434-6060. doi: 10.1140/epjd/e2014-50460-4. URL http://dx.doi.org/10.1140/epjd/e2014-50460-4.

[53] D. A. Anderson, A. Schwarzkopf, R. E. Sapiro, and G. Raithel. Production and trapping of cold circular rydberg atoms. *Phys. Rev. A*, 88:031401, Sep 2013. doi: 10.1103/PhysRevA.88.031401. URL http://link.aps.org/doi/10.1103/PhysRevA.88.031401.

[54] Hans A. Bethe and Edwin E. Salpeter. *Quantum mechanics of one- and two-electron atoms*, volume 35. 1957.

[55] L.D. Landau and E.M. Lifshitz. *Quantum Mechanics: Non-relativistic Theory*. 3 edition, 1958.

[56] T.F.Gallagher. *Rydberg Atoms*. Cambridge University Press, New York, NY, USA, 1994.

[57] C. J. Foot. *Atomic Physics*. Oxford University Press, New York, USA, 2005.

[58] Herald Friedrich. *Theoretical Atomic Physics*. Springer, 2006.

[59] Peter Mohr, Barry Taylor, and David Newell. Codata recommended values of the fundamental physical constants: 2010. *Rev. Mod. Phys.*, 84:1527–1605, Nov 2012. doi: 10.1103/RevModPhys.84.1527. URL `http://link.aps.org/doi/10.1103/RevModPhys.84.1527`.

[60] Wenhui Li, I. Mourachko, M. W. Noel, and T. F. Gallagher. Millimeter-wave spectroscopy of cold rb rydberg atoms in a magneto-optical trap: Quantum defects of the *ns* , *np* , and *nd* series. *Phys. Rev. A*, 67:052502, May 2003. doi: 10.1103/PhysRevA.67.052502. URL `http://link.aps.org/doi/10.1103/PhysRevA.67.052502`.

[61] Markus Mack, Florian Karlewski, Helge Hattermann, Simone Höckh, Florian Jessen, Daniel Cano, and József Fortágh. Measurement of absolute transition frequencies of ^{87}Rb to nS and nD rydberg states by means of electromagnetically induced transparency. *Phys. Rev. A*, 83:052515, May 2011. doi: 10.1103/PhysRevA.83.052515. URL `http://link.aps.org/doi/10.1103/PhysRevA.83.052515`.

[62] Ulf Litzén. The 5 g levels of the alkali metals. *Physica Scripta*, 1(5-6):253, 1970. URL `http://iopscience.iop.org/1402-4896/1/5-6/012`.

[63] Jianing Han, Yasir Jamil, D. V. L. Norum, Paul J. Tanner, and T. F. Gallagher. Rb nf quantum defects from millimeter-wave spectroscopy of cold ^{85}Rb rydberg atoms. *Phys. Rev. A*, 74:054502, Nov 2006. doi: 10.1103/PhysRevA.74.054502. URL `http://link.aps.org/doi/10.1103/PhysRevA.74.054502`.

[64] K. Afrousheh, P. Bohlouli-Zanjani, J. A. Petrus, and J. D. D. Martin. Determination of the ^{85}Rb ng-series quantum defect by electric-field-induced resonant energy transfer between cold rydberg atoms. *Phys. Rev. A*, 74:062712, Dec 2006. doi: 10.1103/PhysRevA.74.062712. URL `http://link.aps.org/doi/10.110`.

[65] J. R. Guest, J.-H. Choi, and G. Raithel. Decay rates of high-$|m|$ rydberg states in strong magnetic fields. *Phys. Rev. A*, 68:022509, Aug 2003. doi: 10.1103/PhysRevA.68.022509. URL `http://link.aps.org/doi/10.1103/PhysRevA.68.022509`.

[66] P Pillet, T Vogt, M Viteau, A Chotia, J Zhao, D Comparat, T F Gallagher, D Tate, A Gatan, Y Miroshnychenko, T Wilk, A Browaeys, and P Grangier. Controllable interactions between rydberg atoms and ultracold plasmas. *Journal of Physics: Conference*

Series, 194(1):012066, 2009. URL http://stacks.iop.org/1742-6596/194/i=1/a=012066.

[67] D. Tong, S. M. Farooqi, J. Stanojevic, S. Krishnan, Y. P. Zhang, R. Côté, E. E. Eyler, and P. L. Gould. Local blockade of rydberg excitation in an ultracold gas. *Phys. Rev. Lett.*, 93:063001, 2004. doi: 10.1103/PhysRevLett.93.063001.

[68] A. Schwarzkopf, R. E. Sapiro, and G. Raithel. Imaging spatial correlations of rydberg excitations in cold atom clouds. *Phys. Rev. Lett.*, 107:103001, Aug 2011. doi: 10.1103/PhysRevLett.107.103001. URL http://link.aps.org/doi/10.1103/PhysRevLett.107.103001.

[69] A. Schwarzkopf, D. A. Anderson, N. Thaicharoen, and G. Raithel. Spatial correlations between rydberg atoms in an optical dipole trap. *Phys. Rev. A*, 88:061406, Dec 2013. doi: 10.1103/PhysRevA.88.061406. URL http://link.aps.org/doi/10.1103/PhysRevA.88.061406.

[70] A. Reinhard, T. Cubel Liebisch, B. Knuffman, and G. Raithel. Level shifts of rubidium rydberg states due to binary interactions. *Phys. Rev. A*, 75:032712, Mar 2007. doi: 10.1103/PhysRevA.75.032712. URL http://link.aps.org/doi/10.1103/PhysRevA.75.032712.

[71] L. Béguin, A. Vernier, R. Chicireanu, T. Lahaye, and A. Browaeys. Direct measurement of the van der waals interaction between two rydberg atoms. *Phys. Rev. Lett.*, 110:263201, Jun 2013. doi: 10.1103/PhysRevLett.110.263201. URL http://link.aps.org/doi/10.1103/PhysRevLett.110.263201.

[72] M. D. Lukin, M. Fleischhauer, R. Cote, L. M. Duan, D. Jaksch, J. I. Cirac, and P. Zoller. Dipole blockade and quantum information processing in mesoscopic atomic ensembles. *Phys. Rev. Lett.*, 87:037901, Jun 2001. doi: 10.1103/PhysRevLett.87.037901. URL http://link.aps.org/doi/10.1103/PhysRevLett.87.037901.

[73] M. Saffman, T. G. Walker, and K. Mølmer. Quantum information with rydberg atoms. *Rev. Mod. Phys.*, 82:2313–2363, Aug 2010. doi: 10.1103/RevModPhys.82.2313. URL http://link.aps.org/doi/10.1103/RevModPhys.82.2313.

[74] Alexey V. Gorshkov, Johannes Otterbach, Michael Fleischhauer, Thomas Pohl, and Mikhail D. Lukin. Photon-photon interactions via rydberg blockade. *Phys. Rev. Lett.*, 107:133602, Sep 2011. doi: 10.1103/PhysRevLett.107.133602. URL http://link.aps.org/doi/10.1103/PhysRevLett.107.133602.

[75] J. J. Sakurai. *Modern Quantum Mechanics Revised Edition*. 1994.

[76] Robert W. Molof, Henry L. Schwartz, Thomas M. Miller, and Benjamin Bederson. Measurements of electric dipole polarizabilities of the alkali-metal atoms and the metastable noble-gas atoms. *Phys. Rev. A*, 10:1131–1140, Oct 1974. doi: 10.1103/PhysRevA.10.1131. URL http://link.aps.org/doi/10.1103/PhysRevA.10.1131.

[77] George J. Schulz. Resonances in electron impact on atoms. *Rev. Mod. Phys.*, 45:378–422, Jul 1973. doi: 10.1103/RevModPhys.45.378. URL http://link.aps.org/doi/10.1103/RevModPhys.45.378.

[78] Thomas F. O'Malley, Leonard Rosenberg, and Larry Spruch. Low-energy scattering of a charged particle by a neutral polarizable system. *Phys. Rev.*, 125:1300–1310, Feb 1962. doi: 10.1103/PhysRev.125.1300. URL http://link.aps.org/doi/10.1103/PhysRev.125.1300.

[79] John M. Brown and Alan Carrington. *Rotational spectroscopy of diatomic molecules*. 2003.

[80] F. Hund. *Handbuch der Physik*, volume 24. 1933.

[81] Rui Zhang. *Cold Neutral Atoms in Optical Lattices*. PhD thesis, University of Michigan, 2008.

[82] E. L. Raab, M. Prentiss, Alex Cable, Steven Chu, and D. E. Pritchard. Trapping of neutral sodium atoms with radiation pressure. *Phys. Rev. Lett.*, 59:2631–2634, Dec 1987. doi: 10.1103/PhysRevLett.59.2631. URL http://link.aps.org/doi/10.1103/PhysRevLett.59.2631.

[83] Rob Williamson, P. Voytas, R. Newell, and Thad Walker. A magneto-optical trap loaded from a pyramidal funnel. *Opt. Express*, 3(3):111–117, Aug 1998. doi: 10.1364/OE.3.000111. URL http://www.opticsexpress.org/abstract.cfm?URI=oe-3-3-111.

[84] H. J. Metcalf and P. van der Straten. *Laser Cooling and Trapping*. 1999.

[85] Z. T. Lu, K. L. Corwin, M. J. Renn, M. H. Anderson, E. A. Cornell, and C. E. Wieman. Low-velocity intense source of atoms from a magneto-optical trap. *Phys. Rev. Lett.*, 77:3331–3334, Oct 1996. doi: 10.1103/PhysRevLett.77.3331. URL http://link.aps.org/doi/10.1103/PhysRevLett.77.3331.

[86] J. Reichel, W. Hänsel, and T. W. Hänsch. Atomic micromanipulation with magnetic surface traps. *Phys. Rev. Lett.*, 83:3398–3401, Oct 1999. doi: 10.1103/PhysRevLett.83.3398. URL http://link.aps.org/doi/10.1103/PhysRevLett.83.3398.

[87] József Fortágh and Claus Zimmermann. Magnetic microtraps for ultracold atoms. *Rev. Mod. Phys.*, 79:235–289, Feb 2007. doi: 10.1103/RevModPhys.79.235. URL http://link.aps.org/doi/10.1103/RevModPhys.79.235.

[88] H. R. Sadeghpour and S. T. Rittenhouse. How do ultralong-range homonuclear rydberg molecules get their permanent dipole moments? *Molecular Physics*, 111(12-13):1902–1907, 2013. doi: 10.1080/00268976.2013.811555. URL http://www.tandfonline.com/doi/abs/10.1080/00268976.2013.811555.

[89] G.C. Wick. *Rend. Lincci*, 19, 27, 1934.

[90] D. Meschede. Centimeter-wave spectroscopy of highly excited rubidium atoms. *J. Opt. Soc. Am. B*, 4:413 – 19, 1987.

[91] Atreju Tauschinsky, Richard Newell, H. B. van Linden van den Heuvell, and R. J. C. Spreeuw. Measurement of ^{87}rb rydberg-state hyperfine splitting in a room-temperature vapor cell. *Phys. Rev. A*, 87:042522, Apr 2013. doi: 10.1103/PhysRevA.87.042522. URL http://link.aps.org/doi/10.1103/PhysRevA.87.042522.

[92] H. Sassmannshausen, F. Merkt, and J. Deiglmayr. High-resolution spectroscopy of rydberg states in an ultracold cesium gas. *Phys. Rev. A*, 87:032519 (10 pp.) –, 2013.

[93] Eugene P. Wigner. Lower limit for the energy derivative of the scattering phase shift. *Phys. Rev.*, 98:145–147, Apr 1955. doi: 10.1103/PhysRev.98.145. URL http://link.aps.org/doi/10.1103/PhysRev.98.145.

[94] Bjrn Butscher, Vera Bendkowsky, Johannes Nipper, Jonathan B Balewski, Ludmila Kukota, Robert Lw, Tilman Pfau, Weibin Li, Thomas Pohl, and Jan Michael Rost. Lifetimes of ultralong-range rydberg molecules in vibrational ground and excited states. *Journal of Physics B: Atomic, Molecular and Optical Physics*, 44(18):184004, 2011. URL http://stacks.iop.org/0953-4075/44/i=18/a=184004.

[95] Andrej Junginger, Jrg Main, and Gnter Wunner. Quantum-classical lifetimes of rydberg molecules. *Journal of Physics B: Atomic, Molecular and Optical Physics*, 46(8): 085201, 2013. URL http://stacks.iop.org/0953-4075/46/i=8/a=085201.

[96] Donald Booth, Seth Rittenhouse, Jin Yang, Hossein Sadeghpour, and James Shaffer. Production of trilobite rydberg molecule dimers with thousand-debye permanent electric dipole moments. *arXiv:1411.5291*, September 2014. URL http://arxiv.org/abs/1411.5291.

[97] P. Goy, J. M. Raimond, G. Vitrant, and S. Haroche. Millimeter-wave spectroscopy in cesium rydberg states. quantum defects, fine- and hyperfine-structure measurements. *Phys. Rev. A*, 26:2733–2742, Nov 1982. doi: 10.1103/PhysRevA.26.2733. URL http://link.aps.org/doi/10.1103/PhysRevA.26.2733.

[98] Zhang Lin-Jie, Feng Zhi-Gang, Li An-Ling, Zhao Jian-Ming, Li Chang-Yong, and Jia Suo-Tang. Measurement of quantum defects of n s and n d states using field ionization spectroscopy in ultracold cesium atoms. *Chinese Physics B*, 18(5):1838, 2009. URL http://stacks.iop.org/1674-1056/18/i=5/a=020.

[99] S. K. Dutta, J. R. Guest, D. Feldbaum, A. Walz-Flannigan, and G. Raithel. Ponderomotive optical lattice for rydberg atoms. *Phys. Rev. Lett.*, 85:5551–5554, Dec 2000. doi: 10.1103/PhysRevLett.85.5551. URL http://link.aps.org/doi/10.1103/PhysRevLett.85.5551.

[100] William H. Wing. Electrostatic trapping of neutral atomic particles. *Phys. Rev. Lett.*, 45:631–634, Aug 1980. doi: 10.1103/PhysRevLett.45.631. URL http://link.aps.org/doi/10.1103/PhysRevLett.45.631.

[101] Bernd Hezel, Igor Lesanovsky, and Peter Schmelcher. Controlling ultracold rydberg atoms in the quantum regime. *Phys. Rev. Lett.*, 97:223001, Nov 2006. doi: 10.1103/PhysRevLett.97.223001. URL http://link.aps.org/doi/10.1103/PhysRevLett.97.223001.

[102] S. E. Anderson, K. C. Younge, and G. Raithel. Trapping rydberg atoms in an optical lattice. *Phys. Rev. Lett.*, 107:263001, Dec 2011. doi: 10.1103/PhysRevLett.107.263001. URL http://link.aps.org/doi/10.1103/PhysRevLett.107.263001.

[103] S. Zhang, F. Robicheaux, and M. Saffman. Magic-wavelength optical traps for rydberg atoms. *Phys. Rev. A*, 84:043408, Oct 2011. doi: 10.1103/PhysRevA.84.043408. URL http://link.aps.org/doi/10.1103/PhysRevA.84.043408.

[104] S. D. Hogan and F. Merkt. Demonstration of three-dimensional electrostatic trapping of state-selected rydberg atoms. *Phys. Rev. Lett.*, 100:043001, Jan 2008. doi: 10.1103/PhysRevLett.100.043001. URL http://link.aps.org/doi/10.1103/PhysRevLett.100.043001.

[105] J.-H. Choi, J. R. Guest, A. P. Povilus, E. Hansis, and G. Raithel. Magnetic trapping of long-lived cold rydberg atoms. *Phys. Rev. Lett.*, 95:243001, Dec 2005. doi: 10.1103/PhysRevLett.95.243001. URL http://link.aps.org/doi/10.1103/PhysRevLett.95.243001.

[106] R.J. Brecha, G. Raithel, C. Wagner, and H. Walther. Circular rydberg states with very large n. *Optics Communications*, 102(34):257 – 264, 1993. ISSN 0030-4018. doi: http://dx.doi.org/10.1016/0030-4018(93)90392-I. URL http://www.sciencedirect.com/science/article/pii/003040189390392I.

[107] A. Nussenzweig, J. Hare, A. M. Steinberg, L. Moi, M. Gross, and S. Haroche. A continuous beam of circular rydberg atoms for fundamental tests and applications in metrology. *EPL (Europhysics Letters)*, 14(8):755, 1991. URL http://stacks.iop.org/0295-5075/14/i=8/a=006.

[108] Jan R. Rubbmark, Michael M. Kash, Michael G. Littman, and Daniel Kleppner. Dynamical effects at avoided level crossings: A study of the landau-zener effect using rydberg atoms. *Phys. Rev. A*, 23:3107–3117, Jun 1981. doi: 10.1103/PhysRevA.23.3107. URL http://link.aps.org/doi/10.1103/PhysRevA.23.3107.

[109] T. P. Hezel, C. E. Burkhardt, M. Ciocca, LW. He, and J. J. Leventhal. Classical view of the properties of rydberg atoms: Application of the correspondence principle. *American Journal of Physics*, 60(4), 1992.

[110] C. O. Reinhold, J. Burgdörfer, M. T. Frey, and F. B. Dunning. Dynamical stabilization of the periodically kicked rydberg atom. *Phys. Rev. Lett.*, 79:5226–5229, Dec 1997. doi: 10.1103/PhysRevLett.79.5226. URL http://link.aps.org/doi/10.1103/PhysRevLett.79.5226.

[111] F Robicheaux. Ionization due to the interaction between two rydberg atoms. *Journal of Physics B: Atomic, Molecular and Optical Physics*, 38(2):S333, 2005. URL http://stacks.iop.org/0953-4075/38/i=2/a=024.

[112] Toshio Fukushima. Numerical computation of spherical harmonics of arbitrary degree and order by extending exponent of floating point numbers. *Journal of Geodesy*, 86 (4):271–285, 2012. ISSN 0949-7714. doi: 10.1007/s00190-011-0519-2. URL http://dx.doi.org/10.1007/s00190-011-0519-2.

[113] R.F. Stebbings and F.B. Dunning. *Rydberg states of atoms and molecules*. Cambridge University Press, New York, NY, USA, 1983.

[114] Seth T. Rittenhouse and H. R. Sadeghpour. Ultracold giant polyatomic rydberg molecules: Coherent control of molecular orientation. *Phys. Rev. Lett.*, 104:243002, Jun 2010. doi: 10.1103/PhysRevLett.104.243002. URL http://link.aps.org/doi/10.1103/PhysRevLett.104.243002.

[115] P.A.M. Dirac. The quantum theory of the emission and absorption of radiation. *Proc. R. Soc. Lond. A*, 114(767):243–265, 1927. URL http://rspa.royalsocietypublishing.org/content/114/767/243.